UNIVERSITY OF OKLAHOMA

GRADUATE COLLEGE

RADIATIVELY-DRIVEN NATURAL SUPERSYMMETRY

A DISSERTATION

SUBMITTED TO THE GRADUATE FACULTY

in partial fulfillment of the requirements for the

Degree of

DOCTOR OF PHILOSOPHY

By

DANIEL S. MICKELSON
Norman, Oklahoma
2014

Downloaded from SHAREOK. Persistent Handle URL: https://hdl.handle.net/11244/10493

RADIATIVELY-DRIVEN NATURAL SUPERSYMMETRY

A DISSERTATION APPROVED FOR THE
HOMER L. DODGE DEPARTMENT OF PHYSICS AND ASTRONOMY

BY

Dr. Howard Baer, Chair

Dr. Braden Abbott

Dr. Bruce Mason

Dr. Kimball Milton

Dr. Nikola Petrov

©Copyright by DANIEL S. MICKELSON 2014
All Rights Reserved.

To Kristina, without whom this would not have been possible.

Table of Contents

List of Figures **vi**

List of Tables **x**

Abstract **xi**

1 Introduction **1**
1.1 The Standard Model . . . 2
1.1.1 The Electroweak Theory and Quantum Chromodynamics . . . 2
1.1.2 The SM Higgs Mechanism . . . 4
1.1.3 Motivations for Physics Beyond the Standard Model . . . 5
1.2 Supersymmetry . . . 6
1.2.1 Supermultiplets and the SUSY Lagrangian . . . 7
1.2.2 SUSY Breaking . . . 10
1.2.3 The Minimal Supersymmetric Standard Model . . . 12
1.2.4 Extensions and Alternatives to mSUGRA . . . 15

2 Naturalness in SUSY [33, 34] **17**
2.1 Standard Model Fine-Tuning . . . 17
2.2 Electroweak Fine-Tuning $\Delta_{\rm EW}$ . . . 18
2.3 Fine-Tuning of the Higgs mass . . . 21
2.4 Barbieri-Giudice Fine-Tuning $\Delta_{\rm BG}$ . . . 22

3 Radiative Natural Supersymmetry [40, 47] **26**
3.1 Radiative natural SUSY from the NUHM models . . . 33
3.1.1 RNS from the NUHM2 model . . . 33
3.1.2 RNS from the NUHM1 model . . . 42
3.1.3 RNS from the NUHM3 (split generation) model . . . 44
3.2 Rare B decay constraints on RNS . . . 47
3.3 BF($b \to s\gamma$) . . . 47
3.4 $B_s \to \mu^+\mu^-$ . . . 47
3.5 $(g-2)_\mu$ . . . 49

4 Radiative Natural Supersymmetry at the LHC [37, 69] **50**
4.1 Simulation of Collider Events . . . 50
4.2 A radiative natural SUSY model line . . . 52
4.3 Sparticle production at LHC . . . 55
4.4 Sparticle branching fractions . . . 58
4.5 Gluino cascade decay signatures . . . 61
4.5.1 OS/SF dilepton mass distribution from cascade decays . . . 65
4.6 Same-sign diboson signature . . . 66
4.7 Hard trileptons from wino pair production . . . 71
4.8 Four leptons from heavy gaugino production . . . 74
4.9 Soft trileptons from direct higgsino pair production . . . 79

5 Physics at a higgsino factory [96] 83
5.1 Simulation of Events at an e^+e^- collider 84
5.2 Two RNS benchmark points 85
5.3 Sparticle production and decay 86
5.3.1 Sparticle production 86
5.3.2 Higgsino decays 92
5.4 SUSY event generation 92
5.5 Benchmark ILC1 at $\sqrt{s} = 250$ GeV 94
5.5.1 Chargino pair production for ILC1 99
5.5.2 Neutralino pair production for ILC1 103
5.6 Benchmark ILC2 at $\sqrt{s} = 340$ GeV 108
5.6.1 Chargino pair production for ILC2 108
5.6.2 Neutralino pair production for ILC2 111

6 Radiative Natural Supersymmetry and Dark Matter [39] 118
6.1 Direct Detection of higgsino-like WIMPs 123
6.2 Indirect Detection of higgsino-like WIMPs 127

7 Summary 131

8 References 135

List of Figures

1 Typical mass spectrum from low $\Delta_{\rm EW}$ models. 19
2 Plot of contributions to $m_Z^2/2$ from the mSUGRA/CMSSM model with parameters as listed, and also for the RNS2 benchmark point with the same $m_0, m_{1/2}, A_0$, and $\tan\beta$ values but with $\mu = 150$ GeV. Red bars denote negative contributions, while blue bars denote positive contributions. 27
3 Evolution of SSB parameters from $M_{\rm GUT}$ to M_{weak} for the RNS2 benchmark point taken from in Ref. [47] whose parameters are given in the text. 29
4 Signed contributions to $m_Z^2/2$ from terms in the EWSB minimization condition Eq. 2.4. 32
5 The dependence of $\Delta_{\rm EW}$ on various NUHM2 parameters from a scan (3.3) over parameter space. 36
6 The value of $\Delta_{\rm EW}$ versus gluino and third generation squark masses from a scan over NUHM2 parameter space. 38
7 The value of $\Delta_{\rm EW}$ versus electroweak -ino and Higgs boson masses from a scan over NUHM2 parameter space. 40
8 The value of $\Delta_{\rm EW}$ versus $m_{H_u}/m_0(M_{\rm GUT})$ from the scan over the NUHM2 parameter space. 41
9 Plot of $\Delta_{\rm EW}$ vs. m_0 from a scan over NUHM1 parameter space while maintaining $m_h = 125.5 \pm 2.5$ GeV. 43
10 The value of $\Delta_{\rm EW}$ versus $m_0(3)$ and $m_0(1,2)$ from a scan over NUHM3 model with split first/second and third generations. 46
11 The values of $\Delta_{\rm EW}$ versus *a*) $BF(b \to s\gamma)$ and *b*) $BF(B_s \to \mu^+\mu^-)$. . 48
12 Plot of $\Delta_{\rm EW}$ versus $m_{1/2}$ along the RNS model line. 53
13 Various sparticle masses versus $m_{1/2}$ for the RNS model line. 54
14 The $m_{\widetilde{Z}_2} - m_{\widetilde{Z}_1}$ mass gap versus $m_{1/2}$ along the RNS model line. . . 55
15 Plot of various NLO sparticle pair production cross sections versus $m_{1/2}$ along the RNS model line for pp collisions at *a*) $\sqrt{s} = 8$ TeV and *b*) $\sqrt{s} = 14$ TeV. 56
16 Plot of various NLO electroweak-ino pair production cross sections versus μ for the RNS model line with $m_{1/2} = 750$ GeV for pp collisions at 14 TeV. 58
17 Plot of various sparticle branching fractions versus $m_{1/2}$ along the RNS model line. 59
18 Plot of gluino cross section in fb after cuts *C2* for $1\ell + jets$ and $0\ell + jets$ channel and cuts *C3* for OS, SS and $3\ell + jets$ channels from gluino cascade decays along the RNS model line at LHC14. . . . 64
19 Distribution of the invariant mass of opposite-sign/same-flavor dileptons after cuts *C3* at LHC14 from the RNS benchmark model line with $m_{1/2} = 450$ GeV. 65
20 Transverse mass and missing energy distributions for SSdB events after cuts at LHC14. 69

21 Same-sign dilepton cross sections (in *fb*) at LHC14 after cuts vs. $m_{1/2}$ along the RNS model line from $\widetilde{W}_2^{\pm}\widetilde{Z}_4$ and $\widetilde{W}_2^{\pm}\widetilde{W}_2^{\mp}$ production and calculated reach for 100, 300 and 1000 fb^{-1}. 70
22 Transverse mass and missing energy distributions for hard trilepton events after the preliminary cuts at LHC14. 73
23 Tri-lepton cross sections (in *fb*) at LHC14 after cuts vs. $m_{1/2}$ along the RNS model line from wino pair production processes $pp \to \widetilde{W}_2\widetilde{Z}_4/\widetilde{W}_2\widetilde{W}_2 \to WZ + E_T^{\rm miss} \to 3\ell + E_T^{\rm miss}$ events. 75
24 The $E_T^{\rm miss}$ distributions for 4ℓ events with $n_b = 0$ from various SM sources and for two signal points on the RNS model-line. 77
25 $p_T(e)$ distribution for soft tri-leptons from higgsino pairs before cuts for two RNS points with $m_{1/2} = 400$ GeV (red) and 1000 GeV (blue) at LHC14. 80
26 The dimuon invariant mass distributions after cuts for $e\mu\mu$ events. . . 82
27 Contours of the mass gap (green curves) $m_{\widetilde{Z}_2} - m_{\widetilde{Z}_1}$ in the $m_{1/2} - \mu$ mass plane of the NUHM2 model for $m_0 = 5$ TeV, $A_0 = -1.6m_0$, $\tan\beta = 15$ and $m_A = 1$ TeV. The red curves show contours of Δ_{EW}. . 87
28 Sparticle production cross sections vs. $\sqrt{s}$ for unpolarized beams at an e^+e^- collider for the ILC1 benchmark point listed in Table 8. . . . 89
29 Sparticle production cross sections vs. $P_L(e^-)$ at an e^+e^- collider for the ILC1 benchmark point with $\sqrt{s} = 250$ GeV. The positrons are taken to be unpolarized. For comparison, shown is a point with a wino-like chargino of similar mass. For the wino-like case with $m_{1/2} = 120$ GeV, then the $\sigma(e^+e^- \to \widetilde{Z}_1\widetilde{Z}_2) \sim 0.1$ fb, while $\sigma(\widetilde{Z}_2\widetilde{Z}_2)$ is even smaller, and so is far below the cross section values shown. . 91
30 Distribution in visible energy measured in e^+e^- events at $\sqrt{s} = 250$ GeV for ILC1 signal and SM backgrounds from e^+e^- and $\gamma\gamma$ collisions. 95
31 Distribution of missing transverse energy from e^+e^- collisions at $\sqrt{s} = 250$ GeV for ILC1 signal along with SM background from e^+e^- and $\gamma\gamma$ collisions. 96
32 Distribution of *a*) isolated lepton multiplicity and *b*) jet multiplicity from e^+e^- collisions at $\sqrt{s} = 250$ GeV for higgsino signals from the ILC1 case study along with corresponding SM backgrounds from e^+e^- and $\gamma\gamma$ collisions. 98
33 Scatter plot in the $E(jj)$ vs. $m(jj)$ plane for $1\ell + 2 - jets$ events from the ILC1 point in e^+e^- collisions at $\sqrt{s} = 250$ GeV. 100
34 Shown in *a*) are values of $\Delta\chi^2$ found from matching 100 fb^{-1} of ILC1 "data" to various "theory" distributions generated from a scan over μ *vs.* $m_{1/2}$ space. In *b*), is the distribution in $E(jj)$ from 100 fb^{-1} of "data" along with best fit distribution. 102

35 Distribution in $E(\ell^+\ell^-)$ from 100 fb^{-1} of "data" of OS/SF dilepton events with $P_L(e^-) = -0.9$ from the signal for the ILC1 case, and from SM background (which only comes from $2 \to 2$ processes), after the E_{vis} and $\Delta\phi(\ell\ell)$ cuts discussed in the text. 104
36 Shown in *a*) are values of χ^2 vs. $m(\ell^+\ell^-)$ from 100 fb^{-1} of OS/SF dilepton ILC1 "data" from $\widetilde{Z}_1\widetilde{Z}_2$ production fit to the shapes from various "theory" templates, as described in the text. In *b*), are the ILC1 "data" for the $m(\ell^+\ell^-)$ distribution from $\widetilde{Z}_1\widetilde{Z}_2$ events along with statistical error for 100 fb^{-1}. The solid curve shows the best fit to these "data". 106
37 Shown in *a*), are fitted values of χ^2 found from matching 100 fb^{-1} of OS/SF dilepton "data" from $\widetilde{Z}_1\widetilde{Z}_2$ production to various "theory" distributions generated from varying $m_{\widetilde{Z}_2}$ while keeping $m_{\widetilde{Z}_2} - m_{\widetilde{Z}_1}$ fixed at 21 GeV. In *b*) is the distribution in $E(\ell^+\ell^-)$ from a 100 fb^{-1} of OS/SF dilepton ILC1 "data" from $\widetilde{Z}_1\widetilde{Z}_2$ production along with best fit. 107
38 Distribution in E_{vis} from benchmark ILC2 signal and SM backgrounds at ILC with $\sqrt{s} = 340$ GeV and $\Upsilon = 0.03$. 109
39 Distribution in missing transverse energy from e^+e^- collisions at $\sqrt{s} = 340$ GeV for signal from the ILC2 benchmark case, along with SM backgrounds from e^+e^- and $\gamma\gamma$ collisions. 110
40 Distribution in transverse plane opening angle between the isolated lepton and jet for the ILC2 signal point at $\sqrt{s} = 340$ GeV, and for SM backgrounds. 112
41 Distribution in transverse opening angle between isolated OS/SF leptons for ILC2 signal at $\sqrt{s} = 340$ GeV and for SM backgrounds. . . . 114
42 Shown in *a* are χ^2 values vs. $m(\ell^+\ell^-)$ from 100 fb^{-1} of OS/SF dilepton ILC2 "data" from $\widetilde{Z}_1\widetilde{Z}_2$ production fit to theory along with a best-fit parabola. In *b*) is the distribution in $m(\ell^+\ell^-)$ from a 100 fb^{-1} of OS/SF dilepton ILC2 "data" from $\widetilde{Z}_1\widetilde{Z}_2$ production along with best fit. 115
43 Shown in *a*) are values of χ^2 found from matching 100 fb^{-1} of OS/SF dilepton ILC2 "data" from $\widetilde{Z}_1\widetilde{Z}_2$ production to various "theory" distributions generated from varying $m_{\widetilde{Z}_2}$ while keeping $m_{\widetilde{Z}_2} - m_{\widetilde{Z}_1}$ fixed at 9.7 GeV. In *b*) is the distribution in $E(\ell^+\ell^-)$ from a 100 fb^{-1} of OS/SF dilepton ILC2 "data" from $\widetilde{Z}_1\widetilde{Z}_2$ production along with best fit. 117
44 Plot of standard thermal neutralino abundance $\Omega^{std}_{\widetilde{Z}_1}h^2$ versus higgsino mass. 121
45 Two of the Feynman diagrams that contribute to the nucleus-neutralino interactions. On the left is Higgs exchange, the light Higgs exchange will dominate, since the heavy Higgs will not contribute in the decoupling limit. On the right is squark exchange. 123

46 Plot of rescaled WIMP spin-independent detection rate $\xi\sigma^{SI}(\widetilde{Z}_1 p)$ versus m(higgsino). 124
47 Plot of rescaled spin-dependent higgsino-like WIMP detection rate $\xi\sigma^{SD}(\widetilde{Z}_1 p)$ versus m(higgsino) from a scan over NUHM2 parameter space. 126
48 Plot of (non-rescaled) spin-dependent higgsino-like WIMP detection rate $\sigma^{SD}(\widetilde{Z}_1 p)$ versus m(higgsino) from a scan over NUHM2 parameter space. 128
49 Plot of $\xi^2 \langle \sigma v \rangle_{v \to 0}$ versus m(higgsino). 130

List of Tables

1 The matter and Higgs chiral supermultiplet content in the MSSM for one generation. 14
2 The gauge supermultiplets in the MSSM. 14
3 Dominant branching fractions of various sparticles along the RNS model line for $m_{1/2} = 1$ TeV. 61
4 Number of events generated and cross section after cuts for the dominant backgrounds in the hard trilepton channel and for the RNS signal with $m_{1/2} = 350$ GeV. 74
5 Background and signal rates in fb for 4-lepton events at LHC14 after cuts. 77
6 Background and signal rates in fb for soft $3\ell + E_T^{\rm miss}$ events at LHC14 after cuts. 80
7 Reach of LHC14 for SUSY in terms of gluino mass, $m_{\tilde{g}}$ (TeV), assuming various integrated luminosity values along the RNS model line. 81
8 NUHM2 input parameters and masses in GeV units for the two RNS benchmark points introduced in the text. Here $m_t = 173.2$ GeV. . . . 88

Abstract

Within the framework of supersymmetric theories, a question arises: how can the W, Z, and h masses be so low (~ 100 GeV) when the superpartner masses are so high ($m_{SUSY} > 1-2$ TeV)? This is the little hierarchy problem, and can be quantified by studying the *fine-tuning* of a particular model. Quantifying a model in such a way provides a unique opportunity to give upper bounds on the supersymmetric particle masses. Introduced in this dissertation is the model called *Radiatively-driven Natural Supersymmetry*, wherein low fine-tuning is achieved while maintaining a light Higgs scalar $\simeq 125$ GeV. In addition, RNS offers a particle spectrum that evades searches at all current collider experiments, and satisfies cosmological constraints. It is shown that RNS could be discovered with high luminosity at LHC14 in multiple channels, having a soft trilepton + MET signature, a unique same-sign diboson signature accompanied by jets, and gluino cascade decays in the trilepton+jets channel. An International Linear Collider operating at $\sqrt{s} = 600$ GeV would either discover RNS or rule it out as a feasible model. Dark matter direct and indirect detection experiments also offer a means of discovery, with a 1-ton noble gas detector effectively probing the entirety of RNS parameter space.

1 Introduction

The Standard Model (SM) has demonstrated huge success in the current understanding of particle physics and, as predicted, the LHC has discovered the long sought after Higgs boson. Despite the success of the Higgs discovery with $m_h \simeq 125$ GeV, the Higgs mass in the SM suffers from quadratic divergences. These quadratic divergences are removed when one considers supersymmetry (SUSY). However, the introduction of SUSY also introduces supersymmetric partner particles. No sign of supersymmetry has yet emerged at the LHC, leading to mass limits $m_{\tilde{g}} \gtrsim 1.8$ TeV (for $m_{\tilde{g}} \simeq m_{\tilde{q}}$) and $m_{\tilde{g}} \gtrsim 1.3$ TeV (for $m_{\tilde{g}} \ll m_{\tilde{q}}$) [1,2]. These limits are obtained in the context of popular models such as mSUGRA/CMSSM [3,4], but are qualitatively also valid in other frameworks as long as one understands that the squark mass limit refers to first generation squarks. These squark and gluino mass limits have caused concern for some physicists, arguing that in order to maintain naturalness in SUSY models, sparticles ought to be well below the TeV scale [5,6,7,8,9,10,11,12,13,14]. This leads to the little hierarchy problem (LHP): How do SUSY parameters at or above the TeV scale lead to W, Z, and h masses of just ~ 100 GeV? Models of *natural supersymmetry* (NS) [15] address the LHP by positing a spectrum of light higgsinos $\lesssim 200$ GeV and light top- and bottom-squarks with $m_{\tilde{t}_{1,2},\tilde{b}_1} \lesssim 600$ GeV along with very heavy first/second generation squarks and TeV-scale gluinos [16,17,18,19]. The absence of any hint of deviations from the SM in the LHC8 data have led some to question whether SUSY could be the solution to the naturalness problem of the SM.

This dissertation describes a model within the framework of the MSSM that satisfies all of the constraints experimental data requires, while allowing for desirable theoretical considerations. The model, Radiatively-driven Natural Supersymmetry (RNS), has low electroweak fine-tuning, a cold dark matter (CDM) candidate, and satisfies the experimental constraints set by the LHC and LEP2.

This chapter introduces the Standard Model, outlines the notation, and sets the framework for the remaining chapters. This will also be useful information concerning the later discussions of physics at hadron and linear colliders. The deficiancies of the SM are pointed out, along with what one may expect from a theory beyond the SM (BSM). Supersymmetry (SUSY) and SUSY theories in general are then introduced, before moving onto the simplest example, the Minimal Supersymmetric Standard Model (MSSM). In Chapter 2, 'Naturalness' is defined along with various fine-tuning measures and how these affect the search for acceptable SUSY theories. Chapter 3 introduces the framework of RNS and points out the advantages of RNS over other theories. Chapters 4 and 5 investigate prospects for discovery at the LHC and a future linear collider, respectively. In Chapter 6, the lightest neutralino as a WIMP along with prospects for both direct and indirect detection of dark matter is discussed.

1.1 The Standard Model

1.1.1 The Electroweak Theory and Quantum Chromodynamics

The Standard Model is the most successful theory of elementary particle physics constructed and was finalized in the 1970's. It describes the electromagnetic, weak and strong interactions successfully across a large range of energies. The SM is a quantum field theory built up of two parts: the $SU(3)_C$ color theory of strong interactions, Quantum Chromodynamics (QCD), and the $SU(2)_L \times U(1)_Y$ electroweak theory (EW). The complete theory, based on $SU(3)_C \times SU(2)_L \times U(1)_Y$, combines them.

The electroweak (EW) theory describes the electromagnetic and weak interactions in the SM. The EW symmetry is spontaneously broken from $SU(2)_L \times U(1)_Y \rightarrow U(1)_{QED}$ via the Higgs mechanism, giving rise to massive W and Z bosons, quarks,

leptons, and a physical Higgs scalar. The EW Lagrangian is given by

$$\mathcal{L}_{EW} = \mathcal{L}_{gauge} + \mathcal{L}_{matter} + \mathcal{L}_{Higgs} + \mathcal{L}_{Yukawa} \tag{1.1}$$

where

$$\mathcal{L}_{gauge} = -\frac{1}{4} W_{A\mu\nu} W_A^{\mu\nu} - B_{\mu\nu} B^{\mu\nu}, \tag{1.2}$$

Here, W_A and B represent the $SU(2)$ and $U(1)$ gauge fields, respectively.

$$\mathcal{L}_{matter} = i\bar{\psi} \not{D} \psi \tag{1.3}$$

D is the electroweak gauge covariant derivative,

$$D_\mu = \partial_\mu + igW_\mu \cdot T + \frac{1}{2} ig' B_\mu Y \tag{1.4}$$

where g and g' are the $SU(2)$ and $U(1)$ coupling constants, W is a gauge isotriplet for $SU(2)$, B is a gauge singlet for $U(1)$, T is the weak isospin operator, and Y is the weak hypercharge operator.

$$\mathcal{L}_{Higgs} = (D\phi)^\dagger (D\phi) + \mu^2 \phi^\dagger \phi - \lambda (\phi^\dagger \phi)^2, \tag{1.5}$$

where μ is the Standard Model Higgs mass parameter (not to be confused with the supersymmetric bilinear Higgs/higgsino mass term which will have the same notation introduced in Sec. 1.2.3). After the symmetry is broken, the Yukawa coupling of the Higgs field to the fermions is given by

$$\mathcal{L}_{Yukawa} = -\sum_i \frac{\lambda_{f_i}}{\sqrt{2}} \bar{f}_i f_i h \tag{1.6}$$

where the sum is over all of the quarks and leptons in the theory.

The QCD Lagrangian is given by

$$\mathcal{L}_{QCD} = -\frac{1}{4} G_{A\mu\nu} G_A^{\mu\nu} + \bar{q}_i (i \not{D} - m_i) q_i \tag{1.7}$$

where i is the quark index and is summed over, the G's are the $SU(3)$ gauge fields of QCD:

$$G_{A\mu\nu} = \partial_\mu G_{A\nu} - \partial_\nu G_{A\mu} - g_S f_{ABC} G_{B\mu} G_{C\nu}, \tag{1.8}$$

and D is the gauge covariant derivative:

$$D_\mu = \partial_\mu + i g_S \frac{\lambda_A}{2} G_{A\mu}. \tag{1.9}$$

Here, g_S is the strong coupling constant, and λ_A are the eight Gell-Mann matrices, a representation of the generators of the theory. The color indices on the quarks take on the values $i = 1, 2, 3$, usually called red, blue, and green. The corresponding anti-colors are anti-red, anti-blue, and anti-green. For the gluons, $A, B, C = 1, ..., 8$, where the eight colors are combinations of red, blue, green, and their anti-colors. All QCD interactions must conserve color charge, in the same way electric charge must be conserved.

1.1.2 The SM Higgs Mechanism

The Higgs mechanism [20, 21] is the process which breaks the $SU(2)_L \times U(1)_Y$ electroweak symmetry and gives mass to particles in the standard model. This process also introduces a CP-even scalar particle into the theory, called the Higgs scalar. The Higgs sector of the SM consists of an $SU(2)_L$ doublet of spin zero fields,

$$\Phi = \begin{pmatrix} \phi^+ \\ \phi^0 \end{pmatrix}. \tag{1.10}$$

The corresponding Higgs Lagrangian is given by

$$\mathcal{L}_{Higgs} = (D\phi)^\dagger (D\phi) - V(|\phi|^2) \tag{1.11}$$

where the Higgs potential is

$$V(|\phi|^2) = -\mu^2 \phi^\dagger \phi + \lambda(\phi^\dagger \phi)^2 \tag{1.12}$$

and $\phi^0 = (\phi_R^0 + i\phi_I^0)/\sqrt{2}$. Minimization of this potential leads to a non-zero vacuum expectation value (*vev*) $v = \langle \phi_R \rangle / \sqrt{2} = \sqrt{-\mu^2/2\lambda}$. The presence of a *vev* signifies the spontaneous breakdown of EW symmetry and gives mass to the vector bosons and fermions.

Within the SM, the Higgs mass is a free parameter that must be measured. In contrast, the MSSM puts an upper limit on the SM-like Higgs mass as $m_h \lesssim 130$ GeV. The recent highly successful runs at the Large Hadron Collider at CERN in Switzerland led to the discovery of a Standard Model (SM) Higgs-like resonance by the ATLAS and CMS collaborations [22, 23]. More analysis needs to be done to confirm that it is in fact the SM Higgs; however it appears that $m_h \simeq 125.5$ GeV.

1.1.3 Motivations for Physics Beyond the Standard Model

Despite the success of the SM there are several questions - both experimental and theoretical - that it does not or cannot address; thus it appears incomplete. On the experimental side, these include:

- the lack of an explanation for gravity.
- a wealth of cosmological data suggests that the universe is dominated by dark matter and dark energy.
- neutrino oscillation data imply that neutrinos have some (small) mass. This

is contradictory to the SM, where neutrinos are treated as massless (there are simple extensions to the SM which do include neutrino mass).

On the theoretical side:

- the big gauge hierarchy problem: Why is there such a discrepancy between the weak scale, and the scale which the forces become unified?
- the strong CP fine-tuning problem, which seemingly requires the Peccei-Quinn mechanism and introduction of new matter, axions, to be solved.
- gauge coupling unification is expected at a grand unified theory (GUT) energy, however this does not occur in the SM.

To address these issues, one must move beyond the SM. One might consider supersymmetry, introducing new matter, or a combination of both. As more experiments search for answers, one may even discover unexpected new physics.

1.2 Supersymmetry

Supersymmetry is a symmetry between bosons and fermions, i.e. for each boson (fermion) there exists a partner fermion (boson) that requires an extension of space-time to include anti-commuting dimensions. The representations of supersymmetry contain both the fermion and boson superpartners and are called supermultiplets. Each supermultiplet has the same number of bosonic and fermionic degrees of freedom, so that $n_F = n_B$. A simple supermultiplet is a *chiral supermultiplet* containing a Majorana spinor field (spin 1/2) and a complex scalar field (spin zero). The standard model fermions are contained in chiral supermultiplets along with their superpartners, the spin-0 sfermions. Another supermultiplet is the *gauge* or *curl supermultiplet*. The SM gauge bosons and their supersymmetric partner spin-1/2 gauginos are contained within gauge supermultiplets. In the following, all super-

symmetric formalism will follow the notation in [24], where four component spinor notation is used.

1.2.1 Supermultiplets and the SUSY Lagrangian

A left chiral supermultiplet consists of a Majorana spinor field ψ_L, a complex scalar field $\mathcal{S}$, and an *auxiliary* field $\mathcal{F}$. The simplest model using this supermultiplet with massless and non-interacting particles is the Wess-Zumino model, with the Lagrangian:

$$\mathcal{L}_{WZ} = \partial_\mu \mathcal{S}^\dagger \partial^\mu \mathcal{S} + \frac{i}{2}\bar{\psi}\partial\!\!\!/\psi + \mathcal{F}^\dagger \mathcal{F}. \tag{1.13}$$

The $\mathcal{F}$-field in the Lagrangian does not have a kinetic term, and therefore does not propogate. Instead, it satisfies an *algebraic* equation of motion. Such a term is required to be present to allow the Lagrangian to be invariant under supersymmetric transformations even when off-shell particles are present. The supersymmetric transformations for these fields are given by

$$\begin{aligned} \delta\mathcal{S} &= -i\sqrt{2}\bar{\alpha}\psi_L, \\ \delta\psi_L &= -\sqrt{2}\mathcal{F}\alpha_L + \sqrt{2}\partial\!\!\!/\mathcal{S}\alpha_R \\ \delta\mathcal{F} &= i\sqrt{2}\bar{\alpha}\partial\!\!\!/\psi_L, \end{aligned} \tag{1.14}$$

where α is a spacetime independent anti-commuting Majorana spinor parameter. The three fields ψ_L, $\mathcal{S}$, and $\mathcal{F}$ can be combined into a *superfield*

$$\hat{\mathcal{S}}(\hat{x}) = \mathcal{S}(\hat{x}) + i\sqrt{2}\bar{\theta}\psi_L(\hat{x}) + i\theta\bar{\theta}\mathcal{F}(\hat{x}) \tag{1.15}$$

where $\hat{x}_\mu = x_\mu + \frac{i}{2}\bar{\theta}\gamma_5\gamma_\mu\theta$ and the θ are anti-commuting Grassmann numbers which, along with x, make up an extension to spacetime called *superspace*. Interactions among such superfields may be included by introducing the superpotential, $\hat{f}$ which

can be chosen by the model builder. Combining this with 1.13, the guaranteed supersymmetric Lagrangian then becomes

$$\begin{aligned}
\mathcal{L}_{chiral} &= \partial_\mu \mathcal{S}^\dagger \partial^\mu \mathcal{S} + \frac{i}{2}\bar{\psi}\not{\partial}\psi + \mathcal{F}^\dagger\mathcal{F} && (1.16)\\
&- i\sum_i \frac{\partial \hat{f}}{\partial \hat{\mathcal{S}}}\bigg|_{\hat{\mathcal{S}}=\mathcal{S}} \mathcal{F}_i - \frac{1}{2}\sum_{i,j}\frac{\partial^2 \hat{f}}{\partial\hat{\mathcal{S}}_i\partial\hat{\mathcal{S}}_j}\bigg|_{\hat{\mathcal{S}}=\mathcal{S}}\bar{\psi}_i P_L \psi_j \\
&+ i\sum_i \left(\frac{\partial \hat{f}}{\partial \hat{\mathcal{S}}_i}\right)^\dagger\bigg|_{\hat{\mathcal{S}}=\mathcal{S}} \mathcal{F}_i^\dagger - \frac{1}{2}\sum_{i,j}\left(\frac{\partial^2 \hat{f}}{\partial\hat{\mathcal{S}}_i\partial\hat{\mathcal{S}}_j}\right)\bigg|_{\hat{\mathcal{S}}=\mathcal{S}}\bar{\psi}_i P_R \psi_j && (1.17)
\end{aligned}$$

The curl supermultiplet, sometimes called the gauge (when applied in a gauge theory as will be the case in this dissertation) or vector supermultiplet, contains the gauge fields of the theory. It contains a field strength tensor $F_{\mu\nu}$ containing the vector field V_μ, a Majorana field λ, and an auxiliary field $\mathcal{D}$. The Majorana field λ is called a *gaugino*, and will be the fermionic partner to the SM gauge bosons. The spin zero bosonic field $\mathcal{D}$ will play the same role as $\mathcal{F}$ in the chiral Lagrangian. A general gauge Lagrangian will take the form

$$\mathcal{L}_{gauge} = -\frac{1}{4}F_{A\mu\nu}F_A^{\mu\nu} + \frac{i}{2}\bar{\lambda}_A \not{D}_{AC}\lambda_C + \frac{1}{2}\mathcal{D}_A\mathcal{D}_A, \tag{1.18}$$

where D is the gauge covariant derivative, given by

$$(\not{D}\lambda)_A = \not{\partial}\lambda_A + igf_{ABC}\not{V}_B\lambda_C. \tag{1.19}$$

The SUSY transformations of these fields are

$$\begin{aligned}
\delta F^{\mu\nu} &= -i\bar{\alpha}[\gamma^\nu\partial^\mu - \gamma^\mu\partial^\nu], \\
\delta\lambda &= -i\gamma_5\alpha\mathcal{D} + \frac{1}{4}[\gamma_\nu,\gamma_\mu]F^{\mu\nu}\alpha, && (1.20)\\
\delta\mathcal{D} &= \bar{\alpha}\not{\partial}\gamma_5\lambda. && (1.21)
\end{aligned}$$

The three fields in the curl supermultiplet can be combined into a *curl superfield* in a similar way as the chiral superfield. The curl superfield $\hat{W}_A(\hat{x})$ in the Wess-Zumino gauge is given by

$$\hat{W}_A(\hat{x}) = \lambda_{LA}(\hat{x}) + \frac{1}{2}\gamma^\mu\gamma^\nu F_{\mu\nu A}(\hat{x})\theta_L - i\bar{\theta}\theta_L(\not{D}\lambda_R)_A - i\mathcal{D}_A(\hat{x})\theta_L. \tag{1.22}$$

The action for supersymmetric gauge theories can be written as an integral over superspace. One finds

$$\begin{aligned} S = & - \frac{1}{4}\int d^4x d^4\theta \left[\hat{\mathcal{S}}^\dagger e^{-2gt_A\hat{\Phi}_A}\hat{\mathcal{S}}\right] & (1.23)\\ & - \frac{1}{2}\left[\int d^4x d^2\theta_L \hat{f}(\hat{\mathcal{S}} + h.c.)\right] - \frac{1}{4}\int d^4x d^2\theta_L \overline{\hat{W}_A^c}\hat{W}_A, & (1.24)\end{aligned}$$

where $\hat{\Phi}_A$ is a set of gauge potential superfields in which the vector potential resides and the t_A are matrix representations of the generators of the gauge group that satisfy the Lie algebra $[t_A, t_B] = if_{ABC}t_C$. Also allowed, but not shown, are Fayet-Iliopoulos terms which appear for each $U(1)$ factor of the gauge group.

The complete SUSY Lagrangian for a renormalizable gauge theory will take the form

$$\begin{aligned} \mathcal{L} &= \mathcal{L}_{chiral} + \mathcal{L}_{gauge} + \mathcal{L}_{int} \\ &= (D_\mu\mathcal{S})^\dagger(D^\mu\mathcal{S}) + \frac{i}{2}\bar{\psi}\not{D}\psi + \mathcal{F}^\dagger\mathcal{F} - \frac{1}{4}F_{A\mu\nu}F_A^{\mu\nu} + \frac{i}{2}\bar{\lambda}_A\not{D}_{AC}\lambda_C + \frac{1}{2}\mathcal{D}_A\mathcal{D}_A \\ &+ \sum_i\left[-\sqrt{2}\left(\mathcal{S}_i^\dagger g t_A\bar{\lambda}_A\frac{1-\gamma_5}{2}\psi_i + h.c.\right) + \mathcal{S}_i^\dagger g t_A\mathcal{S}_i\right] \qquad (1.25)\\ &- i\sum_i\frac{\partial\hat{f}}{\partial\hat{\mathcal{S}}}\bigg|_{\hat{\mathcal{S}}=\mathcal{S}}\mathcal{F}_i - \frac{1}{2}\sum_{i,j}\frac{\partial^2\hat{f}}{\partial\hat{\mathcal{S}}_i\partial\hat{\mathcal{S}}_j}\bigg|_{\hat{\mathcal{S}}=\mathcal{S}}\bar{\psi}_i P_L\psi_i \\ &+ i\sum_i\left(\frac{\partial\hat{f}}{\partial\hat{\mathcal{S}}_i}\right)^\dagger\bigg|_{\hat{\mathcal{S}}=\mathcal{S}}\mathcal{F}_i^\dagger - \frac{1}{2}\sum_{i,j}\left(\frac{\partial^2\hat{f}}{\partial\hat{\mathcal{S}}_i\partial\hat{\mathcal{S}}_j}\right)\bigg|_{\hat{\mathcal{S}}=\mathcal{S}}\bar{\psi}_i P_R\psi_j. \end{aligned}$$

Here i, j denote the matter field types and A is the gauge group index. Once again,

the Fayet-Iliopoulos terms are not included.

Symmetries other than SUSY must also be considered when constructing a supersymmetric Lagrangian, such as lepton and baryon number conservation. These can be broken by non-perturbative effects in general SUSY theories, but should be conserved at this level to prevent rapid decay rates of the proton. A symmetry that will remove B and L violating terms from the SUSY Lagrangian is matter parity, which is the same as R-parity, defined by

$$R \equiv (-1)^{3(B-L)+2s}, \tag{1.26}$$

where s is the spin of the field. Here, squark, slepton, gaugino, and higgsino fields are odd, whereas the matter, gauge, and Higgs fields are even. For the remainder of this dissertation, R-parity is assumed to be conserved in nature. This implies that the lightest supersymmetric (LSP) in R-parity conserving models is stable. When constructing soft breaking terms, these symmetries are necessarily conserved.

In addition to the protection of symmetries, there are other constraints on SUSY that must be taken into consideration when considering the phenomenological features of the theory. Collider experiments put limits on decays such as $b \to s\gamma$ and $B_S \to \mu^+\mu^-$ give high precision flavor limits by which model builders must abide. LEP2 constraints put a limit on lightest chargino mass $m_{\widetilde{W}_1} > 103.5$ GeV [25] in addition to the squark and gluon constraints mentioned earlier (these particles will be introduced in Sec 1.2.3). Cosmological observations may also put limits on SUSY through dark matter direct and indirect detection.

1.2.2 SUSY Breaking

If supersymmetry were unbroken, the known particles would each have a superpartner of the same mass. Experimentally this is not the case, and supersymmetry must

be a broken symmetry, giving larger masses to the superpartners. Broken SUSY arises spontaneously if the F or D terms in the Lagrangian acquire *vev*s, however, such breaking cannot be realized in accord with phenomenology for global SUSY models. One must move to local SUSY or supergravity (SUGRA) models. Then SUSY could be broken in some *hidden sector* which couples to the *visible sector*. The hidden sector would be essentially decoupled from the our world, and only communicated to the visible sector through messenger interactions. There are many models which employ this method of SUSY breaking, with the most studied being *gravity mediation*.

In gravity mediated scenarios, gravitational interactions act as the mediator between the two sectors. The gravity force carrier is the spin 2 graviton, and its supersymmetric partner is the spin 3/2 gravitino. This is the case in supergravity models, such as mSUGRA/CMSSM along with its extensions, such as the Non-Universal Higgs Mass (NUHM) model which will be discussed further in Sec. 1.2.4. In these models, for a suitably chosen superpotential, SUGRA can be broken at a mass scale $m \sim 10^{11}$ GeV and gives rise to supersymmetric Goldstone bosons called goldstinos. The goldstino degrees of freedom are absorbed by the gravitino, giving it a mass $m_{3/2}$. The visible sector soft terms are then of order $m^2/M_{\rm Pl}$, where the Planck mass $M_{\rm Pl} \simeq 1.2 \times 10^{19}$ GeV.

Without knowledge of the actual supersymmetry breaking mechanism, we can parameterize the effects of SUSY breaking by adding to the Lagrangian *soft SUSY breaking* (SSB) terms. These terms must include all possible SUSY breaking terms, however they are required to respect the desired symmetries (such as lepton and baryon number) at the SUSY breaking scale. It is also required that they do not re-introduce quadratic divergences into the theory. In this way, SUSY is explicitly broken, however particular models of SUSY breaking may still be communicated into the soft terms. For example, in gravity mediated theories, the soft term masses

are proportional to the gravitino mass $m_{3/2}$ which is assumed to lie around the TeV scale.

1.2.3 The Minimal Supersymmetric Standard Model

The Minimal Supersymmetric Standard Model (MSSM) is the direct supersymmetric extension of the Standard Model, introducing the minimum number of extra particles and interactions to the theory. Supersymmetry is broken by adding to the theory all allowed soft SUSY breaking terms. The gauge symmetry of the MSSM is chosen to be $SU(3)_C \times SU(2)_L \times U(1)_Y$, which is also the Standard Model gauge symmetry. Table 1 lists the fields in the MSSM, along with the SM particles and their supersymmetric partners. For a full treatment of the MSSM see, for example, [24].

The MSSM requires the introduction of two Higgs doublets, the reason being twofold: 1. in SUSY, a doublet can only give mass to either the up-type quarks or the down-type quarks and leptons, a single doublet cannot do both, and 2. the doublets each carry higgsinos which can circulate in triangle anomalies. This upsets the delicate anomaly cancellation that occurs in the SM model, therefore one set of higgsinos with $Y = 1/2$ must be paired by a second with $Y = -1/2$. These appear in a chiral supermultiplet, consisting of both scalar/pseudo-scalar Higgs bosons and higgsinos. Before symmetry breaking the two Higgs doublets are specified as being up-type with mass m_{H_u} or down-type with mass m_{H_d}. Electroweak symmetry is broken when $m^2_{H_u}$ is driven to negative values via renormalization group equation (RGE) running. At this point the neutral scalar fields each acquire a *vev*, $\langle h^0_u \rangle \equiv v_u$ and $\langle h^0_d \rangle \equiv v_d$. Thus we define a new parameter,

$$\tan\beta \equiv \frac{v_u}{v_d} \tag{1.27}$$

After the electroweak symmetry is broken five physical Higgs states remain, the light

Higgs scalar h (typically associated with the SM Higgs), the heavy Higgs scalar, two charged Higgs $H^{\pm}$, and a pseudo-scalar Higgs A. The fermionic partners of the Higgs are the *higgsinos*. The supersymmetric Higgs/higgsino bilinear term μ gives mass to both SM particles (the gauge and Higgs bosons) and the SUSY partner higgsinos. This arises from the superpotential term

$$\hat{f} \ni \mu(\hat{h}_u^0 \hat{h}_d^0 + \hat{h}_u^+ \hat{h}_d^-). \tag{1.28}$$

The gauge sector of the MSSM is built up of three curl superfields, $\hat{B}_\mu, \hat{W}_\mu^a$, and $\hat{g}_\mu^A$. These correspond to the $U(1)_Y, SU(2)_L$, and $SU(3)_C$ symmetries, respectively. The Lagrangian contribution from the soft SUSY breaking gaugino masses is

$$\mathcal{L}_{mass} = -\frac{1}{2}[M_1 \bar{\lambda}_0 \lambda_0 + M_2(\bar{\lambda}_3 \lambda_3 + 2\bar{\lambda}\lambda) + M_3 \bar{\tilde{g}} \tilde{g}]. \tag{1.29}$$

Here, M_1, M_2, and M_3 are the bino, wino, and gluino mass parameters. The gluino is the only color octet fermion; since $SU(3)_C$ is not broken, it cannot mix with any other fermion and is therefore a mass eigenstate with $m_{\tilde{g}} = |M_3|$.

The bino, winos, and higgsinos mix to give physical mass eigenstates, the four neutralinos ($\widetilde{Z}_{1,2,3,4}$) and four charginos ($\widetilde{W}_{1,2}^{\pm}$). The charginos and neutralinos are labeled according to increasing mass, with $\widetilde{Z}_1(\widetilde{W}_1)$ the lightest and $\widetilde{Z}_4(\widetilde{W}_2)$ the heaviest. These masses depend on the complex mixing patterns of M_1, M_2, μ, and $\tan\beta$, however they can be described as gaugino-like, higgsino-like, or some mixture. If $|M_{1,2}| \gg |\mu|, m_W$, then the lighter chargino and two lighter neutralinos are higgsino-like, and the heavier chargino and two heavier neutralinos are gaugino-like. If $|\mu| \gg |M_{1,2}|, m_W$, then the situation is reversed.

Partnered to the leptons are the sleptons, such as the scalar electron (selectron), scalar electron neutrino (sneutrino), etc. The partners to the quarks are called *squarks*, including the stop, sbottom, etc. As a whole, these are sometimes referred

Field	spin 0	spin 1/2	$SU(3)_C$	$SU(2)_L$	$U(1)_Y$
$\hat{L} = \begin{pmatrix} \hat{\nu}_{eL} \\ \hat{e}_L \end{pmatrix}$	$(\tilde{\nu}\ \tilde{e}_L)$	$(\nu\ e_L)$	**1**	**2**	-1
$\hat{E}^c$	$\tilde{e}^*_R$	$e^\dagger_R$	**1**	**1**	2
$\hat{Q} = \begin{pmatrix} \hat{u}_L \\ \hat{d}_L \end{pmatrix}$	$(\tilde{u}_L\ \tilde{d}_L)$	$(u_L\ d_L)$	**3**	**2**	1/3
$\hat{U}^c$	$\tilde{u}^*_R$	$u^\dagger_R$	$\mathbf{3}^*$	**1**	-4/3
$\hat{D}^c$	$\tilde{d}^*_R$	$d^\dagger_R$	$\mathbf{3}^*$	**1**	2/3
$\hat{H}_u = \begin{pmatrix} \hat{h}^+_u \\ \hat{h}^0_u \end{pmatrix}$	$(\tilde{h}^+_u\ \tilde{h}^0_u)$	$(h^+_u\ h^0_u)$	**1**	**2**	1
$\hat{H}_d = \begin{pmatrix} \hat{h}^-_d \\ \hat{h}^0_d \end{pmatrix}$	$(\tilde{h}^-_d\ \tilde{h}^0_d)$	$(h^-_d\ h^0_d)$	**1**	$\mathbf{2}^*$	-1

Table 1: The matter and Higgs chiral supermultiplet content in the MSSM for one generation.

Field	spin 1/2	spin 1	$SU(3)_C$	$SU(2)_L$	$U(1)_Y$
$\hat{g}_A$ A=1,...,8	$\tilde{g}$	g	**8**	**1**	0
$\hat{W}_a$, a=1,2,3	$\tilde{W}^\pm\ \tilde{W}^0$	$W^\pm\ W^0$	**1**	**3**	0
$\hat{B}$	$\tilde{B}$	B	**1**	**1**	0

Table 2: The gauge supermultiplets in the MSSM.

to as *sfermions*. Just as in the SM, the sfermions appear in three generations.

Within the MSSM there are 124 free parameters. One of the successes of the MSSM is gauge coupling unification at the grand unified theory (GUT) scale $m_{\rm GUT} \simeq 2 \times 10^{16}$ GeV. One may then assume that the MSSM is the correct effective field theory describing nature from the electroweak scale $Q = 1$ TeV to the high scale (HS) $Q = m_{\rm GUT}$. Motivated by the universality of gravity and by the phenomenological need to suppress FCNC and CP violating processes, many physicists

adopt the universality hypothesis, defining at the GUT scale

$$\begin{aligned} g = g' = g_S &\equiv g_{\rm GUT} \\ m^2_{Q_i} = m^2_{U_i} = m^2_{D_i} = m^2_{L_i} = m^2_{E_i} = m^2_{H_u} = m^2_{H_d} &\equiv m^2_0 \\ M_1 = M_2 = M_3 &\equiv m_{1/2} \\ A_t = A_b = A_\tau &\equiv A_0. \end{aligned}$$

This assumption greatly simplifies the parameter space. Now it is possible to specify just five parameters, $m_0, m_{1/2}, A_0, sign(\mu), \tan\beta$, to fully determine the weak scale spectra of the theory. This is called mSUGRA (minimal SUperGRAvity), or CMSSM (Constrained MSSM) model. Through renormalization group equation (RGE) running, the term $m^2_{H_u}$ evolves from large m^2_0 through zero to negative values, breaking electroweak symmetry. The RGE running is heavily dependent on the radiative corrections, therefore this mechanism is referred to as *radiative electroweak symmetry breaking* (REWSB) [26].

The MSSM may be embedded within a larger framework, such as a GUT or string model. Since the MSSM is free of quadratic divergences, masses at the weak scale remain stable under radiative corrections and allow the predictions of the MSSM to be extended to the HS. However, logarithmic divergences will still remain, and for energies $Q \sim m_{\rm GUT}$ calculations will contain terms proportional to $\frac{\alpha_i}{4\pi}\log(m_{\rm GUT}/m_Z)$. These large logarithms will become a part of the discussion of fine-tuning in SUSY in Chapter 2.

1.2.4 Extensions and Alternatives to mSUGRA

Another model, the Non-Universal Higgs Mass (NUHM) model is included in the supergravity class of models. Within the NUHM framework, one may make the choice of additional free parameters such that the GUT scale Higgs masses are not

equal to the common scalar mass m_0. NUHM models may have one, two, or three extra parameters where:

- NUHM1 [27] has $m_{H_u}^2 = m_{H_d}^2 \neq m_0^2$ at the GUT scale.
- NUHM2 [28] has two free parameters leading to non-universal Higgs masses, $m_{H_u}^2 \neq m_{H_d}^2 \neq m_0^2$. This leads to a parameter set consisting of

$$m_0, m_{1/2}, A_0, \tan\beta, m_{H_u}^2, m_{H_d}^2 \tag{1.30}$$

- NUHM3 is the same as NUHM2, but with different values m_0^2 for the third generation from the first and second, i.e. $m_0^2(3) \neq m_0^2(1,2)$.

The NUHM models are the focus of Chapter 3.

A popular model that includes solving the Strong CP Problem by introducing axions (a) is the Peccei-Quinn MSSM (PQMSSM). The partners to the axion are the saxion ($\tilde{s}$) and axino ($\tilde{a}$) [29, 30, 31, 32]. This model will be discussed further in Chapter 6.

2 Naturalness in SUSY [33, 34]

The ultra-violet properties of softly broken SUSY theories, with SUSY broken near the weak scale, ensures that the low energy theory is at most logarithmically sensitive to high scale (HS) physics. The realization [35] that weak scale SUSY solves the big gauge hierarchy problem endemic to the SM [36], embedded into a high scale framework, provided much impetus for its study over the last three decades. Thus, the question arises: are SUSY models now unnatural, and if so, how unnatural are they? Or, do there exist portions of parameter space where SUSY remains natural? If so, a credible goal of collider [37, 38] and dark matter [39] search experiments is to leave no stone unturned in the search for natural SUSY. Although some authors maintain that naturalness is inherently subjective, it is shown here that this is not so by examining several different proposed measures. One finds that – if applied properly – all measures agree with one another and allow for much heavier top squarks than previously considered.

2.1 Standard Model Fine-Tuning

In the SM, the mass of the Higgs boson can be calculated as the sum of the tree level contributions and the radiative corrections:

$$m_h^2 = m_{h\ tree}^2 + \delta m_{h\ rad}^2. \tag{2.1}$$

where the quadratically divergent radiative corrections

$$\delta m_{h\ rad}^2 \simeq \frac{3}{4\pi^2}\left(-\lambda_t^2 + \frac{g^2}{4} + \frac{g^2}{8\cos^2\theta_W} + \lambda\right)\Lambda^2 \tag{2.2}$$

are independent of the tree level Higgs mass (here, λ_t is the SM top Yukawa coupling, g is the $SU(2)_L$ gauge coupling, λ is the SM Higgs quartic coupling and Λ is the

effective theory energy cutoff scale). A SM fine-tuning measure can be defined as

$$\Delta_{SM} \equiv \delta m_{h\ rad}^2/(m_h^2/2). \tag{2.3}$$

One may require a fine-tuning with $\Delta_{SM} \approx 1$, thus for large Λ the large radiative corrections must be balanced by the fine tuning of $m_{h\ tree}^2$. Alternatively, $\delta m_{h\ rad}^2 \sim m_{h\ tree}^2$, requiring $\Lambda \sim 1$ TeV and the SM should only be valid up to the TeV scale.

2.2 Electroweak Fine-Tuning $\Delta_{\rm EW}$

The value of m_Z that is obtained from the minimization of the one-loop-corrected Higgs boson potential

$$\frac{m_Z^2}{2} = \frac{m_{H_d}^2 + \Sigma_d^d - (m_{H_u}^2 + \Sigma_u^u)\tan^2\beta}{\tan^2\beta - 1} - \mu^2, \tag{2.4}$$

is the starting point for most discussions of fine-tuning [5,6,10] in the MSSM and its extensions. This expression is obtained using the weak scale MSSM Higgs potential and all parameters in Eq. (2.4) are evaluated at the scale $Q = M_{SUSY}$. The Σs in Eq. (2.4) arise from one loop corrections to the Higgs potential. Explicit forms for the Σ_u^u and Σ_d^d are given in the Appendix of Ref. [40]. Requiring that the observed value of m_Z is obtained without large cancellations between the various terms on the right-hand-side of (2.4) leads to the suggestion of

$$\Delta_{\rm EW} \equiv max_i \left|C_i\right| /(m_Z^2/2)\ , \tag{2.5}$$

as a measure of fine-tuning. Here, $C_{H_d} = m_{H_d}^2/(\tan^2\beta{-}1)$, $C_{H_u} = -m_{H_u}^2\tan^2\beta/(\tan^2\beta{-}1)$ and $C_\mu = -\mu^2$. Also, $C_{\Sigma_u^u(k)} = -\Sigma_u^u(k)\tan^2\beta/(\tan^2\beta - 1)$ and $C_{\Sigma_d^d(k)} = \Sigma_d^d(k)/(\tan^2\beta{-}1)$, where k labels the various loop contributions included in Eq. (2.4). By studying (2.4) one sees that for low $\Delta_{\rm EW}$ we must have low $\mu^2 \sim m_Z^2$ so that

higgsino masses are necessarily bounded from above.

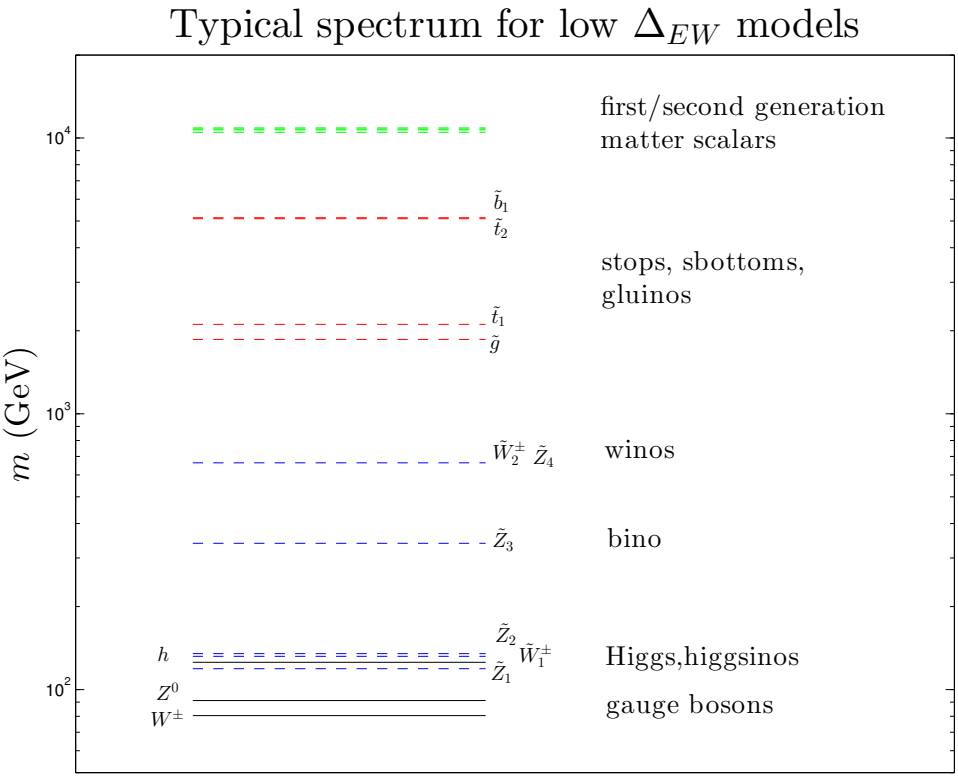


Figure 1: Typical mass spectrum from low $\Delta_{\rm EW}$ models.

The fine-tuning measure $\Delta_{\rm EW}$ has several attractive features that merit consideration.

- *Model independent* (within the context of models which reduce to the MSSM at the weak scale): $\Delta_{\rm EW}$ is essentially determined by the sparticle spectrum [41], and – unlike other measures of fine-tuning – does not depend on the mechanism by which sparticles acquire masses. Since $\Delta_{\rm EW}$ is determined only from weak scale Lagrangian parameters, the phenomenological consequences which may be derived by requiring low Δ_{EW} will apply not only for the NUHM2 model considered here, but also for other possibly more complete (or less complete, such as pMSSM) models which lead to look-alike spectra at the weak scale.

- *Conservative*: $\Delta_{\rm EW}$ captures the minimal fine-tuning that is necessary for any given sparticle spectrum, and so leads to the most conservative conclusions regarding fine-tuning considerations.

- *Measureable*: $\Delta_{\rm EW}$ is in principle measurable, in that it can be evaluated if the underlying weak scale parameters can be extracted from data.

- *Unambiguous*: Fine-tuning measures which depend on high scale parameter choices are highly sensitive to exactly which set of model input parameters one adopts. There is no such ambiguity in the fine-tuning sensitivity as measured by both $\Delta_{\rm EW}$.

- *Predictive*: While $\Delta_{\rm EW}$ is less restrictive than than another measure of fine-tuning Δ_{HS} (introduced in Sec. 2.3), it still remains highly restrictive. The requirement of low Δ_{EW} highly disfavors models such as mSUGRA/CMSSM [41], while allowing for very distinct predictions from more general models such as NUHM2.

- *Falsifiable*: The most important prediction from requiring low Δ_{EW} is that $|\mu|$ cannot be too far removed from m_Z. This implies the existence of light higgsinos $\sim 100-300$ GeV which are hard to see at hadron colliders, but which are easily detected at a linear e^+e^- collider with $\sqrt{s} \gtrsim 2|\mu|$.

- *Simple to calculate*: $\Delta_{\rm EW}$ is extremely simple to encode in sparticle mass spectrum programs, even if one adopts models with very large numbers of input parameters.

Fig. 1 shows see the typical SUSY spectra that occurs in models with low $\Delta_{\rm EW}$. As expected by the condition $\mu^2 \sim m_Z^2$, the higgsinos are roughly of the same order as the SM gauge bosons and the Higgs. The stops, sbottoms and gluinos lie $\sim 1-5$ TeV, safely above current collider limits.

Before proceeding further, note that $\Delta_{\rm EW}$ as defined here entails only weak scale parameters, and therefore has no information about the $\log\Lambda$ terms mentioned in Sec. 1.2.3 that cause weak scale physics to exhibit logarithmic sensitivity to HS physics. Since many broad features of the phenomenology are determined by the spectrum, much of the phenomenology of the (unknown) underlying theory is the same as those of the NUHM2 model with the same spectrum.

2.3 Fine-Tuning of the Higgs mass

In the MSSM, it is found that,

$$m_h^2 \simeq \mu^2 + m_{H_u}^2|_{tree} + \delta m_{H_u}^2|_{rad}, \tag{2.6}$$

where now μ^2 is the supersymmetric Higgs/higgsino bilinear term mentioned earlier. If one assumes the MSSM is valid up to the GUT scale, then the value of $\delta m_{H_u}^2$ can be found by integrating the renormalization group equation [42]

$$\frac{dm_{H_u}^2}{dt} = \frac{1}{8\pi}\left(-\frac{3}{5}g_1^2M_1^2 - 3g_2^2M_2^2 + \frac{3}{10}g_1^2S + 3f_t^2X_t\right) \tag{2.7}$$

where $t = \sqrt{Q^2/Q_0^2}$, $S = m_{H_u}^2 - m_{H_d}^2 + Tr[\mathbf{m}_Q^2 - \mathbf{m}_L^2 - 2\mathbf{m}_U^2 + \mathbf{m}_D^2 + \mathbf{m}_E^2]$, and $X_t = m_{Q_3}^2 + m_{U_3}^2 + m_{H_u}^2 + A_t^2$. Neglecting the gauge terms, the S term, the $m_{H_u}^2$ contribution to X_t, and the fact that f_t and the soft terms evolve under Q^2 variation, equation 2.7 can be integrated to give

$$\delta m_{H_u}^2|_{rad} \simeq -\frac{3f_t^2}{8\pi^2}(m_{Q_3}^2 + m_{U_3}^2 + A_t^2)\ln\left(\Lambda^2/M_{\rm SUSY}^2\right). \tag{2.8}$$

Here, Λ is again the cut-off scale which may be taken as high as $m_{\rm GUT}$ or even the reduced Planck mass $M_P \simeq 2.4\times10^{18}$ GeV in models with a high scale origin, or close to $M_{SUSY}^2 \simeq m_{\tilde{t}_1}m_{\tilde{t}_2}$. By requiring the measure $\Delta_{\rm HS}$ [15, 17]$\sim \delta m_{H_u}^2/(m_h^2/2) \lesssim 10$,

one expects $m_{\tilde{t}_{1,2}\tilde{b}_1} \lesssim 600$ GeV. Using $\Delta_{\rm HS}$ along with $m_h \simeq 125$ GeV, some popular SUSY models are fine-tuned to 0.1%.

This case is different from the SM case because $m^2_{H_u}$ and $\delta m^2_{H_u\ rad}$ are *not independent*. Therefore, using $\Delta_{\rm HS}$ could lead to the erroneous conclusion that the model is fine-tuned. If, instead, these two terms are grouped together, then

$$(m^2_{H_u} + \delta m^2_{H_u\ rad}) = m^2_{H_u}. \tag{2.9}$$

Such a regrouping of terms leads back to the $\Delta_{\rm EW}$ measure.

2.4 Barbieri-Giudice Fine-Tuning $\Delta_{\rm BG}$

The traditional fine-tuning measure Δ_{BG}, introduced over 25 years ago [5, 6, 8], uses fractional change in the output value of m_Z^2 given by (2.4) relative to the corresponding change in the input parameters, and is defined by,

$$\Delta_{\rm BG} \equiv max_i|B_i| = \left|\frac{\partial \ln m_Z^2}{\partial \ln c_i}\right| = max_i \left|\frac{c_i}{m_Z^2}\frac{\partial m_Z^2}{\partial c_i}\right| . \tag{2.10}$$

Here, the c_i constitute the fundamental parameters of the theory. These would be the weak scale parameter set in the case of the pMSSM, but the HS parameter set for models such as mSUGRA. If the dependence of m_Z^2 on a_i is linear as in (2.4) with weak scale MSSM parameters as inputs, $\Delta_{\rm BG}$ coincides with $\Delta_{\rm EW}$ at the tree-level. An advantage for $\Delta_{\rm BG}$ over $\Delta_{\rm HS}$ is that it maintatins the correlation between $m^2_{H_u}$ and $\delta m^2_{H_u\ rad}$ by its expression in terms of the high scale parameters.

To evaluate $\Delta_{\rm BG}$ in HS models, one needs to know the explicit dependence of the weak scale parameters on the fundamental parameters. At tree-level, for moderate to large values of $\tan\beta$, the $m^2_{H_d}$ term in the expression for m_Z^2 is unimportant, and so, to a good approximation, one needs only the $m^2_{H_u}$ and μ^2 in terms of the HS parameters. Expressions for these can be gained by semi-analytic solutions to the

one-loop renormalization group equations, as found for instance in Refs [43]. For instance, for $\tan\beta = 10$, it is found in Ref. [44, 45, 46] that

$$-2\mu^2(m_{\rm weak}) = -2.18\mu^2 \tag{2.11}$$

$$\begin{aligned}
-2m_{H_u}^2(m_{\rm weak}) = {} & 3.84M_3^2 + 0.32M_3M_2 + 0.047M_1M_3 - 0.42M_2^2 \\
& +0.011M_2M_1 - 0.012M_1^2 - 0.65M_3A_t - 0.15M_2A_t \\
& -0.025M_1A_t + 0.22A_t^2 + 0.004M_3A_b \\
& -1.27m_{H_u}^2 - 0.053m_{H_d}^2 \\
& +0.73m_{Q_3}^2 + 0.57m_{U_3}^2 + 0.049m_{D_3}^2 - 0.052m_{L_3}^2 + 0.053m_{E_3}^2 \\
& +0.051m_{Q_2}^2 - 0.11m_{U_2}^2 + 0.051m_{D_2}^2 - 0.052m_{L_2}^2 + 0.053m_{E_2}^2 \\
& +0.051m_{Q_1}^2 - 0.11m_l{U_1}^2 + 0.051m_{D_1}^2 - 0.052m_{L_1}^2 + 0.053m_{E_1}^2,
\end{aligned} \tag{2.12}$$

where the parameters on the right-hand-side are evaluated at the GUT scale. For different values of $\tan\beta$, the functional form on the right-hand-side is the same except for somewhat different values of the coefficients. Substituting this into the tree level expression for m_Z^2, it is straightforward to evaluate the derivatives in Eq. (2.10), and Δ_{BG} can be calculated using any sparticle mass spectrum code which includes solving the MSSM coupled RGEs starting from the GUT scale. For the mSUGRA model where the GUT scale scalar mass parameters are universal, the scalar mass squared terms coincidentally sum to just $0.013m_0^2$.

Note that the parameters in Eq. 2.13 may even be further correlated. For any fully specified hidden sector in supergravity theories, one expects each SSB param-

eter to be some multiple of $m_{3/2}$: *e.g.*

$$\begin{aligned} m_{H_u}^2 &= a_{H_u} \cdot m_{3/2}^2 && (2.13)\\ m_{Q_3}^2 &= a_{Q_3} \cdot m_{3/2}^2 && (2.14)\\ m_{A_t}^2 &= a_{A_t} \cdot m_{3/2} && (2.15)\\ M_i &= a_i \cdot m_{3/2} && (2.16)\\ &\cdots . && (2.17) \end{aligned}$$

Here, the coefficients a_i parameterize ignorance of the exact model for SUSY breaking. By using several adjustable parameters, a wide net is cast which encompasses a large range of hidden sector SUSY breaking possibilites. Using these terms, Eq. 2.13 can be rewritten as

$$m_Z^2 = -2.18\mu^2 + a \cdot m_{3/2}^2 \qquad (2.18)$$

where now a is just some number which is the sum of all of the coefficients of the terms $\propto m_{3/2}^2$, assuming μ is independent of $m_{3/2}$. Now, naturalness simply requires a small value of a such that

- $m_z^2 \sim a \cdot m^2 3/2$

and

- $m_z^2 \sim \mu^2$.

The first of these implies $m_{3/2}^2 \sim m_Z^2$ or a quite small. The former is unlikely due to the lack of SUSY signal at LHC, while in the latter case the SUSY soft terms conspire such that there are large cancellations among the various coefficients of $m_{3/2}^2$. This is what occurs in radiatively-driven natural SUSY, which will be introduced in the next chapter. One may equate the value of m_Z^2 in terms of weak scale parameters

with the value of m_Z^2 in terms of GUT scale parameters:

$$m_Z^2 \simeq -\mu^2(weak) - m_{H_u}^2(weak) \simeq -2.18\mu^2(GUT) + a \cdot m_{3/2}^2. \tag{2.19}$$

Since μ hardly evolves under RG running, then the BG condition for low fine-tuning is

$$-m_{H_u}^2(weak) \sim a \cdot m_{3/2}^2 \sim m_Z^2, \tag{2.20}$$

i.e. that the value of $m_{H_u}^2$ must be driven to small negative values $\sim -m_Z^2$ at the weak scale. These are exactly the conditions required by the $\Delta_{\rm EW}$ measure. In other words,

$$\lim_{n_{SSB}\to 1} \Delta_{\rm BG} \to \Delta_{\rm EW} \tag{2.21}$$

where n_{SSB} is the the number of independent soft SUSY breaking terms. Therefore, if applied properly, $\Delta_{\rm BG} \to \Delta_{\rm EW}$ and $\Delta_{\rm HS} \to \Delta_{\rm EW}$.

3 Radiative Natural Supersymmetry [40, 47]

Spectra from low Δ_{EW} models are characterized by (as seen in Fig 1):

- four light higgsinos $\widetilde{W}_1^{\pm}$, $\widetilde{Z}_1$ and $\widetilde{Z}_2$ with mass $\sim \mu \sim 100 - 300$ GeV,
- well-mixed top and bottom squarks in the few TeV regime,
- $m_{\tilde{g}} \lesssim 2 - 4$ TeV and
- first/second generation squarks and sleptons in the $5 - 30$ TeV regime, consistent with at least a partial decoupling solution to the SUSY flavor, CP, gravitino and p-decay problems [48, 49].

Models with such spectra have been described as radiatively-driven natural supersymmetry (RNS) models since the value of $m_{H_u}^2$ is radiatively driven to values close to m_Z^2. RNS spectra can be realized in the 2-extra-parameter non-universal Higgs models (NUHM2), but not in more constrained models such as mSUGRA/CMSSM. For the case of mSUGRA, while μ can become low in the HB/FP region, the rather heavy top squarks $m_{\tilde{t}_{1,2}} \sim 7-15$ TeV produce large $\Sigma_u^u(\tilde{t}_{1,2})$ leading again to substantial fine-tuning [41]. An example may be seen in Fig. 2. Plotted here are the contributions to m_Z^2 from the mSUGRA/CMSSM model and RNS model scaled to $m_Z^2/2$ for $m_0 = 7025$ GeV, $m_{1/2} = 568.3$ GeV, $A_0 = -11426.6$ GeV, and $\tan\beta = 8.55$. Red bars denote negative contributions, while blue bars denote positive contributions. In frame *a*), the situation is shown for the mSUGRA model (parameters as above with $m_{H_u} = m_{H_d} = m_0$). The value of μ^2 must be fine-tuned so that a large, unnatural cancellation between $m_{H_u}^2$ and μ^2 is needed to obtain a Z mass of just 91.2 GeV. In frame *b*), the case is shown for RNS with the same parameters as mSUGRA but with $\mu = 150$ GeV and where now $m_{H_u}(\Lambda) \neq m_{H_d}(\Lambda) \neq m_0$. All contributions are now roughly comparable, so that it is easy to understand why m_Z and m_h both naturally occur around ~ 100 GeV.

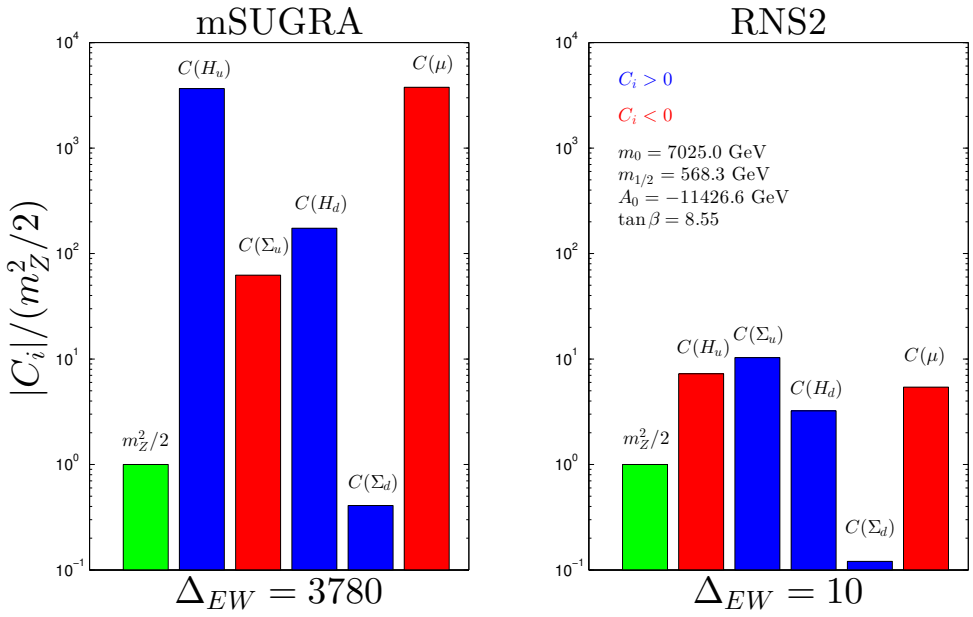


Figure 2: Plot of contributions to $m_Z^2/2$ from the mSUGRA/CMSSM model with parameters as listed, and also for the RNS2 benchmark point with the same $m_0, m_{1/2}, A_0$, and $\tan\beta$ values but with $\mu = 150$ GeV. Red bars denote negative contributions, while blue bars denote positive contributions.

The RNS model automatically maintains the SUSY success stories of gauge coupling unification and radiative breaking of electroweak symmetry due to a large top quark mass. These features require the MSSM as the effective field theory from M_{weak} up to a scale Λ, which is taken to be $M_{GUT} \simeq 2 \times 10^{16}$ GeV. The low value of $m_{H_u}^2$(weak) that is required to obtain small $\Delta_{\rm EW}$ can always be realized via RGE running, once the GUT-scale value of $m_{H_u}^2$ is decoupled from matter scalar masses.

To illustrate how a low value of $m_{H_u}^2(m_{SUSY})$ is obtained, shown in Fig. 3 is the running of various SUSY parameters versus the renormalization scale Q for the RNS2 benchmark point from Ref. [47]. The RNS2 point has parameters $m_0 = 7025$ GeV, $m_{1/2} = 568.3$ GeV, $A_0 = -11426.6$ GeV, $\tan\beta = 8.55$ with $\mu = 150$ GeV and $m_A = 1000$ GeV. The gaugino and matter scalar mass parameters evolve from $m_{1/2}$ and m_0 to their weak scale values, resulting in a pattern of masses very similar to that in mSUGRA. The parameter μ hardly evolves, and for such a low value of $\tan\beta$, $m_{H_d}^2$ also suffers little evolution. Of most interest here is the RG evolution of $m_{H_u}^2$. As is well known, the SUSY breaking parameters $m_{Q_3}^2$, $m_{U_3}^2$ and $m_{H_u}^2$ of the scalar fields that couple via the large top quark Yukawa coupling are driven down with reducing values of the scale Q. The reduction is the greatest for $m_{H_u}^2$ which, in fact, is driven negative, triggering the radiative breakdown of electroweak symmetry [26]. It is seen from the figure that the weak scale value of $-m_{H_u}^2$ has a magnitude $\sim m_Z^2$, and is much smaller than the weak scale value of other mass parameters. This is not an accident because the NUHM2 model provides the flexibility to adjust the GUT scale value of $m_{H_u}^2$ so that it barely runs to negative values at the weak scale.

This chapter will explore what parameter choices lead to low values of $\Delta_{\rm EW}$. While Δ_{EW} seems bounded from below by about 100 in mSUGRA/CMSSM [41], one finds that Δ_{EW} as low as ~ 10 can be obtained in NUHM2. The goal is to provide a rather complete characterization of RNS. This should provide a comprehensive picture as to where in model parameter space one can find 1) $m_h \sim 125$ GeV

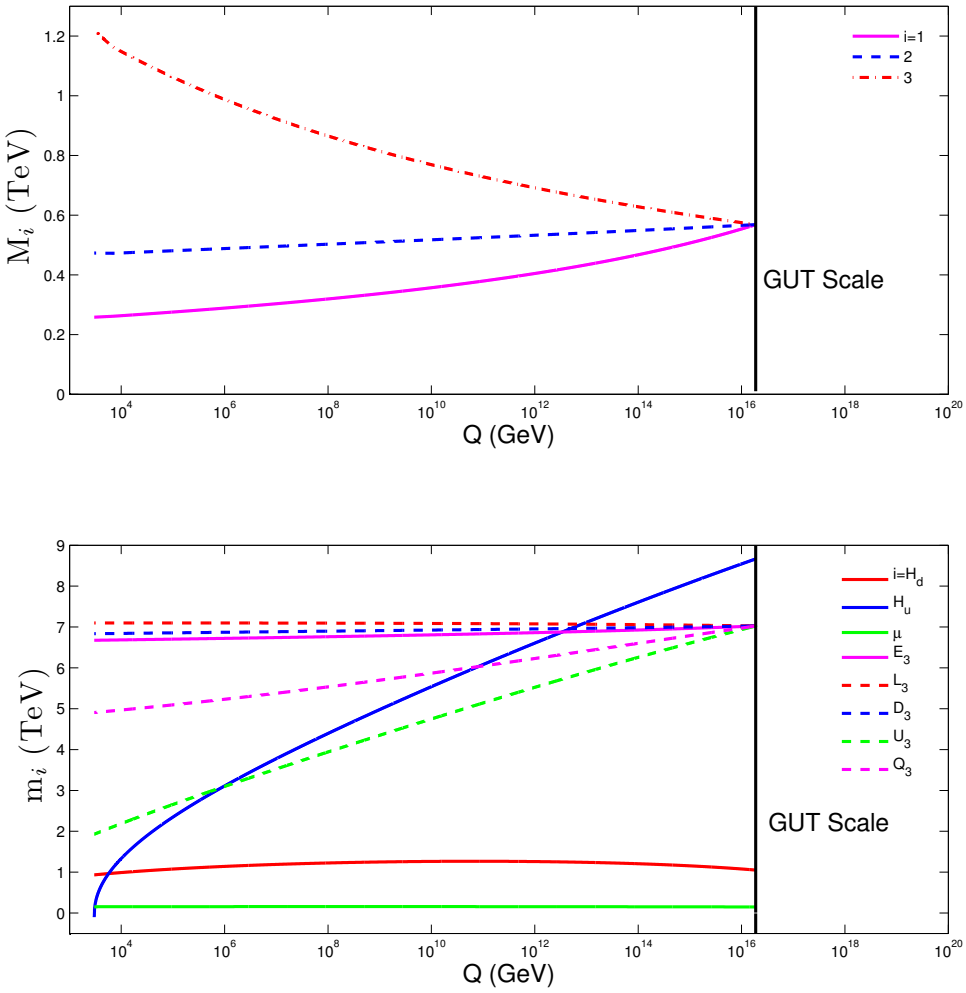


Figure 3: Evolution of SSB parameters from $M_{\rm GUT}$ to M_{weak} for the RNS2 benchmark point taken from in Ref. [47] whose parameters are given in the text. The graph extends to values below $Q^2 = m_{\tilde{t}_1} m_{\tilde{t}_2}$ where the Higgs mass parameters are extracted.

along with 2) low EWFT $\Delta_{\rm EW} \stackrel{<}{\sim} 30$ while at the same time 3) respecting LHC constraints on sparticle masses. In Sec. 3.1.1, parameter space regions leading to low $\Delta_{\rm EW}$ from scans over the NUHM2 model which allow for RNS are shown. In Sec. 3.1.3, the results are extended to include the split generation non-universal Higgs model NUHM3, wherein high scale third generation scalar masses $m_0(3)$ need not equal first/second generation scalar masses $m_0(1,2)$. While the former implementation allows for fewer parameters, the additional freedom in the NUHM3 model allows for a more robust decoupling solution to the SUSY flavor and CP problems because heavier multi-TeV first/second generation sfermion masses are then possible. Section 3.2 shows that constraints from B-physics – especially $BF(b\rightarrow s\gamma)$ are much more easily respected in RNS than in generic natural SUSY models.

Motivated by the possibility of cancellations occurring in $m_{H_u}^2(m_{SUSY})$, the EWSB minimization condition (2.4) is now returned to, and the radiative corrections embodied in Σ_u^u and Σ_d^d that have not yet been discussed will be examined. These affect the minimization condition in an important way when $m_{H_u}^2(m_{\rm SUSY})$ and μ^2 are much smaller than the scale of other weak scale SUSY breaking parameters. At the one-loop level, Σ_u^u contains the contributions [50, 51] $\Sigma_u^u(\tilde{t}_{1,2})$, $\Sigma_u^u(\tilde{b}_{1,2})$, $\Sigma_u^u(\tilde{\tau}_{1,2})$, $\Sigma_u^u(\widetilde{W}_{1,2})$, $\Sigma_u^u(\widetilde{Z}_{1-4})$, $\Sigma_u^u(h,H)$, $\Sigma_u^u(H^{\pm})$, $\Sigma_u^u(W^{\pm})$, $\Sigma_u^u(Z)$, and $\Sigma_u^u(t)$. Σ_d^d contains similar terms along with $\Sigma_d^d(b)$ and $\Sigma_d^d(\tau)$ while $\Sigma_d^d(t) = 0$. There are additional contributions from first/second generation sparticles from their D-term couplings to Higgs scalars. If these squarks, and separately sleptons, are degenerate then these contributions cancel within each generation because the sum of weak isospins/hypercharges of squarks/sleptons total to zero [41]. In the parameter space region where RNS is realized, *i.e.* where $-m_{H_u}^2(m_{SUSY}) \sim \mu^2 \sim m_Z^2$, the radiative correction terms from Σ_u^u may give the largest contributions to $\Delta_{\rm EW}$.

The largest of the Σ_u^u terms almost always come from top squarks for which it can be found

$$\Sigma_u^u(\tilde{t}_{1,2}) \;=\; \frac{3}{16\pi^2}F(m^2_{\tilde{t}_{1,2}}) \times \left[f_t^2 - g_Z^2 \mp \frac{f_t^2 A_t^2 - 8g_Z^2(\frac{1}{4} - \frac{2}{3}x_W)\Delta_t}{m^2_{\tilde{t}_2} - m^2_{\tilde{t}_1}} \right] \qquad (3.1)$$

where $\Delta_t = (m^2_{\tilde{t}_L} - m^2_{\tilde{t}_R})/2 + m_Z^2 \cos 2\beta(\frac{1}{4} - \frac{2}{3}x_W)$, $g_Z^2 = (g^2 + g'^2)/8$, $x_W \equiv \sin^2\theta_W$ and $F(m^2) = m^2\left(\log(m^2/Q^2) - 1\right)$, with $Q^2 = m_{\tilde{t}_1} m_{\tilde{t}_2}$. In Ref. [47], it is shown that for the case of the $\tilde{t}_1$ contribution, as $|A_t|$ gets large there is a suppression of $\Sigma_u^u(\tilde{t}_1)$ due to a cancellation between terms in the square brackets of Eq. (3.1). The $\tilde{t}_2$ contribution is suppressed if there is a sizeable splitting between $m_{\tilde{t}_2}$ and $m_{\tilde{t}_1}$ due to a large cancellation within $F(m^2_{\tilde{t}_2})$ because $\log(m^2_{\tilde{t}_2}/Q^2) = \log(m_{\tilde{t}_2}/m_{\tilde{t}_1}) \simeq 1$. The large $|A_t|$ values suppress both top squark contributions to Σ_u^u, and at the same time lift up the value of m_h, which is near maximal for large negative A_t. Combining all effects, one sees that the same mechanism responsible for boosting the value of m_h into accord with LHC measurements can also suppress the Σ_u^u contributions to EWFT, leading to a model with low EWFT.

To display the quality of EWFT explicitly, Fig. 4*a* shows the various *signed* contributions to $m_Z^2/2$ that enter Eq. (2.4) for the RNS2 point from Fig. 3 and Ref. [47]. In this figure, the signed contributions are labeled by C_i where $i = H_u, H_d, \mu, \Sigma_u^u, \Sigma_d^d$. The largest contributions come from $C_{\Sigma_u^u} \sim 0.04$ TeV^2 and $C_{H_u} \sim -0.03$ TeV^2. Frame *b*) shows these same quantities for the mSUGRA model (where μ and m_A are outputs instead of input parameters). Here, the maximal contributions $C_{H_u} \sim 15$ TeV^2 and $C_\mu \sim -15$ TeV^2. Frame *c*) compares results from the two models using a common scale. Here, it is clearly seen that the mSUGRA model is enormously fine-tuned compared to the RNS2 benchmark point.

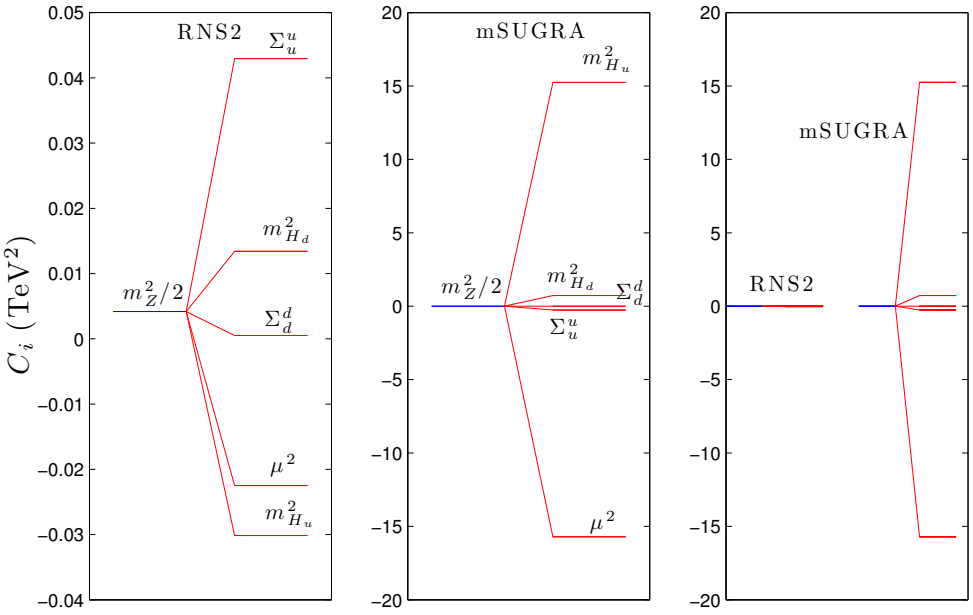


Figure 4: Signed contributions to $m_Z^2/2$ from terms in the EWSB minimization condition Eq. 2.4 from *a*) the RNS2 benchmark point defined in the text and *b*) the corresponding mSUGRA model as RNS2 with μ and m_A as outputs rather than inputs. In frame *c*), the results for both models are plotted on a common scale.

3.1 Radiative natural SUSY from the NUHM models

Since the mass scale of the MSSM is stable to radiative corrections even when the MSSM is embedded into a high scale framework, it is tempting to speculate that the MSSM arises as the low energy limit of an underlying SUSY grand unified theory with a unification scale $M_{\rm GUT} \simeq 2 \times 10^{16}$ GeV. Indeed, the MSSM receives some indirect support from experiment in that 1) the measured weak scale gauge couplings nearly unify at $M_{\rm GUT}$ under MSSM RG evolution, 2) radiative corrections due to the large top quark Yukawa coupling – consistent with $m_t \sim 173$ GeV – dynamically breaks electroweak symmetry, and 3) a light SM-like Higgs boson has been discovered to be lying squarely within the narrow mass window predicted by the MSSM.

Motivated by these successes, the interesting question arises as to whether a natural SUSY sparticle mass spectrum, *i.e.* one with a modest value of $\Delta_{\rm EW}$, can be consistently generated from a model with parameters defined at the high scale $Q = M_{\rm GUT}$.

3.1.1 RNS from the NUHM2 model

Naturalness requires $|\mu| \sim m_Z\sqrt{\Delta_{\rm EW}/2}$, while the recently measured [52] value of the branching fraction $BF(B_s \to \mu^+\mu^-)$ qualitatively agrees with the predicted SM value, which in turn requires the CP odd boson A to be relatively heavy. One is then led to adopt the 2-parameter non-universal Higgs model (NUHM2) [28], wherein weak scale values of μ and m_A may be used as inputs in lieu of GUT scale values of $m_{H_u}^2$ and $m_{H_d}^2$. Also, in this section a common GUT scale mass parameter m_0 is taken for *all* the matter scalars. Thus the parameter set is given by:

$$m_0,\ m_{1/2},\ A_0,\ \tan\beta,\ \mu,\ m_A. \tag{3.2}$$

For these calculations, $m_t = 173.2$ GeV and the Isajet 7.83 [53] SUSY spectrum generator Isasugra [54] are used.

Radiative Natural SUSY solutions are searched for by first performing a random scan over the following NUHM2 parameter ranges:

$$\begin{aligned} m_0 &: 0 - 20 \text{ TeV}, \\ m_{1/2} &: 0.3 - 2 \text{ TeV}, \\ -3 &< A_0/m_0 < 3, \\ \mu &: 0.1 - 1.5 \text{ TeV}, \\ m_A &: 0.15 - 1.5 \text{ TeV}, \\ \tan\beta &: 3 - 60. \end{aligned} \tag{3.3}$$

For the solutions found, it is required that:

- electroweak symmetry be radiatively broken (REWSB),
- the neutralino $\widetilde{Z}_1$ is the lightest MSSM particle,
- the light chargino mass obeys the model independent LEP2 limit, $m_{\widetilde{W}_1} > 103.5$ GeV [25],
- The parameters m_0 and $m_{1/2}$ respect the recent LHC search bounds on $m_{\tilde{g}}$ and $m_{\tilde{q}}$ obtained within the mSUGRA model [1, 2] are respected,
- $m_h = 125 \pm 2$ GeV, allowing for estimated uncertainty in the calculation of m_h.

To begin the investigation of NUHM2 model parameters which lead to low $\Delta_{\rm EW}$, Fig. 5 shows each scan point as a red "+" in frames of $\Delta_{\rm EW}$ versus *a*) m_0, *b*) $m_{1/2}$, *c*) A_0/m_0, *d*) $\tan\beta$, *e*) μ, and *f*) m_A. Since low $\Delta_{\rm EW}$ solutions are only possible for low values of μ, a separate narrow scan was performed, but this time with μ

restricted between 100–300 GeV. The results of this second scan are shown by the blue crosses in the figure.

One sees from the plots that $\Delta_{\rm EW}$ varies from as low as ~ 10 ($\Delta_{EW}^{-1} = 10\%$ EWFT) to over 1000. While the bulk of points shown are fine-tuned with large $\Delta_{\rm EW} \gtrsim 100$, there do exist many solutions with $\Delta_{\rm EW} \lesssim 30$, corresponding to better than 3% EWFT. The RNS solutions with $\Delta_{\rm EW} \lesssim 30$ are obtained for values of $m_0 \sim 1 - 8$ TeV. In the cases where m_0 is as high as 5-10 TeV, the top squark masses are driven to much lower values via 1) the large top-quark Yukawa coupling f_t which suppresses top-squark soft masses during RG evolution, 2) large mixing effects which can suppress $m_{\tilde{t}_1}$ and yield a large $m_{\tilde{t}_1} - m_{\tilde{t}_2}$ splitting, and 3) two-loop RGE suppression of diagonal top squark mass terms arising from large first/second generation sfermion masses [49, 55, 56]. If m_0 is too large – in this case above ~ 10 TeV – then these suppression mechanisms are insufficient to drive $m_{\tilde{t}_{1,2}}$ to low enough values to allow for low EWFT. Thus, the span of points shown in frame *a*) trends upward in $\Delta_{\rm EW}$ as m_0 increases past about 8 TeV. One also sees that for the red pluses in frame *a*) $\Delta_{\rm EW}$ has an upper bound close to about 500 if $m_0 \lesssim 10$ TeV. For still larger values of m_0 then $\Delta_{\rm EW}$ increases with m_0. This is because while μ^2 (or equivalently $-m_{H_u}^2$) is the largest of the quantities in (2.4) for the lower range of m_0, for very large values of m_0 then Σ_u^u begins to dominate. The blue crosses from the narrow scan with small μ have a different shape from the red broad scan since the upper edge is mostly determined by Σ_u^u, and so increases with m_0.

Frame *b*) of Fig. 5 shows $\Delta_{\rm EW}$ *vs.* $m_{1/2}$. Here, the low values of $\Delta_{\rm EW}$ span a wide range of $m_{1/2}$ values from $0.3 - 1.5$ TeV. Since $m_{\tilde{g}} \sim (2.5 - 3)m_{1/2}$, one expects $\Delta_{\rm EW} \lesssim 30$ for $m_{\tilde{g}}$ values up to about 4 TeV. For the entire parameter space (red pluses) $\Delta_{\rm EW}$ is roughly evenly distributed with respect to the gaugino mass parameter. Frame *c*) shows $\Delta_{\rm EW}$ *vs.* A_0/m_0. A clear trend is evident for low values of EWFT when $|A_0/m_0| \sim 1.5 - 2$. The reason is that the hole at low

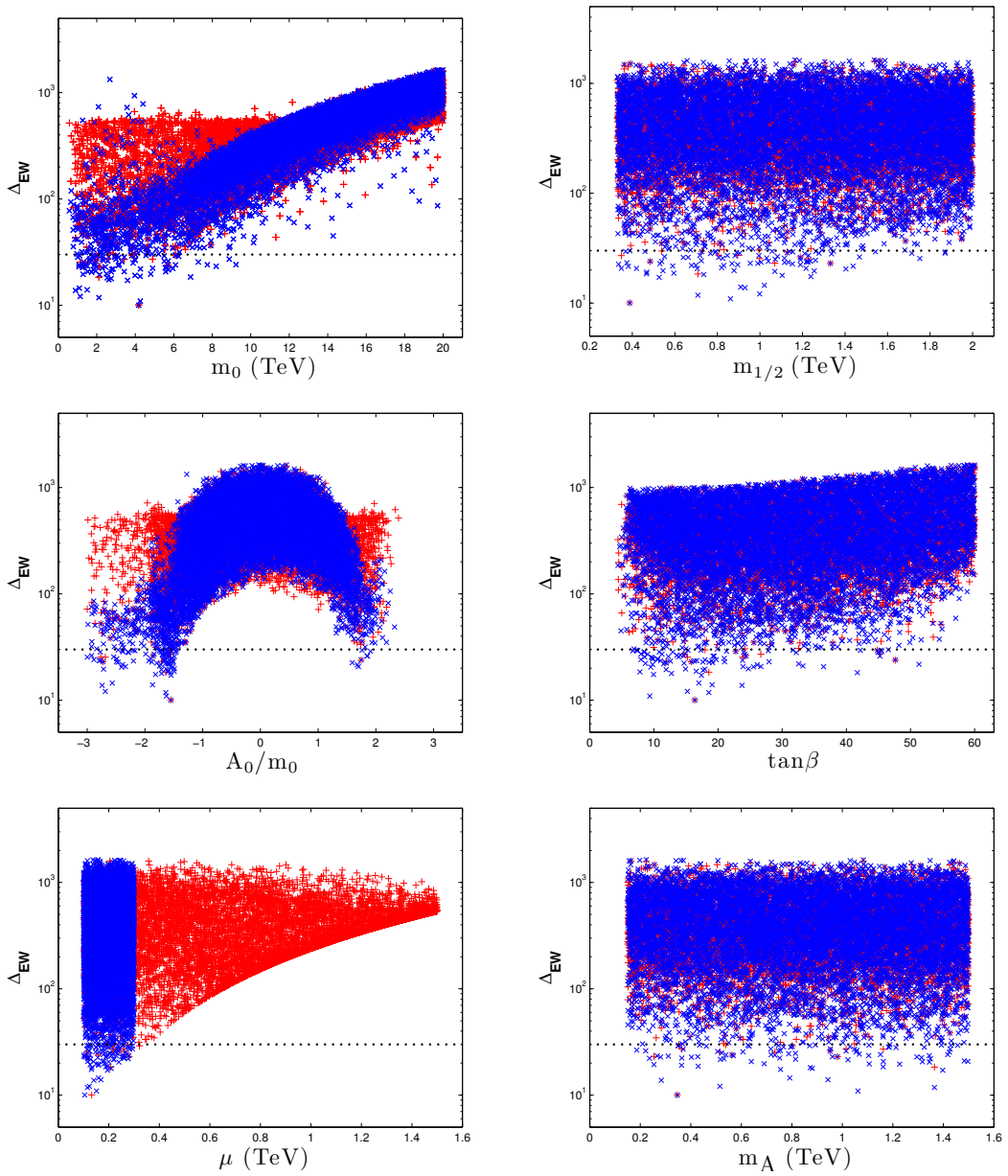


Figure 5: The dependence of $\Delta_{\rm EW}$ on various NUHM2 parameters from a scan (3.3) over parameter space (red pluses) and for the dedicated scan with 100 GeV$<$ μ $<$300 GeV (blue crosses). The line at $\Delta_{\rm EW} = 30$ is to guide the eye.

magnitudes of A_0/m_0 and small values of $\Delta_{\rm EW}$ occurs because of the Higgs mass constraint. Large magnitudes of GUT scale A_0 lead to correspondingly large weak scale A_t parameters, which, in turn, provide large mixing in the top-squark sector. This leads to low EWFT and also heightened values of $m_h \sim 125$ GeV. Frame *d*) shows $\Delta_{\rm EW}$ *vs.* $\tan\beta$. There is a slight preference for low $\tan\beta \sim 10-20$ but otherwise no structure to speak of. Frame *e*) shows $\Delta_{\rm EW}$ versus the weak scale value of μ. The parabolic lower edge of the span of points reflects the upper bound on μ necessary for low EWFT. From the plot, bounds on μ can be conveniently read off: for instance, requiring $\Delta_{\rm EW} \lesssim 30$ then requires $\mu \lesssim 350$ GeV. Models with low $\mu \sim 100$ GeV but multi-TeV top squarks can still be very fine-tuned if the dominant contributions to $\Delta_{\rm EW}$ arise from $\Sigma_u^u(\tilde{t}_i)$. In frame *f*) $\Delta_{\rm EW}$ *vs.* m_A is shown. Low $\Delta_{\rm EW}$ can be found over the entire range of $m_A \sim 0.15-1.5$ TeV, so this parameter is not so relevant towards achieving low EWFT.

Next, to gain a sense of the sparticle mass ranges expected from RNS, $\Delta_{\rm EW}$ is plotted versus selected sparticle masses. First, since $m_0 \sim 2-8$ TeV for $\Delta_{\rm EW} \lesssim 30$, the first and second generation squark and slepton masses are expected to also be within this range (which is for the most part inaccessible LHC SUSY searches). Next, in frame *a*) of Fig. 6, $\Delta_{\rm EW}$ *vs.* $m_{\tilde{g}}$ is shown. Requiring $\Delta_{\rm EW} \lesssim 30$ requires $m_{\tilde{g}} \sim 1-4$ TeV. The lower portion of this range should be accessible to LHC14 searches, while the upper part lies beyond any LHC luminosity upgrade [57].

Frame *b*) shows $\Delta_{\rm EW}$ versus the lighter top squark mass $m_{\tilde{t}_1}$. Here, $\Delta_{\rm EW} \lesssim 30$ allows $m_{\tilde{t}_1} \sim 0.5-2.5$ TeV range. This is well above the range expected in generic NS models [16, 17, 18], where $m_{\tilde{t}_{1,2}}$ has been advocated to lie below about 600 GeV. Frame *c*) shows $\Delta_{\rm EW}$ *vs.* $m_{\tilde{t}_2}$. Here, $m_{\tilde{t}_2}$ can range up to ~ 6 TeV for $\Delta_{\rm EW} \lesssim 30$. Such high values of $m_{\tilde{t}_2}$ are helpful to increase radiative corrections to the light Higgs mass m_h into the 125 GeV range. However, such heavy top squarks lie far beyond any conceivable LHC reach. In frame *d*), $\Delta_{\rm EW}$ *vs.* $m_{\tilde{b}_1}$ is shown. Here,

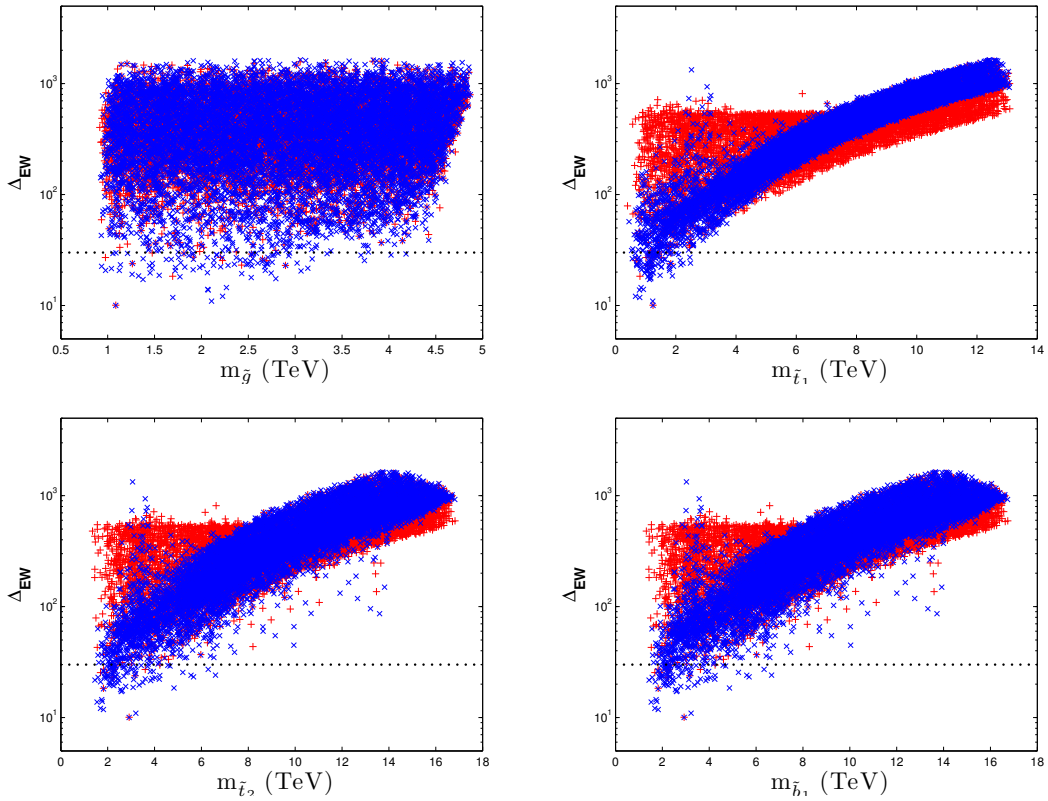


Figure 6: The value of $\Delta_{\rm EW}$ versus gluino and third generation squark masses from a scan over NUHM2 parameter space. As in Fig. 5, the red pluses denote the distributions from the complete scan, whereas the blue crosses depict the results for the dedicated low μ scan. The line at $\Delta_{\rm EW} = 30$ is to guide the eye.

$m_{\tilde{b}_1} \sim 0.8-6$ TeV, which again allows for far heavier bottom squarks than previous NS models, where $m_{\tilde{t}_{1,2}}$ and $m_{\tilde{b}_1}$ all were suggested to be $\lesssim 600$ GeV.

Figure 7*a*) shows $\Delta_{\rm EW}$ *vs.* $m_{\widetilde{W}_1}$. For RNS models, $m_{\widetilde{W}_1} \simeq m_{\widetilde{Z}_{1,2}} \sim |\mu|$, *i.e.* its mass is roughly equal to that of the two lighter neutralinos. Since $\widetilde{W}_1$ is mainly higgsino-like near the lower edge of the envelope of points, the distribution follows a similar pattern as for the $\Delta_{\rm EW}$ *vs.* μ plot in Fig. 5. For $\Delta_{\rm EW} \lesssim 20$, $m_{\widetilde{W}_1} \lesssim 250$ GeV; thus, a linear collider operating with $\sqrt{s} > 2m_{\widetilde{W}_1}$ will directly probe the lowest values of $\Delta_{\rm EW}$ if the relatively soft visible daughters of the chargino can be distinguished over two-photon backgrounds [58]. In this sense, it has been emphasized that for models of natural SUSY, a linear e^+e^- collider would be a higgsino factory in addition to a Higgs factory [19, 47, 59]. This will be discussed in Chapter 5. In frame *b*), $\Delta_{\rm EW}$ *vs.* $m_{\widetilde{W}_2}$ is shown. In the RNS model, the $\widetilde{W}_2$ is nearly pure wino-like and its mass can range between $\sim 0.3-1.2$ TeV for $\Delta_{\rm EW} \lesssim 30$. Since RNS as presented here includes gaugino mass unification, then typically $\widetilde{Z}_{1,2}$ are higgsino-like, $\widetilde{Z}_3$ is bino-like and $\widetilde{Z}_4$ is wino-like. Since the $SU(2)$ gauge coupling g is rather large, one expects significant rates for $\widetilde{W}_2^{\pm}\widetilde{Z}_4$ production at LHC, at least for the lower portion of the range of $m_{\widetilde{W}_2}$. Frame *c*) shows the $m_{\tilde{Z}_2} - m_{\tilde{Z}_1}$ mass difference in RNS versus $\Delta_{\rm EW}$. For most points with $\Delta_{\rm EW} \lesssim 30$, it is seen that $m_{\tilde{Z}_2} - m_{\tilde{Z}_1} \lesssim 10-20$ GeV. Some points with $\Delta_{\rm EW} \sim 30-40$ have a mass difference as large as 100 GeV; these points arise from sampling the lower portion of the $m_{1/2}$ range, which gives rise to gaugino masses comparable in magnitude to $|\mu|$ so that the lighter electroweakinos are actually gaugino-higgsino mixtures. For the small mass gap case, the lighter neutralinos are dominantly higgsino-like and decay via $\widetilde{Z}_2 \to \widetilde{Z}_1 f\bar{f}$ (here f denotes SM-fermions) through the virtual Z. Then decays into opposite-sign same-flavor (OS/SF) isolated dileptons should occur at $\sim 3\%$ for each charged lepton species. The presence of low invariant mass OS/SF isolated dileptons from boosted $\widetilde{Z}_2$ produced in gluino or gaugino cascade decay events could then be

a distinctive signature of RNS at the LHC as will be discussed in Chapter 4. For NUHM2 models with larger values of $\Delta_{\rm EW}$, falling outside the RNS low EWFT requirement, $m_{\widetilde{Z}_2}$ can be greater than $m_{\widetilde{Z}_1}+m_Z$ or $m_{\widetilde{Z}_1}+m_h$ so that two body decays of $\widetilde{Z}_2$ are then allowed. Finally, in frame *d*), $\Delta_{\rm EW}$ *vs.* m_h is shown. Here, the lower $m_h\sim 123-124$ GeV values are just slightly preferred by EWFT over the higher range, although values of m_h as high as ~ 126.5 GeV occur for $\Delta_{\rm EW}=30$.

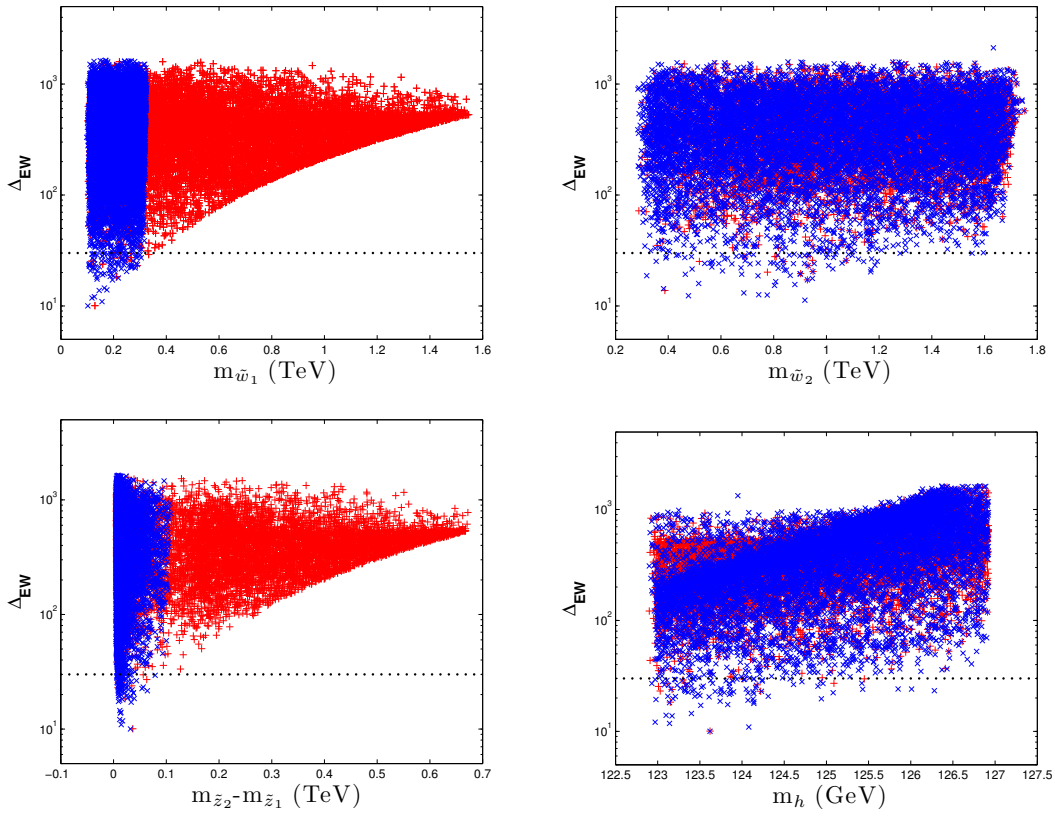


Figure 7: The value of $\Delta_{\rm EW}$ versus electroweak -ino and Higgs boson masses from a scan over NUHM2 parameter space. As in Fig. 5, the red pluses denote the distributions from the complete scan, whereas the blue crosses depict the results for the dedicated low μ scan. The line at $\Delta_{\rm EW}=30$ is to guide the eye.

Finally, in Fig. 8 a scatter plot of $\Delta_{\rm EW}$ versus the GUT scale ratio $m_{H_u}^2/m_0$ from the scan over NUHM2 models is shown. Here is is seen that for points with $\Delta_{\rm EW}\lesssim 30$, then $m_{H_u}(M_{\rm GUT})\sim(1-2)m_0$.

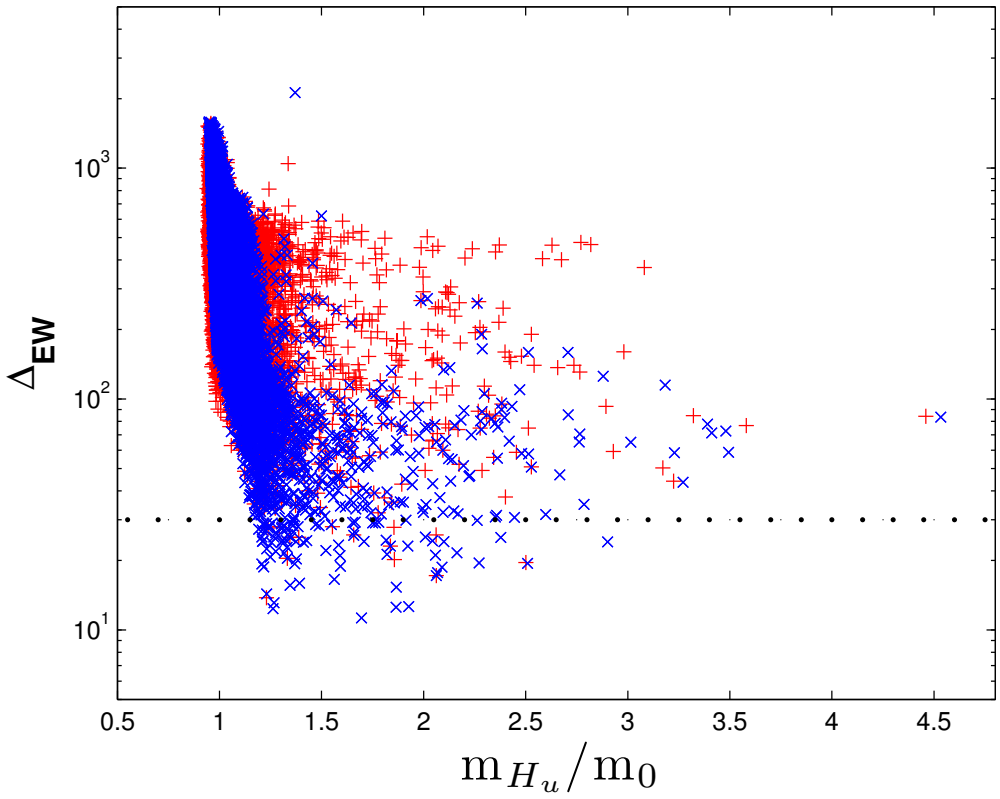


Figure 8: The value of $\Delta_{\rm EW}$ versus $m_{H_u}/m_0(M_{\rm GUT})$ from the scan over the NUHM2 parameter space. As before, the red pluses are for the scan over the entire range of μ while the blue crosses are for the dedicated scan with μ limited to the 100-300 GeV range. The line at $\Delta_{\rm EW} = 30$ is to guide the eye.

3.1.2 RNS from the NUHM1 model

The NUHM1 model [27] is inspired by $SO(10)$ SUSY GUT models where the Higgs doublets live in the 10-dimensional fundamental representation while the matter scalars inhabit the 16- dimensional spinor representation. In this case, the parameter set is expanded by one and now the scan is over

- $m_0 : 0 - 15$ TeV,
- $m_{H_u} = m_{H_d} \equiv m_H : 0 - 15$ TeV,
- $m_{1/2} : 0 - 2$ TeV,
- $2.5 < A_0/m_0 < 2.5$,
- $\tan\beta : 3 - 60$.

By increasing $m_H \gg m_0$, then $m_{H_u}^2$ is only driven to small instead of large negative values, while if $m_{H_u}^2$ is increased too much, then $m_{H_u}^2$ is never driven negative and electroweak symmetry is not broken. If m_H is taken smaller than m_0, even with $m_H^2 < 0$ as a possibility, then $m_{H_d} \sim m_A$ can be decreased while $m_{H_u}^2$ is driven to very large negative values. In the former case, where $m_{H_u}^2$ is driven to small negative values, then μ also decreases since its value is set to yield the measured Z mass. In such cases, one expects reduced values of $\Delta_{\rm EW}$. In the scan results shown in Fig. 9, this is true, as the minimal value of $\Delta_{\rm EW}$ reaches as low as ~ 30. Values of $\Delta_{\rm EW}$ in the $30 - 50$ range which obey B-decay constraints and $m_h \sim$125 GeV can be found for $m_0 \sim 3 - 10$ TeV. With such large m_0 values, then the top squarks also tend to be in the $3 - 10$ TeV regime and the top squark radiative corrections prevent $\Delta_{\rm EW}$ from reaching below ~ 30.

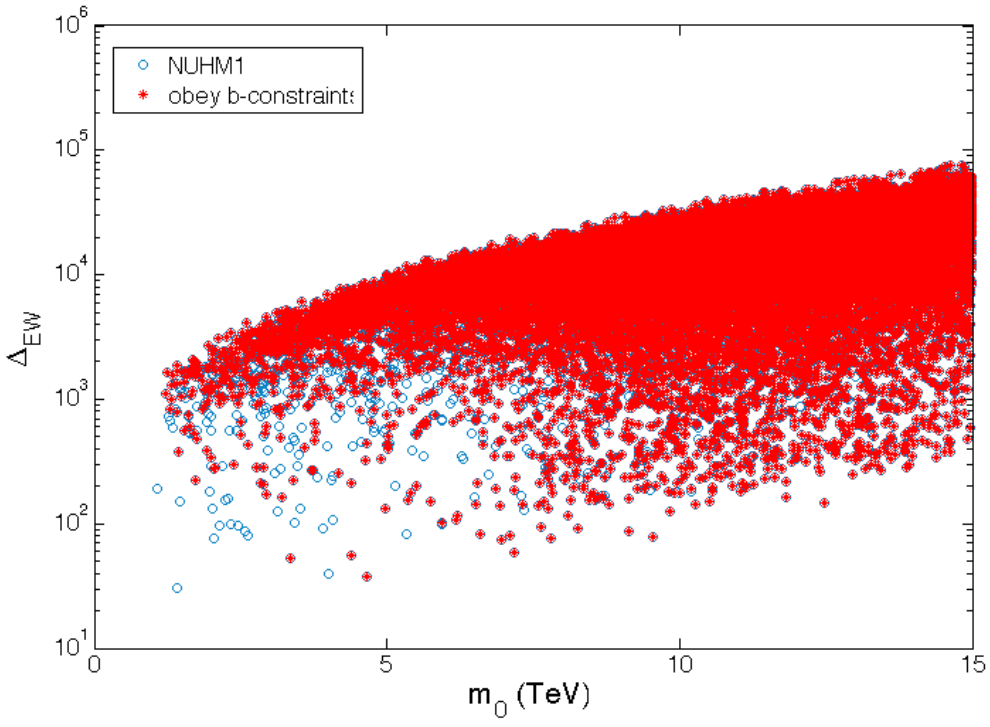


Figure 9: Plot of $\Delta_{\rm EW}$ vs. m_0 from a scan over NUHM1 parameter space while maintaining $m_h = 125.5 \pm 2.5$ GeV.

3.1.3 RNS from the NUHM3 (split generation) model

This section explores the possibility of split first/second versus third generation matter scalars to see if any advantage can be gained for RNS. Here, the third generation GUT scale mass parameter $m_0(3)$ is allowed to differ from $m_0(1,2)$ for the first/second generation scalars. Universality within each generation is well-motivated by $SO(10)$ GUT symmetry, since all matter multiplets of a single generation belong to a 16-dimensional spinor rep of $SO(10)$. One can also envisage some degree of non-universality between $m_0(1)$ and $m_0(2)$ as long as both lie in the tens of TeV regime: such a scenario invokes a partial decoupling-partial degeneracy solution to the SUSY flavor and CP problems (for constraints from FCNC processes [60], see *e.g.* Ref. [61]). For convenience, $m_0(1)$ and $m_0(2)$ will be set equal, and the parameter set

$$m_0(1,2),\ m_0(3),\ m_{1/2},\ A_0,\ \tan\beta,\ \mu,\ m_A \qquad \text{(NUHM3)} \tag{3.4}$$

will be adopted. Here, $m_0(3)$ is the GUT scale third generation soft SUSY breaking mass parameter and $m_0(1,2)$ is the corresponding (common) parameter for the first/second generation.

RNS solutions from the split generation parameter space are searched for by

implementing a random scan over the parameters:

$$\begin{aligned} m_0(3) &: 0-20 \text{ TeV}, \\ m_0(1,2) &: m_0(3)-30 \text{ TeV}, \\ m_{1/2} &: 0.3-2 \text{ TeV}, \\ -3 &< A_0/m_0 < 3, \\ \mu &: 0.1-1.5 \text{ TeV}, \\ m_A &: 0.15-1.5 \text{ TeV}, \\ \tan\beta &: 3-60. \end{aligned} \tag{3.5}$$

The same LHC sparticle mass and $m_h = 125 \pm 2$ GeV constraints are implemented as before.

Figure 10 shows $\Delta_{\rm EW}$ versus $m_0(3)$ and also versus $m_0(1,2)$. The results for $\Delta_{\rm EW}$ versus other parameters are very similar to Fig. 5 and are not repeated here. From Fig. 10*a*), one sees that RNS solutions with $\Delta_{\rm EW} \lesssim 30$ can be found for $m_0(3)$ values ranging between 1-8 TeV, similar to results found in Fig. 5 for the NUHM2 model. It is interesting to note that the smallest values of $\Delta_{\rm EW}$ in the figure are no smaller than for the NUHM2 model. The gap at small values of $m_0(3)$ is an artifact of the upper limit on $m_{1/2}$ in the scan: for small values of $m_0(3)$ the lighter t-squark is often driven to tachyonic masses by two-loop contributions of heavy first/second generation squarks. With larger values of $m_{1/2}$ in the scan, solutions fill in the entire gap. Even though the GUT scale value of $m_0(3)$ is in the multi-TeV regime, the $\tilde{t}_2$ and especially $\tilde{t}_1$ physical masses are considerably lower – in the few TeV regime – due to radiative effects from RGE running and also large mixing.

The key advantage of the NUHM3 model is seen in Fig. 10*b*), where $\Delta_{\rm EW}$ versus $m_0(1,2)$ is plotted. In this case, the GUT scale first/second generation scalar masses can easily range between $1-30$ TeV while still maintaining low $\Delta_{\rm EW}$. The

solutions with $m_0(1,2)$ in the multi-TeV region will also produce first/second generation squark and slepton masses which are comparable to $m_0(1,2)$. This allows for a much more robust solution to the SUSY flavor/CP problems.

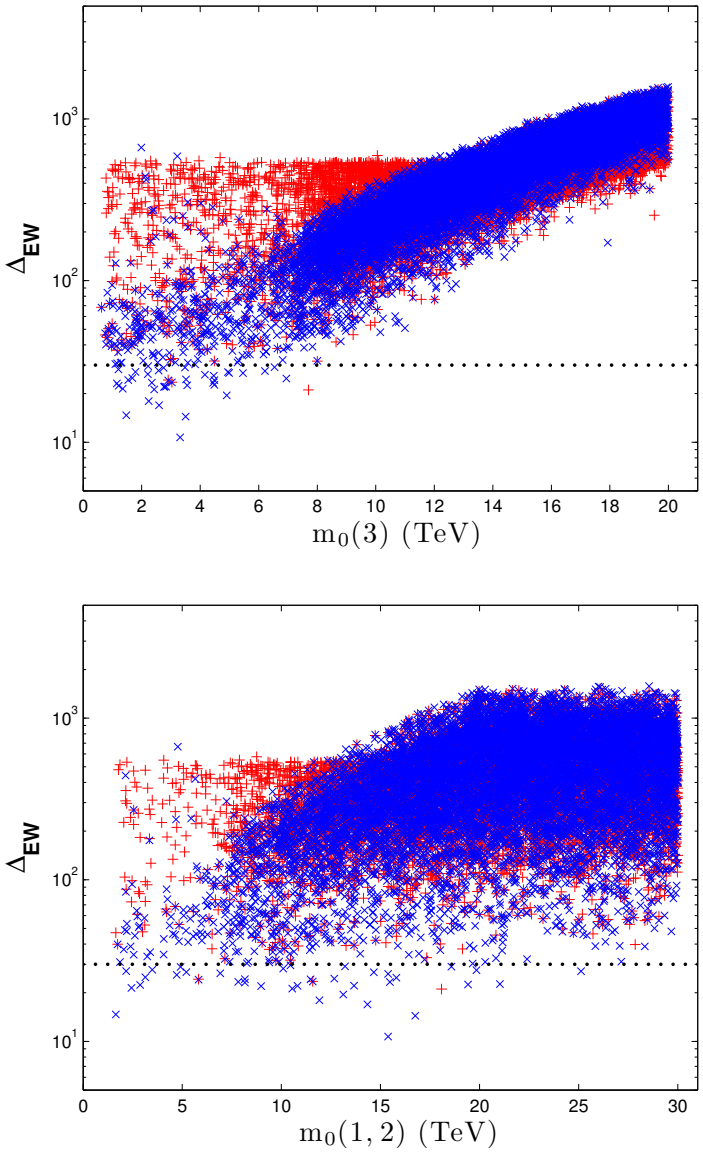


Figure 10: The value of $\Delta_{\rm EW}$ versus $m_0(3)$ and $m_0(1,2)$ from a scan over NUHM3 model with split first/second and third generations. As in Fig. 5, the red pluses denote the distributions from the complete scan, whereas the blue crosses depict the results for the dedicated low μ scan. The line at $\Delta_{\rm EW}=30$ is to guide the eye.

Plots of $\Delta_{\rm EW}$ versus sparticle masses are not shown since these are very similar

to results shown in Fig. 6 and Fig. 7 except for the fact that NUHM3 scans allow for much heavier first/second generation squark and slepton masses in the 10-30 TeV range, whereas in the NUHM2 model the squarks and sleptons are typically constrained to be below 8 TeV due to the imposed relation $m_0(3) = m_0(1,2)$.

3.2 Rare B decay constraints on RNS

3.3 BF($b \to s\gamma$)

The combination of several measurements of the $b \to s\gamma$ decay rate finds that $BF(b \to s\gamma) = (3.55 \pm 0.26) \times 10^{-4}$ [62]. This is slightly higher than the SM prediction [63] of $BF^{SM}(b \to s\gamma) = (3.15 \pm 0.23) \times 10^{-4}$. SUSY contributions to the $b \to s\gamma$ decay rate come mainly from chargino-stop loops and the W-charged Higgs loops, and so are large when these particles are light and when $\tan\beta$ is large [64]. Thus, in generic natural SUSY where $m_{\tilde{t}_{1,2},\tilde{b}_1} \lesssim 600$ GeV, one finds generally large deviations from the SM value for $BF(b \to s\gamma)$, as shown in Ref. [19]. In contrast, in radiative natural SUSY where third generation squarks are in the TeV range, SUSY contributions to $BF(b \to s\gamma)$ are more suppressed. The situation is shown in Fig. 11a) along with the measured central value (green solid line) and errors. The red points all have $\Delta_{\rm EW} < 30$ and qualify as RNS points. The bulk of RNS points are consistent with the measured $BF(b \to s\gamma)$, although there are outliers.

3.4 $B_s \to \mu^+\mu^-$

Recently, the LHCb collaboration has discovered an excess over the background for the decay $B_s \to \mu^+\mu^-$ [52]. They find a branching fraction of $BF(B_s \to \mu^+\mu^-) = 3.2^{+1.5}_{-1.2} \times 10^{-9}$ in accord with the SM prediction of $(3.2 \pm 0.2) \times 10^{-9}$ [65]. In supersymmetric models, this flavor-changing decay occurs through pseudoscalar Higgs A exchange [66], and the contribution to the branching fraction from SUSY is proportional to $\frac{(\tan\beta)^6}{m_A^4}$. The value of $BF(B_s \to \mu^+\mu^-)$ from RNS is shown in Fig. 11b).

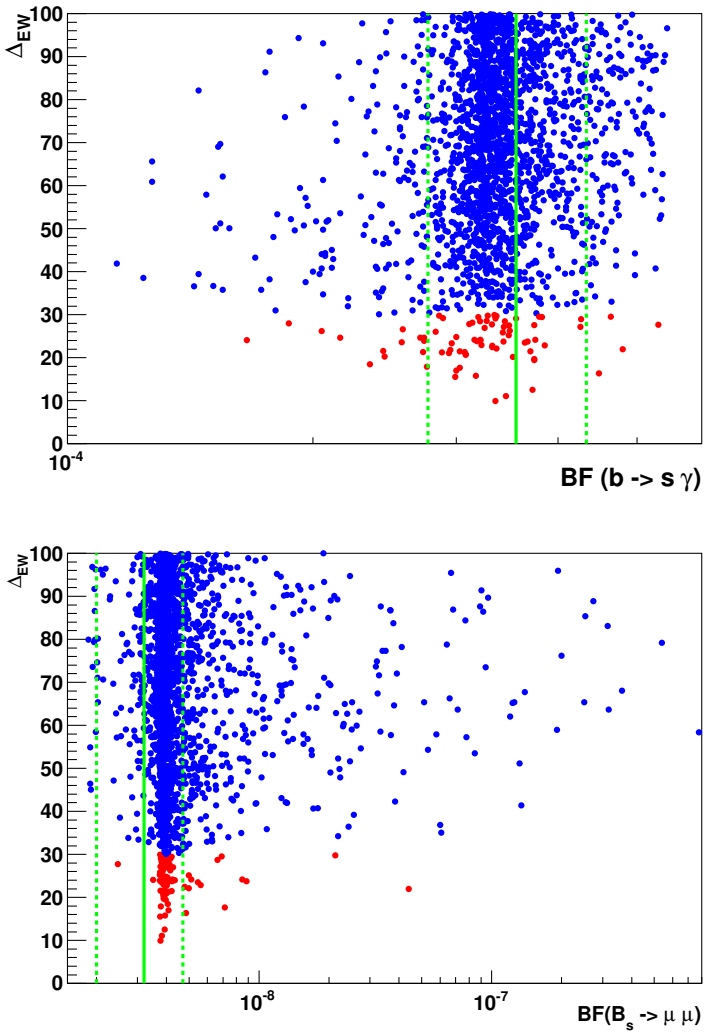


Figure 11: The values of $\Delta_{\rm EW}$ versus *a)* $BF(b \to s\gamma)$ and *b)* $BF(B_s \to \mu^+\mu^-)$. The vertical lines represent the experimental measurements with uncertainties.

The decay is most constraining at large $\tan\beta \sim 50$ as occurs in Yukawa-unified models [67] and low m_A. In the case of RNS with lower $\tan\beta$ and heavier m_A, the constraint is less important. The bulk of the RNS points in Fig. 11*b*) fall well within the newly measured error bands although there are some outlier red points, mainly at larger values of the branching fraction.

3.5 $(g-2)_\mu$

In addition, the well-known $(g-2)_\mu$ anomaly has been reported as a roughly 3σ deviation from the SM value: $\Delta a_\mu = (28.7 \pm 8.0) \times 10^{-10}$ [68]. In RNS, since the $\tilde{\mu}_{1,2}$ and $\tilde{\nu}_\mu$ masses are expected to be in the multi-TeV range, only a tiny non-standard contribution to the $(g-2)_\mu$ anomaly is expected, and alternative explanations for this anomaly would have to be sought.

4 Radiative Natural Supersymmetry at the LHC [37, 69]

In this chapter, the prospects for CERN LHC operating at $\sqrt{s} = 14$ TeV and $30 - 300$ fb^{-1} (or even higher) to discover supersymmetry within the RNS context are assessed, along with a detailed treatment of a variety of different signatures expected at LHC14 for the RNS model. In Sec. 4.2, a RNS model line which contains all the generic features of RNS models is constructed, but with a variable gluino mass. In Sec. 4.3, one may find sparticle production cross sections and branching fractions along the RNS model line. Section 4.5 examines prospects for discovering gluino pair production via signals from their cascade decays. If a signal is found, then the shape of the mass distribution of opposite sign, same flavor dileptons from $\widetilde{Z}_2 \to \widetilde{Z}_1 \ell\bar{\ell}$ decays of neutralinos produced via cascade decays (or directly, see Sec. 4.9), characterizes models with light higgsinos, as emphasized in Ref. [15,70,71]. In Sec. 4.6, aspects of the characteristic same-sign diboson signature from SUSY models with light higgsinos are examined. Sec. 4.7, presents the prospects for LHC to detect the clean trilepton signal arising from wino pair production followed by decay to $WZ + E_T^{\rm miss}$. Section 4.8 examines a novel $4\ell + E_T^{\rm miss}$ signal from wino pair production. Section 4.9 examines the possibility of detecting directly produced higgsinos – whose decays have a very low energy release in the RNS framework – in the soft trilepton channel with low jet activity.

4.1 Simulation of Collider Events

The simulation of collider scattering events through computer packages is generally broken into several steps. The first step is to calculate the hard scattering cross sections within the framework of the parton model. The partons are the pointlike constituents of the particles that are being collided, such as the quarks and gluons in protons. For example, if a is a parton in hadron A, and the fraction of longitudinal momentum it carries is x_a, then the parton distribution function (PDF) may be

denoted by $f_{a/A}(x_a)$. Then, for a hadronic collision between two particles A and B

$$A \;+\; B \;\rightarrow\; c \;+\; X \tag{4.1}$$

where c is the produced quark or lepton and X is anything, the hard scattering "subprocess" is actually

$$a \;+\; b \;\rightarrow\; c. \tag{4.2}$$

The cross section for this subprocess reaction may be calculated from the Lagrangian. However, it is then necessary to convolute the subprocess cross section $d\hat{\sigma}$ with the PDFs, and sum over all partons to obtain the final cross section for the process.[1] For Eq. 4.1 this becomes:

$$d\sigma(AB \rightarrow cX) = \sum_{a,b} \int_0^1 dx_a \int_0^1 dx_b f_{a/A}(x_a) f_{b/B}(x_b) d\hat{\sigma}(ab \rightarrow c). \tag{4.3}$$

Next, parton showers must be included for both initial and final state colored particles. These can be the result of QCD radiation effects and are difficult to calculate exactly. Instead, they are usually incorporated approximately via clever algorithms. Multiple quark and gluon bremstrahlung can lead to effects such as jet broadening. In addition, the products of the hard scattering subprocess may also decay. These *cascade decays* can be very complex, and it is possible to produce a variety of final states which depend on the various branching fractions of the decay chain.

Once the cascade decays have been performed and the parton showers have commenced, the quarks and gluons will begin to hadronize due to the strong force. Hadronization models descride how mesons and baryons may be formed from these

[1] In Chapter 5 where production at an e^+e^- collider is discussed, electron PDFs are used to incorporate beamstrahlung and bremstrahlung effects. However, these have sharp peaks at the electron (or photon) pole, but may result in energy loss of the beam. It is also necessary to take into account polarized beams, which is one of the advantages of e^+e^- over hadron colliders.

particles. The hadronized products can decay into quasi-stable particles such as π and K mesons, which are often detected. Finally, all other remnants of the beams must be taken into account to achieve a complete picture of the physics. These can be described as non-perturbative processes, and lead to hadronic showers in the forward beam direction.

Simulations here are performed mainly with Isajet 7.83 [53]. However, some processes are calculated using other software packages as noted in the text.

4.2 A radiative natural SUSY model line

NUHM2 model parameter values leading to low $\Delta_{\rm EW} \sim 10$ (RNS solutions) were found in the previous chapter. Here, those results are used to construct a RNS model line which features a variable gluino mass, via

$$\begin{aligned} m_0 &= 5 \text{ TeV}, \\ m_{1/2} &: \text{ variable between } 0.3 - 2 \text{ TeV}, \\ A_0 &= -1.6 m_0, \\ \tan\beta &= 15, \\ \mu &= 150 \text{ GeV}, \\ m_A &= 1 \text{ TeV}. \end{aligned} \tag{4.4}$$

The variation in $m_{1/2}$ corresponds to variation in $m_{\tilde{g}}$ from about 0.9 TeV to ~ 5 TeV.

Shown in Fig. 12 is the value of $\Delta_{\rm EW}$ along the RNS model line. One finds that $\Delta_{\rm EW}$ begins around 11 at $m_{1/2} \sim 300$ GeV and increases only mildly with $m_{1/2}$, reaching $\Delta_{\rm EW} \sim 20$ for $m_{1/2}$ as high as 1000 GeV. This corresponds to EWFT of $\sim 9\%$ at the low end of $m_{1/2}$ and $\sim 5\%$ at around $m_{1/2} \sim 1$ TeV where $m_{\tilde{g}} \sim 2.5$ TeV.

In Fig. 13, the various sparticle masses from the RNS model line versus $m_{1/2}$ are plotted. Along the model line, the value of m_h varies from $124.4 - 125.2$ GeV,

quite compatible with the recent ATLAS/CMS Higgs resonance discovery [22, 23]. Also, since μ is fixed at 150 GeV, one obtains a spectrum of higgsino-like $\widetilde{W}_1^{\pm}$, $\widetilde{Z}_1$ and $\widetilde{Z}_2$ states with mass ~ 150 GeV. However, along the model line, the mass gap $m_{\widetilde{Z}_2} - m_{\widetilde{Z}_1}$ varies from 55.6 GeV for very low $m_{1/2}$ to just under ~ 10 GeV if $m_{1/2}$ nears the values allowed by $\Delta_{\rm EW} \lesssim 30$, as shown in Fig. 14. The behaviour of light chargino/neutralino masses is understood since for low $m_{1/2}$ the weak scale gaugino mass $M_1 \simeq 136$ GeV and so the $\widetilde{Z}_1$ state is really a bino-higgsino admixture, while at $m_{1/2} \sim 1$ TeV then $M_1 \simeq 444$ GeV so that $\widetilde{Z}_1$ is more nearly a pure higgsino state.

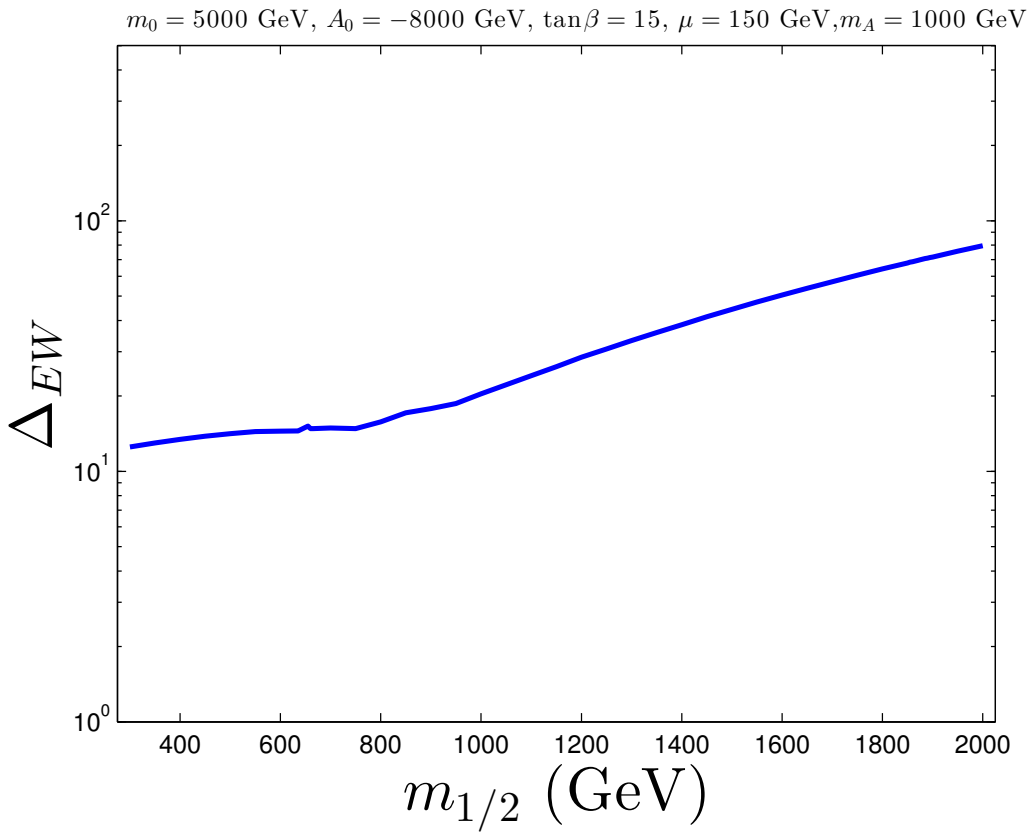


Figure 12: Plot of $\Delta_{\rm EW}$ versus $m_{1/2}$ along the RNS model line.

After the higgsinos, the next lightest sparticles are the bino-like $\widetilde{Z}_3$ – whose mass varies between $160 - 900$ GeV – and the wino-like $\widetilde{W}_2^{\pm}$ and $\widetilde{Z}_4$ states – whose masses

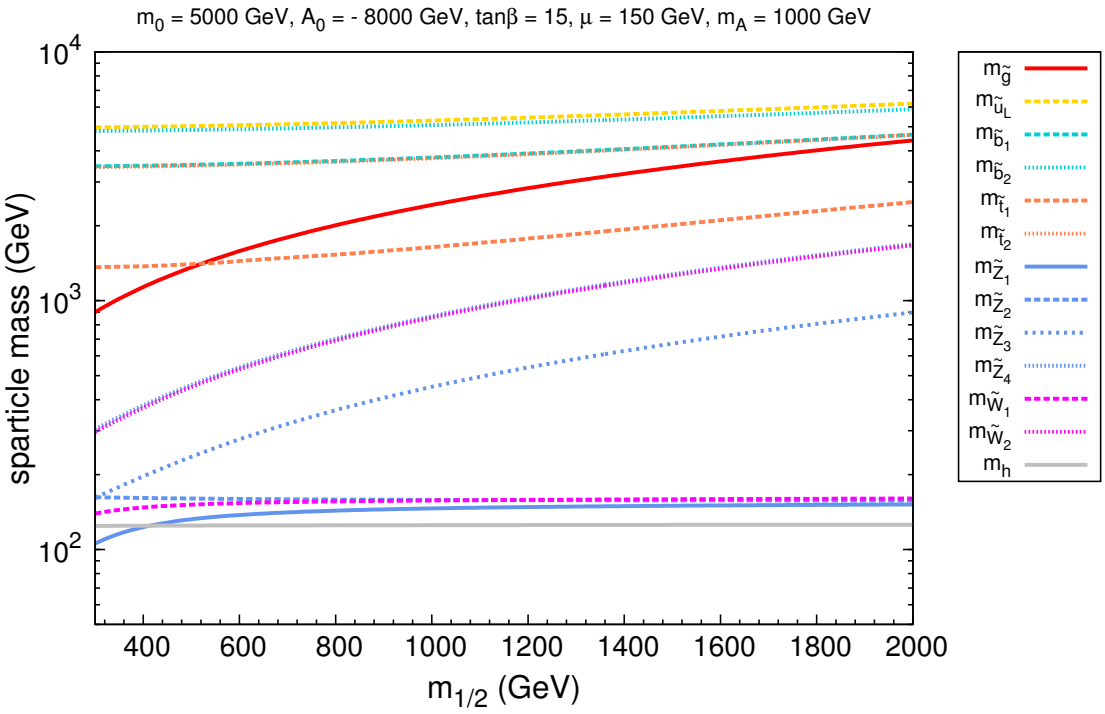


Figure 13: Various sparticle masses versus $m_{1/2}$ for the RNS model line.

vary between $300-1700$ GeV – for the range of $m_{1/2}$ shown in the figure. The solid red curve denoting $m_{\tilde{g}}$ varies between $900-4500$ GeV. The red-dashed $m_{\tilde{t}_1}$ contour varies between $1360-2500$ GeV over the $m_{1/2}$ range shown in the figure; the line crosses the $m_{\tilde{g}}$ curve at $m_{1/2}\sim 520$ GeV. The first/second generation squarks and sleptons inhabit the multi-TeV range, and are far beyond the reach of LHC14.

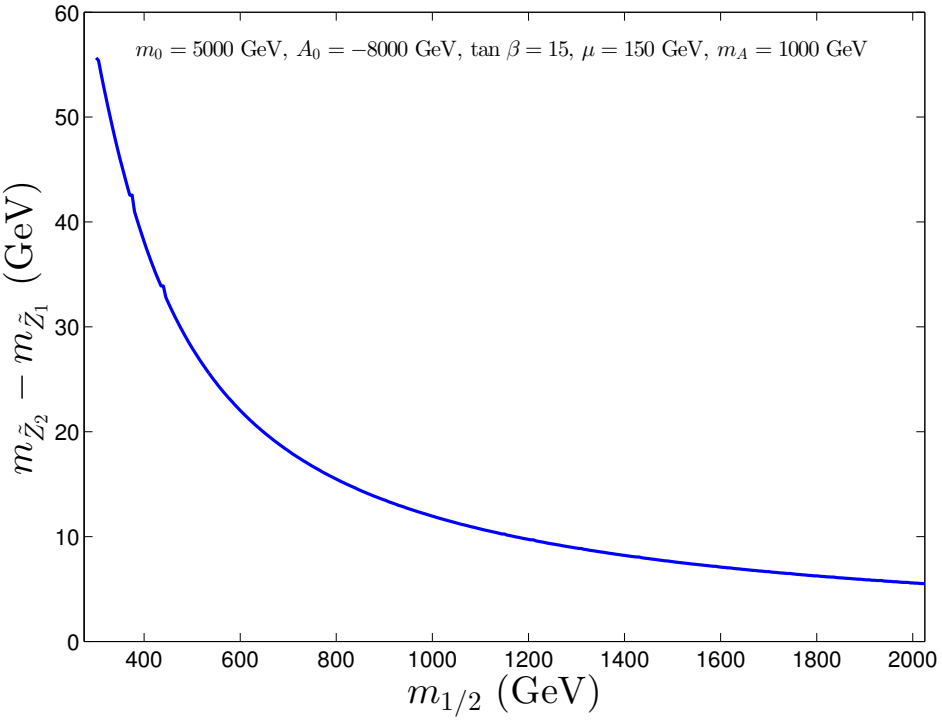


Figure 14: The $m_{\widetilde{Z}_2}-m_{\widetilde{Z}_1}$ mass gap versus $m_{1/2}$ along the RNS model line.

4.3 Sparticle production at LHC

In Fig. 15, various sparticle pair production cross sections at LHC for *a)* $\sqrt{s}=8$ TeV and *b)* $\sqrt{s}=14$ TeV versus $m_{1/2}$ along the RNS model line are shown. Prospino [72] is used to generate the cross sections at NLO in QCD.

Figure 15 shows that the four higgsino pair production reactions – $pp\to\widetilde{W}_1^{\pm}\widetilde{Z}_1$, $\widetilde{W}_1^{\pm}\widetilde{Z}_2$, $\widetilde{W}_1^{+}\widetilde{W}_1^{-}$ and $\widetilde{Z}_1\widetilde{Z}_2$ – all occur at comparable rates of $\sim 10^3$ fb at LHC8 and

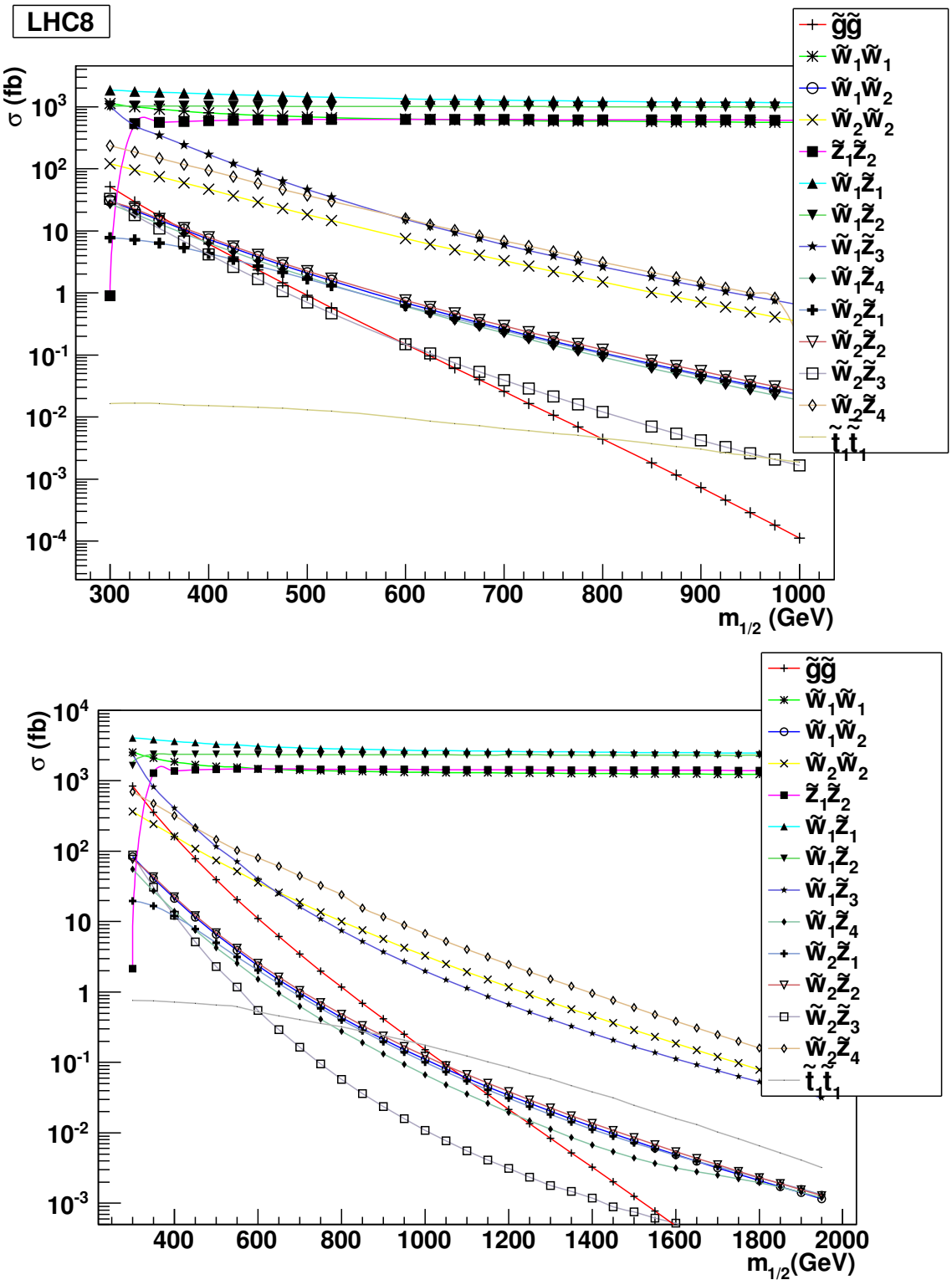


Figure 15: Plot of various NLO sparticle pair production cross sections versus $m_{1/2}$ along the RNS model line for pp collisions at $a)$ $\sqrt{s} = 8$ TeV and $b)$ $\sqrt{s} = 14$ TeV.

of $\sim (2-4)\times 10^3$ fb at LHC14. These cross sections are nearly flat with increasing $m_{1/2}$ since they mainly depend on μ which is fixed at 150 GeV along the model line.

The gluino pair production cross section – $\sigma(pp\to \tilde{g}\tilde{g}X)$ – is denoted by the red curve with pluses (note that $m_{\tilde{g}}\simeq 2.5m_{1/2}$). While the $\tilde{g}\tilde{g}$ production cross section is large at $m_{1/2}\sim 300$ GeV (corresponding to $m_{\tilde{g}}\sim 900$ GeV), it drops off rapidly with increasing values of $m_{1/2}$: it is likely to be inconsequential for even LHC14 searches for the upper range of $m_{1/2}\gtrsim 1$ TeV unless extremely high integrated luminosities are attained.

Also of importance are the gaugino pair production reactions: wino pair production $pp\to \widetilde{W}_2^{\pm}\widetilde{Z}_4$ and $\widetilde{W}_2^{+}\widetilde{W}_2^{-}$, and also $\widetilde{W}_1^{\pm}\widetilde{Z}_3$ which proceeds via the higgsino component of the bino-like $\widetilde{Z}_3$. Wino pair production can be large due to the large $SU(2)$ triplet gauge coupling. The cross section for this drops off much less sharply than that for $\tilde{g}\tilde{g}$ production since the wino masses are much smaller than the gluino mass. The cross section for $\widetilde{W}_1\widetilde{Z}_3$ production falls off faster than the wino production cross section because the higgsino content of $\widetilde{Z}_3$ drops off with increasing $m_{1/2}$. These reactions constitute the largest observable SUSY cross sections over most of the range of $m_{1/2}$.

For comparison, also shown are cross sections for the pair production of top squarks, the lightest sfermions in RNS. The tiny $\tilde{t}_1\bar{\tilde{t}}_1$ production cross section at $\sqrt{s}=8$ TeV precludes any possibility of stop detection at LHC8. Detection of top-squark pairs at LHC14– which occurs at a lower rate than gluino production unless $m_{1/2}>1$ TeV– may be possible if the stop signal can be sorted from gluino pair production; detection in this case will likely require several hundred fb^{-1} of integrated luminosity.

In Fig. 16, selected electroweak-ino cross sections versus μ for $m_{1/2}=750$ GeV along the RNS model line are shown. Here, $\widetilde{W}_1\widetilde{Z}_2$, $\widetilde{Z}_1\widetilde{Z}_2$ and $\widetilde{W}_1^{+}\widetilde{W}_1^{-}$ production are all comparable and as high as $\sim 10^4$ fb at $\mu\sim 100$ GeV. They drop to the vicinity

of $\sim 10^2$ fb at $\mu \sim 300$ GeV.

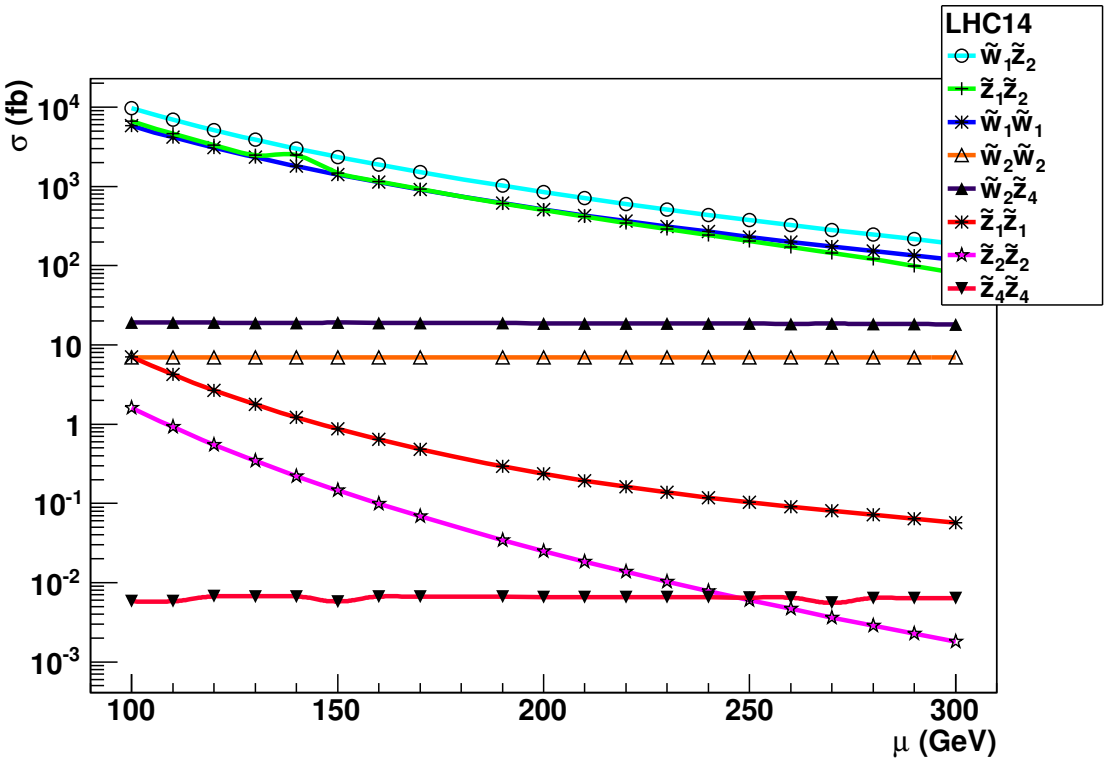


Figure 16: Plot of various NLO electroweak-ino pair production cross sections versus μ for the RNS model line with $m_{1/2} = 750$ GeV for pp collisions at 14 TeV.

4.4 Sparticle branching fractions

Shown in Fig. 17 are various sparticle branching fractions for the sparticles most accessible at the LHC, *i.e.* *a)* $\tilde{g}$, *b)* $\tilde{t}_1$, *c)* $\widetilde{Z}_2$, *d)* $\widetilde{Z}_3$, *e)* $\widetilde{Z}_4$, and *f)* $\widetilde{W}_2$. From frame *a)*, it is apparent that for the lower portion of $m_{1/2}$ corresponding to $m_{\tilde{g}} \lesssim 1.8$ TeV, the gluino decays via 3-body modes into $tb\widetilde{W}_1$ and $t\bar{t}\widetilde{Z}_{1,2,3}$ states. For heavier $m_{\tilde{g}} \gtrsim 1.8$ TeV, the 2-body modes $\tilde{g} \to t\tilde{t}_1$ open up and dominate the decays. Thus, one expects the gluino pair production events to be rich in b-jet activity [73, 74]. In the case where $\tilde{g} \to t\tilde{t}_1$, it is important to know how $\tilde{t}_1$ decays. This is shown in frame *b)*. For the very lowest $m_{1/2}$ values, the $\tilde{t}_1 \to t\tilde{g}$ decay mode is open and is dominant. However, as $m_{1/2}$ increases, this mode quickly closes and instead $\tilde{t}_1$

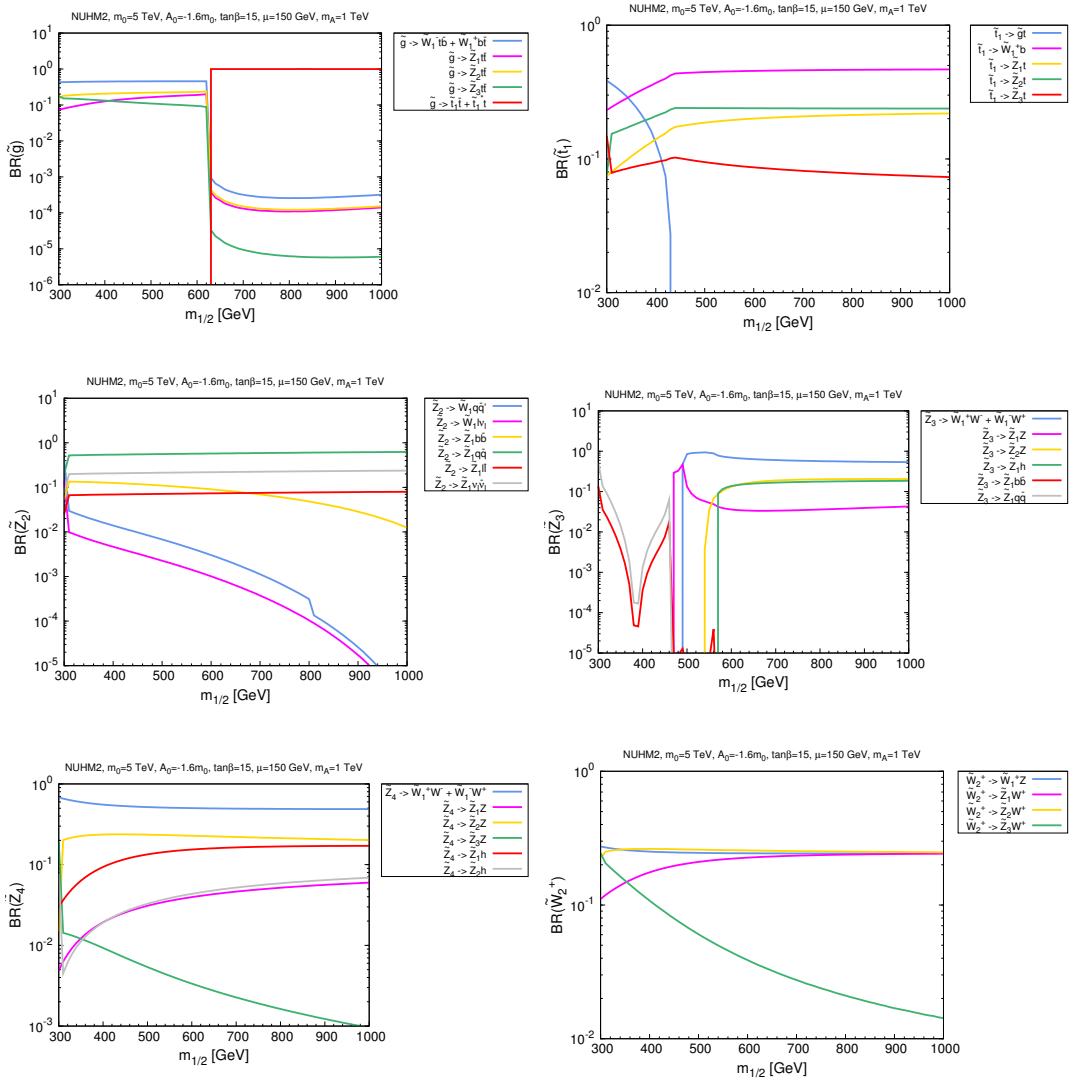


Figure 17: Plot of various sparticle branching fractions versus $m_{1/2}$ along the RNS model line.

decays into $b\widetilde{W}_1$ or $t\widetilde{Z}_{1,2,3}$.

In frame *c*), the $\widetilde{Z}_2$ decay modes are shown. Since the $m_{\widetilde{Z}_2} - m_{\widetilde{Z}_1}$ mass gap ranges from ~ 55 GeV (already excluded for this model line by LHC8 gluino searches) to ~ 10 GeV along the model line, then $\widetilde{Z}_2$ always decays dominantly to 3-body modes $\rightarrow \widetilde{W}_1 f\bar{f}'$ or $\rightarrow \widetilde{Z}_1 f\bar{f}$, where f stands for kinematically accessible SM fermions. As mentioned earlier, since the $\widetilde{Z}_2 - \widetilde{Z}_1$ mass gap is small and the released decay energy is shared between three particles, then the decay products from $\widetilde{Z}_2$ decay are usually very soft – in the few GeV range. The light chargino (branching fractions not shown) decays into $\widetilde{Z}_1 f\bar{f}'$ mainly via W^*, where the f and $\bar{f}'$ are again typically rather soft.

In frame *d*) the bino-like $\widetilde{Z}_3$ decays are shown. Here $\widetilde{Z}_3 \rightarrow \widetilde{W}_1 f\bar{f}'$ or $\widetilde{Z}_{1,2} f\bar{f}$ for $m_{1/2} \lesssim 500$ GeV. For heavier $m_{\widetilde{Z}_3} \gtrsim 220$ GeV (this value depends on the choice of μ), the 2-body decays $\widetilde{Z}_3 \rightarrow \widetilde{W}_1^{\pm} W^{\mp}$ and $\widetilde{Z}_{1,2} Z$ and $\widetilde{Z}_1 h$ turn on, leading to production of vector bosons and Higgs bosons in the SUSY events.

Frames *e*) and *f*) show the neutral $\widetilde{Z}_4$ and charged $\widetilde{W}_2^{\pm}$ wino branching fractions. One sees that $\widetilde{Z}_4 \rightarrow \widetilde{W}_1^{\pm} W^{\mp}$ mode dominates over the entire range of $m_{1/2}$. The subdominant decay modes $\widetilde{Z}_4 \rightarrow \widetilde{Z}_{1,2} Z$ and $\widetilde{Z}_{1,2} h$ can also be important and occur at significant rates. The sizeable branching ratio for the decay $\widetilde{Z}_4 \rightarrow Z\widetilde{Z}_1$ may be surprising at first glance since $\widetilde{Z}_4$ is dominantly a wino while $\widetilde{Z}_1$ is mostly a higgsino, so that the $Z\widetilde{Z}_4\widetilde{Z}_1$ coupling should be suppressed by the small higgsino content $\sim M_Z/M_2$ (assuming $M_2 \gg |\mu|$) of $\widetilde{Z}_4$. For heavy $\widetilde{Z}_4$, this suppression is compensated for by the fact that the amplitude for decay to the longitudinally polarized Z boson is enhanced by $\sim |\mu|/M_Z$. As a result, for $M_2 \gg M_Z, |\mu|$, the branching fractions for decays to Z and to h become comparable. This is discussed in detail in Ref. [75]. In the case of $\widetilde{W}_2$ decay shown in frame *f*), one sees that $\widetilde{W}_2 \rightarrow \widetilde{W}_1 Z$ or $\widetilde{Z}_{1,2} W$ or $\widetilde{W}_1 h$ over the entire range of $m_{1/2}$, leading again to production of gauge and Higgs bosons in wino pair production events. The dominant

Particle	dom. mode	BF
$\tilde{g}$	$\tilde{t}_1 t$	$\sim 100\%$
$\tilde{t}_1$	$b\widetilde{W}_1$	$\sim 50\%$
$\widetilde{Z}_2$	$\widetilde{Z}_1 f\bar{f}$	$\sim 100\%$
$\widetilde{Z}_3$	$\widetilde{W}_1^{\pm} W^{\mp}$	$\sim 50\%$
$\widetilde{Z}_4$	$\widetilde{W}_1^{\pm} W^{\mp}$	$\sim 50\%$
$\widetilde{W}_1$	$\widetilde{Z}_1 f\bar{f}'$	$\sim 100\%$
$\widetilde{W}_2$	$\widetilde{Z}_i W$	$\sim 50\%$

Table 3: Dominant branching fractions of various sparticles along the RNS model line for $m_{1/2} = 1$ TeV.

sparticle branching fractions for $m_{1/2} = 1$ TeV along the RNS model line are shown in Table 3.

4.5 Gluino cascade decay signatures

First, the $pp \to \tilde{g}\tilde{g}X$ reaction followed by gluino cascade decays [76] are examined. This can be searched for in multi-lepton plus multi-jet $+E_T^{\rm miss}$ events. Squark pair production and gluino-squark associated production which occur at very low rates are neglected because squarks are heavy.

Isajet 7.83 [53] is used for the generation of signal events at LHC14. For event generation, a toy detector simulation is used with calorimeter cell size $\Delta\eta \times \Delta\phi = 0.05 \times 0.05$ and $-5 < \eta < 5$. The HCAL (hadronic calorimetry) energy resolution is taken to be $80\%/\sqrt{E} + 3\%$ for $|\eta| < 2.6$ and FCAL (forward calorimetry) is $100\%/\sqrt{E} + 5\%$ for $|\eta| > 2.6$, where the two terms are combined in quadrature. The ECAL (electromagnetic calorimetry) energy resolution is assumed to be $3\%/\sqrt{E} + 0.5\%$. The cone-type Isajet jet-finding algorithm [53] is used to group the hadronic final states into jets. Jets and isolated leptons are defined as follows:

- Jets are hadronic clusters with $|\eta| < 3.0$, $R \equiv \sqrt{\Delta\eta^2 + \Delta\phi^2} \leq 0.4$ and $E_T(jet) > 50$ GeV.

- Electrons and muons are considered isolated if they have $|\eta| < 2.5$, $p_T(l) > 10$ GeV with visible activity within a cone of $\Delta R < 0.2$ about the lepton direction, $\Sigma E_T^{cells} < 5$ GeV.

- Hadronic clusters are identified as b-jets if they contain a B hadron with $E_T(B) > 15$ GeV, $\eta(B) < 3$ and $\Delta R(B, jet) < 0.5$. A tagging efficiency of 60% is assumed, and light quark and gluon jets can be mis-tagged as a b-jet with a probability 1/150 for $E_T \leq 100$ GeV, 1/50 for $E_T \geq 250$ GeV, with a linear interpolation for intermediate E_T values.

Gluino pair production cascade decay signatures have been previously calculated and compared against backgrounds in Ref. [70]. In that paper, it was advocated that in models where gluino pair production signatures are dominant above background (such as the focus point region of mSUGRA), if one can suppress the background entirely, then the remaining total cross section may be used to extract the gluino mass to 10-15% precision. The cuts from that paper are adopted and compared RNS signal rates along the model line against previously calculated backgrounds using the exact same set of cuts.

In Ref. [70], the following pre-cuts set *C1* are first invoked:

C1 Cuts:

$$\begin{aligned} E_T^{\rm miss} &> \max(100 \text{ GeV}, 0.2M_{eff}), \\ n(jets) &\geq 4, \\ E_T(j_1, j_2, j_3, j_4) &> 100,\ 50, 50, 50 \text{ GeV}, \\ S_T &> 0.2, \\ p_T(\ell) &> 20 \text{ GeV}. \end{aligned} \tag{4.5}$$

Here, M_{eff} is defined as in Hinchliffe *et al.* [77] as $M_{eff} = E_T^{\rm miss} + E_T(j_1) + E_T(j_2) +$

$E_T(j_3)+E_T(j_4)$, where j_1-j_4 refer to the four highest E_T jets ordered from highest to lowest E_T, $E_T^{\rm miss}$ is missing transverse energy and S_T is transverse sphericity. The SM cross sections in fb after C1 cuts are listed in Table III of Ref. [70]. It is found that the signal with these cuts is swamped by various SM backgrounds (BG), especially those from QCD multi-jet production and $t\bar{t}$ production. After inspection of a variety of distributions including jet multiplicity $n(jets)$, b-jet multiplicity $n(b-jets)$ and augmented effective mass A_T (here, $A_T = E_T^{\rm miss} + \sum_{leptons} E_T + \sum_{jets} E_T$), for 0ℓ and 1ℓ events, the *C1* cuts are amended to

C2 Cuts:

$$apply\ cuts\ set\ C1$$
$$n(jets) \geq 7$$
$$n(b-jets) \geq 2$$
$$A_T \geq 1400\ \text{GeV}.$$

For multi-lepton events (opposite sign dileptons OS, same sign dileptons SS and trileptons 3ℓ), somewhat softer cuts are used:

C3 Cuts:

$$apply\ cuts\ set\ C1$$
$$n(isol.\ leptons) \geq 2$$
$$n(jets) \geq 4$$
$$n(b-jets) \geq 2$$
$$A_T \geq 1200\ \text{GeV}.$$

After *C2* cuts, it is found that 1 fb of BG remains in the $1\ell + jets$ channel and 0.5 fb of BG remains in the $0\ell + jets$ channel. No BG was found in the

$OS + jets$, $SS + jets$ or $3\ell + jets$ channels after cuts *C3*. The signal rates along the RNS model line are shown in Fig. 18. From the plot, one can read off the 5σ discovery level for various integrated luminosity choices for different signal channels. For the $0\ell + jets$ channel with 300 fb^{-1} a reach to $m_{1/2} \sim 650$ GeV is expected, corresponding to $m_{\tilde{g}} \sim 1.7$ TeV.The reach in the lower background multilepton channels is not projected as these would depend on the residual background that remains.

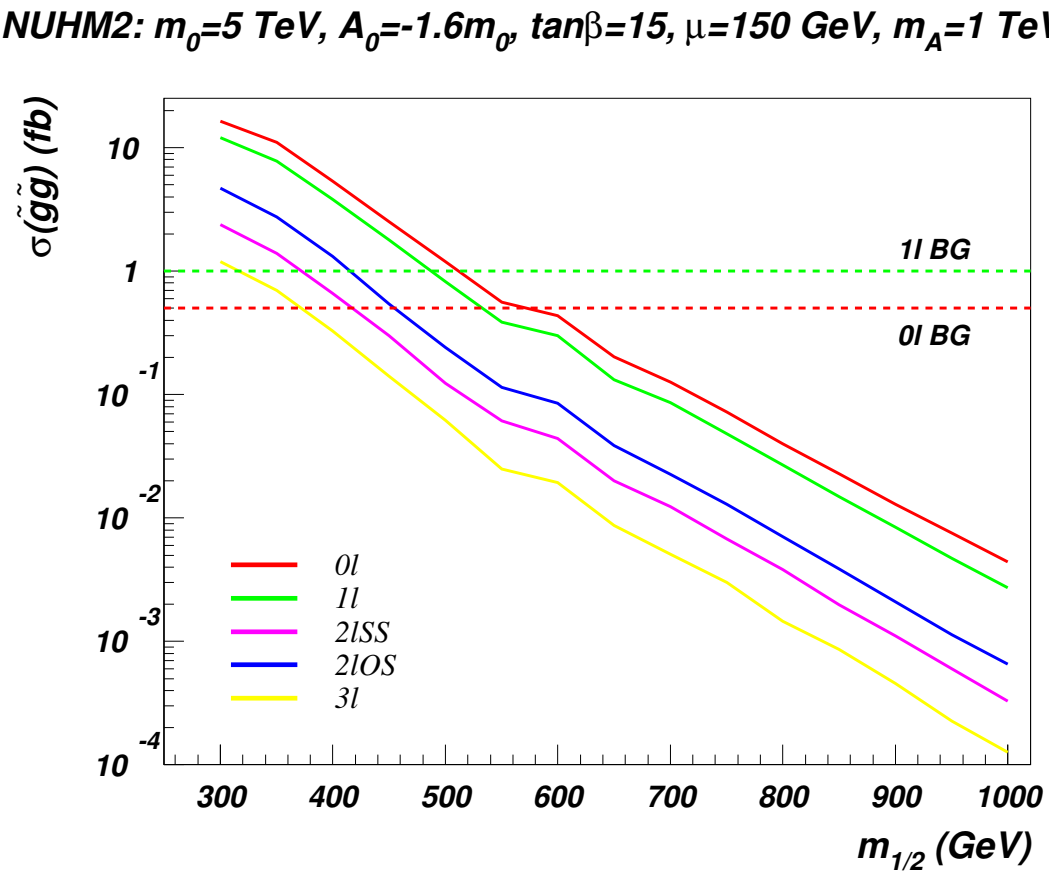


Figure 18: Plot of gluino cross section in fb after cuts *C2* for $1\ell + jets$ and $0\ell + jets$ channel and cuts *C3* for OS, SS and $3\ell + jets$ channels from gluino cascade decays along the RNS model line at LHC14. The horizontal lines denote the corresponding backgrounds estimated in Ref. [70].

4.5.1 OS/SF dilepton mass distribution from cascade decays

Within the OS dileptons plus jets channel, one expects a large fraction of signal events to contain an OS dilepton pair arising from $\widetilde{Z}_2 \to \ell^+\ell^-\widetilde{Z}_1$ decay. For these events, the $m(\ell^+\ell^-)$ distributions will be bounded by the kinematic mass difference $m_{\widetilde{Z}_2} - m_{\widetilde{Z}_1} < M_Z$. In Fig. 19, the invariant mass of opposite-sign/same-flavor dilepton pairs from the $OS + jets$ events which survive cuts *C3* is shown. In the figure, $m_{1/2} = 450$ GeV for which $m_{\tilde{g}} = 1250$ GeV and $m_{\widetilde{Z}_2} - m_{\widetilde{Z}_1} = 32$ GeV. A mass edge at 32 GeV is clearly visible from the plot, as is the Z peak. A detection of an excess of events with a cut-off on the dilepton mass could readily be attributed to neutralinos of SUSY.

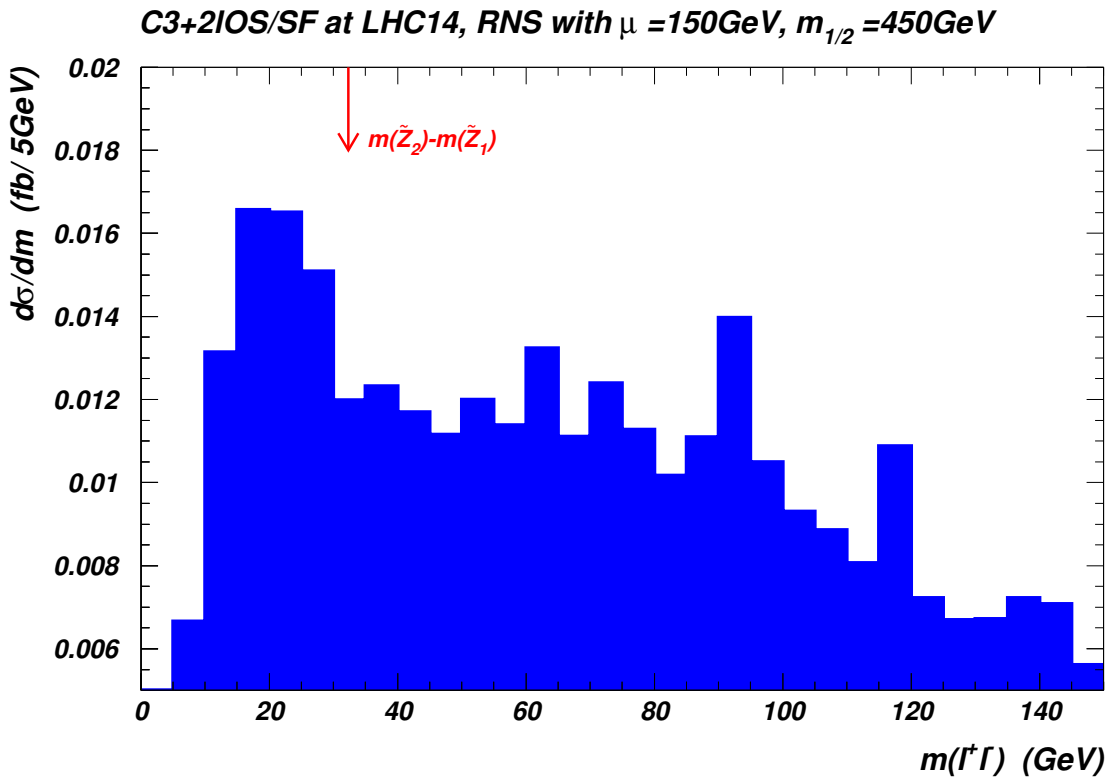


Figure 19: Distribution of the invariant mass of opposite-sign/same-flavor dileptons after cuts *C3* at LHC14 from the RNS benchmark model line with $m_{1/2} = 450$ GeV.

4.6 Same-sign diboson signature

Presented in this section are details on the same-sign diboson (SSdB) signature. In models where $|\mu|$ is smaller than the magnitude of gaugino mass parameters – as exemplified by the RNS model line – wino pair production provides a novel signature with a final state characterized by two same sign W bosons and $E_T^{\rm miss}$ but accompanied by just modest jet activity. The most promising reaction appears to be $pp \to \widetilde{W}_2^{\pm}\widetilde{Z}_4$, where $\widetilde{W}_2^{\pm} \to W^{\pm}\widetilde{Z}_{1,2}$ and $\widetilde{Z}_4 \to W^{\pm}\widetilde{W}_1^{\mp}$ although $\widetilde{W}_2^{+}\widetilde{W}_2^{-}$ pair production also provides a non-negligible signal contribution. It is seen in Fig. 17 that the winos have substantial branching fractions for decays to W bosons. For these decays, half the time the final states consist of $W^{\pm}W^{\pm} + E_T^{\rm miss}$. The analysis here is focused on the SS dilepton signal from the leptonic decays of both Ws. The jet activity in these events is relatively limited since the daughter higgsinos $\widetilde{W}_1$ and $\widetilde{Z}_{1,2}$ usually yield only soft decay products. This serves to distinguish the wino-pair induced SSdB signature from the SS dilepton signal from gluino pair production – the latter is expected to be accompanied by several hard jets.

The SM physics backgrounds to the SSdB signal come from $uu \to W^+W^+dd$ or $dd \to W^-W^-uu$ production with a cross section ~ 350 fb. These events will be characterized by high rapidity (forward) jets and rather low $E_T^{\rm miss}$. $W^{\pm}W^{\pm}$ pairs may also occur via two overlapping events: such events will mainly have low p_T Ws and possibly distinct production vertices. Double parton scattering will also lead to SSdB events at a rate somewhat lower than the $qq \to W^{\pm}W^{\pm}q'q'$ process [78]. Additional physics backgrounds come from $t\bar{t}$ production where a lepton from a daughter b is accidentally not isolated, from $t\bar{t}W$ production and from $4t$ production. SM processes such as $WZ \to 3\ell$ and $t\bar{t}Z \to 3\ell$ production, where one lepton is missed, constitute reducible backgrounds to the signal.

Here, it is assumed that the $2 \to 4$ processes as well as the double parton scattering processes, which have different characteristics from the signal, can be

readily eliminated by suitable cuts and do not simulate these. AlpGen [79] is used for the simulation of the remaining background events and MadGraph 5 [80] is used to generate the hard scattering events. Those events are then passed to Pythia 6.4 [81] via the LHE interface [82] for showering and hadronization. For the $2 \to 4$ "WZ" process, the full matrix element for $pp \to l^+l^-l'\nu'$ that includes contributions from on- and off-shell Z and γ as well as from interference diagrams is computed. Signal and background are normalized to NLO cross sections obtained with Prospino [72] and MCFM [83], respectively. The procedure to reconstruct jets and isolated leptons that was followed is described in Sec. 4.5.

The following cuts are imposed:

- *exactly* 2 isolated same-sign leptons with $p_T(\ell_1) > 20$ GeV and $p_T(\ell_2) > 10$ GeV,
- $n(b-jets) = 0$ (to aid in vetoing $t\bar{t}$ background).

After these cuts, the event rate is dominated by WZ and $t\bar{t}$ backgrounds.

To distinguish signal from background, the transverse mass of each lepton is constructed with $E_T^{\rm miss}$:

$$m_T^{\rm min} \equiv \min\left[m_T(\ell_1, E_T^{\rm miss}), m_T(\ell_2, E_T^{\rm miss})\right] .$$

The signal gives rise to a continuum distribution, while the dominant backgrounds have a kinematic cut-off around $m_T^{\rm min} \simeq M_W$ (as long as the $E_T^{\rm miss}$ dominantly arises from the leptonic decay of a single W). The situation is seen in Fig. 20, where in *a*) the $m_T^{\rm min}$ distribution is shown, while in *b*) the $E_T^{\rm miss}$ distribution is shown. The bulk of $t\bar{t}$ and WZ backgrounds can be eliminated by requiring

- $m_T^{\rm min} > 125$ GeV and
- $E_T^{\rm miss} > 200$ GeV.

After these cuts, no background events were generated from $t\bar{t}$ and WZ production, where the 1-event level in the simulation was 0.05 fb and 0.023 fb, respectively. The dominant SM background for large $m_T^{\rm min}$ then comes from $Wt\bar{t}$ production for which (including a QCD k-factor $k = 1.18$ obtained from Ref. [84]) a cross section of 0.019 (0.006) fb is found after the cuts $m_T^{\rm min} > 125$ (175) GeV and $E_T^{\rm miss} > 200$ GeV; the harder cuts serve to optimize the signal reach for high $m_{1/2}$ values.

The calculated signal rates after cuts along the RNS model line from just $\widetilde{W}_2^{\pm}\widetilde{Z}_4$ and $\widetilde{W}_2^{\pm}\widetilde{W}_2^{\mp}$ production are shown vs. $m_{1/2}$ in Fig. 21 where the upper (blue) curves require $m_T^{\rm min} > 125$ GeV and the lower (orange) curve requires $m_T^{\rm min} > 175$ GeV. The $\widetilde{W}_2\widetilde{Z}_4$ and $\widetilde{W}_2\widetilde{W}_2$ cross sections are normalized to those from Prospino [72]. For observability with an assumed value of integrated luminosity, it is required: 1) significance $> 5\sigma$, 2) Signal/BG> 0.2 and 3) at least 5 signal events. The LHC signal (blue dashed curve) and reach lines for integrated luminosity values 25 and 100 fb^{-1} with a soft $E_T^{\rm miss} > 75$ GeV cut are shown first. The 25 fb^{-1} reach is to $m_{1/2} \simeq 450$ GeV corresponding to gluinos of ~ 1300 GeV. As greater integrated luminosity is accumulated, harder cuts can be applied. The solid blue line shows signal for $E_T^{\rm miss} > 200$ GeV and reach for 100, 300 and 1000 fb^{-1}. With harder cuts, the 100 fb^{-1} reach extends to $m_{1/2} \simeq 680$ GeV corresponding to $m_{\tilde{g}} \sim 1.75$ TeV in a model with gaugino mass unification. The direct search for $\tilde{g}\tilde{g}$ gives a projected reach of $m_{\tilde{g}} \sim 1.6$ TeV as seen in Sec. 4.5; see also Ref. [85]. Thus, with $\mathcal{O}(100)$ fb^{-1} of integrated luminosity, the SS diboson signal offers a comparable reach to that for gluino cascade decays. For 300 (1000) fb^{-1} of integrated luminosity, the reach is improved with a harder $m_T^{\rm min} > 175$ GeV cut. In this case, the LHC14 reach for SS dibosons extends to $m_{1/2} \sim 840$ (1000) GeV, corresponding to $m_{\tilde{g}}$ of 2.1 and 2.4 TeV. For the RNS model-line where gaugino mass unification is assumed, these reach numbers extend well beyond the LHC14 reach for direct gluino pair production [86]. Regardless of this, the SSdB signal is a new independent signal, and

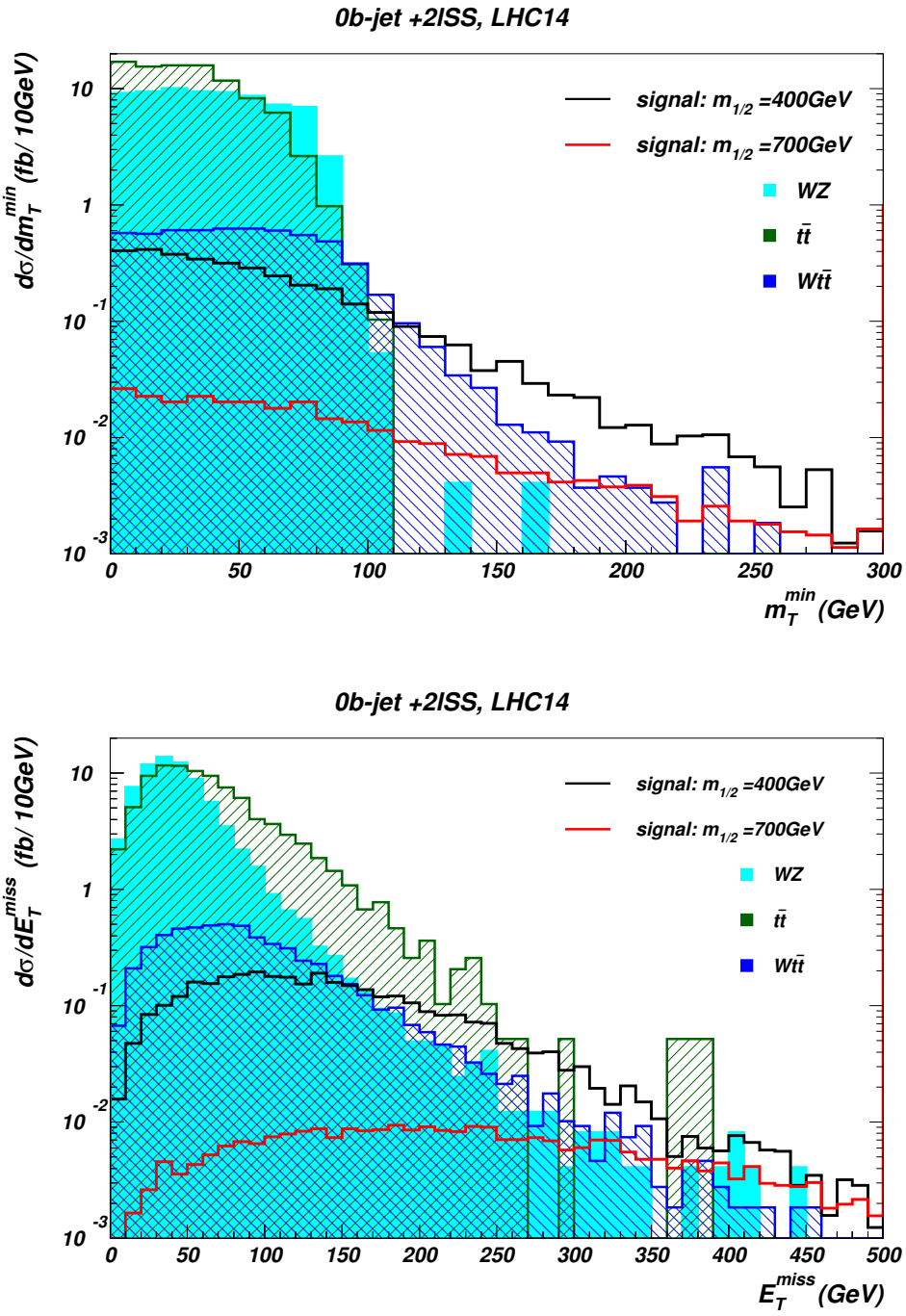


Figure 20: Transverse mass and missing energy distributions for SSdB events after cuts at LHC14. The open black and red histograms represent the signal from winos – via $\widetilde{W}_2\widetilde{Z}_4$ and $\widetilde{W}_2^+\widetilde{W}_2^-$ pair production – for the RNS model-line points with $m_{1/2} = 400$ GeV and 700 GeV, respectively.

detection of signals in multiple channels will be essential to unravel the underlying origin of any new physics that is found.

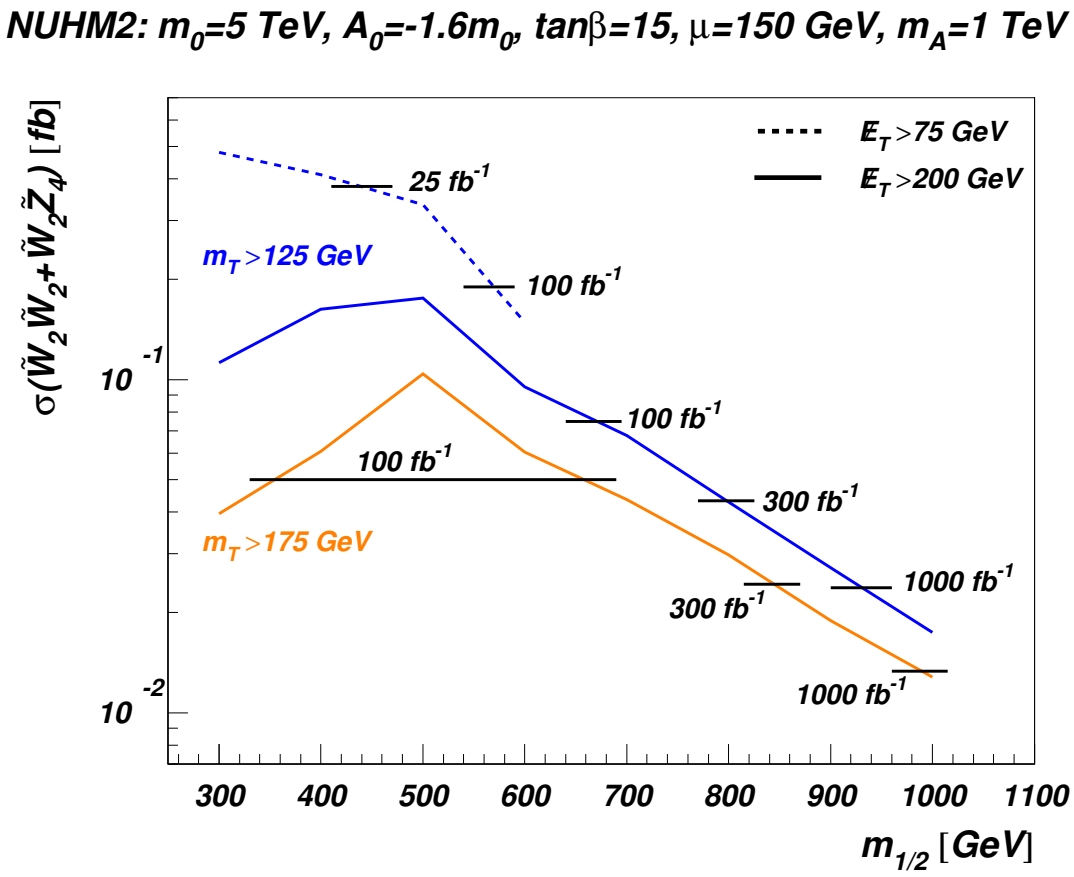


Figure 21: Same-sign dilepton cross sections (in *fb*) at LHC14 after cuts vs. $m_{1/2}$ along the RNS model line from $\widetilde{W}_2^{\pm}\widetilde{Z}_4$ and $\widetilde{W}_2^{\pm}\widetilde{W}_2^{\mp}$ production and calculated reach for 100, 300 and 1000 fb^{-1}. The upper solid and dashed (blue) curves requires $m_T^{\rm min} > 125$ GeV while the lower solid (orange) curve requires $m_T^{\rm min} > 175$ GeV. The signal is observable above the horizontal lines.

The low jet activity associated with the SSdB signal from SUSY models with light higgsinos makes it quite distinct from the usual SS dilepton signal arising from gluino pair production, which is usually accompanied by numerous hard jets and high $E_T^{\rm miss}$. Recent CMS searches for SS dileptons from SUSY [87] required the

presence of multiple jets (some b-tagged jets) or large H_T in the events; these cuts greatly reduce or even eliminate the SSdB signal. Likewise, the cuts $n_j \geq 3$ high p_T jets (possibly b-tagged) along with $E_T^{\rm miss} > 150$ GeV and large $m_{\rm eff}$ required by a recent ATLAS search for SS dileptons from gluinos [88] would have eliminated much of the SSdB signal from SUSY with light higgsinos.

Hard trilepton production from winos (discussed in the next section) can lead to clean, same-sign dilepton events if a lepton is not isolated or fails to be identified. The CMS collaboration used this channel to extend the search for electroweak-inos to portions of parameter space not accessible via the trilepton search, requiring 120 GeV $< E_T^{\rm miss} <$ 200 GeV [89]. They do not, however, impose the $m_T^{\rm min}$ cut that was crucial for the SSdB analysis. The CMS search is thus not optimized for the clean SS dilepton signal in the RNS scenario. In any case, with just ~ 20 fb^{-1} at LHC8, this channel should have a lower reach than that via multi-jet plus multi-lepton events from gluino pair production.

4.7 Hard trileptons from wino pair production

In this section, prospects for detection of reactions such as

$$pp \to \widetilde{W}_2\widetilde{Z}_4 \to (\widetilde{W}_1 Z) + (\widetilde{W}_1 W) \to WZ + E_T^{\rm miss} \to \ell^+\ell^-\ell' + E_T^{\rm miss}.$$

are examined. The trilepton channel where the neutralino decays via the three-body decay $\widetilde{Z}_2 \to \ell^+\ell^-\widetilde{Z}_1$ because the two-body decay $\widetilde{Z}_2 \to Z\widetilde{Z}_1$ is kinematically forbidden (so that SM trileptons from WZ production can be eliminated via a mass cut on the opposite-sign, same flavor dilepton pair) has long been regarded as a golden channel in the search for gauginos from supersymmetry [90]. More recently, it has been pointed out [91] that at least within mSUGRA the trilepton search for gauginos is viable even when the neutralinos decay to on-shell Z bosons. Indeed, the

CMS and ATLAS experiments have searched in this channel and found that there is no excess above SM expectations [92]. For a recent assessment of multilepton signals, see Ref. [75]. Here, prospects for this signal for the RNS model line are analysed, for the most part following the cuts of Ref. [91] which required:

Pre-Selection Cuts:

- $n(b-jets)=0$ (to aid in vetoing $t\bar{t}$ background),
- 3 isolated leptons with $p_T(\ell)>20$ GeV and
- $|m(\ell^+\ell^-)-M_Z|<10$ GeV (leptonic Z),

where two of the leptons in the event must form an OS/SF pair. If more than one OS/SF pairing is possible, the pair which minimizes $|m(\ell^+\ell^-)-M_Z|$ is chosen. The remaining lepton is labeled ℓ'. In the case of the RNS model line, the $WZ+E_T^{\rm miss}$ signal also receives a smaller, though non-negligible contribution, from $\widetilde{W}_2^+\widetilde{W}_2^-$ where one of the winos decays via $\widetilde{W}_2\to W\widetilde{Z}_{1,2}$ and the other via $\widetilde{W}_2\to Z\widetilde{W}_1$ mode. At this point, a large background from the $2\to 4$ process $pp\to(\ell^+\ell^-)+(\ell^{\pm\prime}\nu_{\ell'})$ which occurs via various on- and off-shell processes – including W^*Z^* and $W^*\gamma^*$ production – tends to dominate the signal. Here, the $2\to 4$ process is evaluated using MadGraph with no restriction on the invariant mass around the Z and W resonances. For $t\bar{t}$, $Z(ll)+jets$, $W(l\nu)+jets$, $Z(ll)+t\bar{t}$ and $W(l\nu)+t\bar{t}$ (all summed over 3 lepton flavors) at least two additional partons in the final state are allowed, and the MLM matching scheme [93] is used to avoid double counting. Also included are ZZ, $W(l\nu)+tb$ and $Z(ll)+b\bar{b}$ backgrounds. The signal and background distributions in $m_T(\ell',E_T^{\rm miss})$ and $E_T^{\rm miss}$ are shown in Fig. 22.

To enhance the signal relative to background, it is required that,

- $m_T(\ell',E_T^{\rm miss})>125$ GeV,
- $E_T^{\rm miss}>150$ GeV.

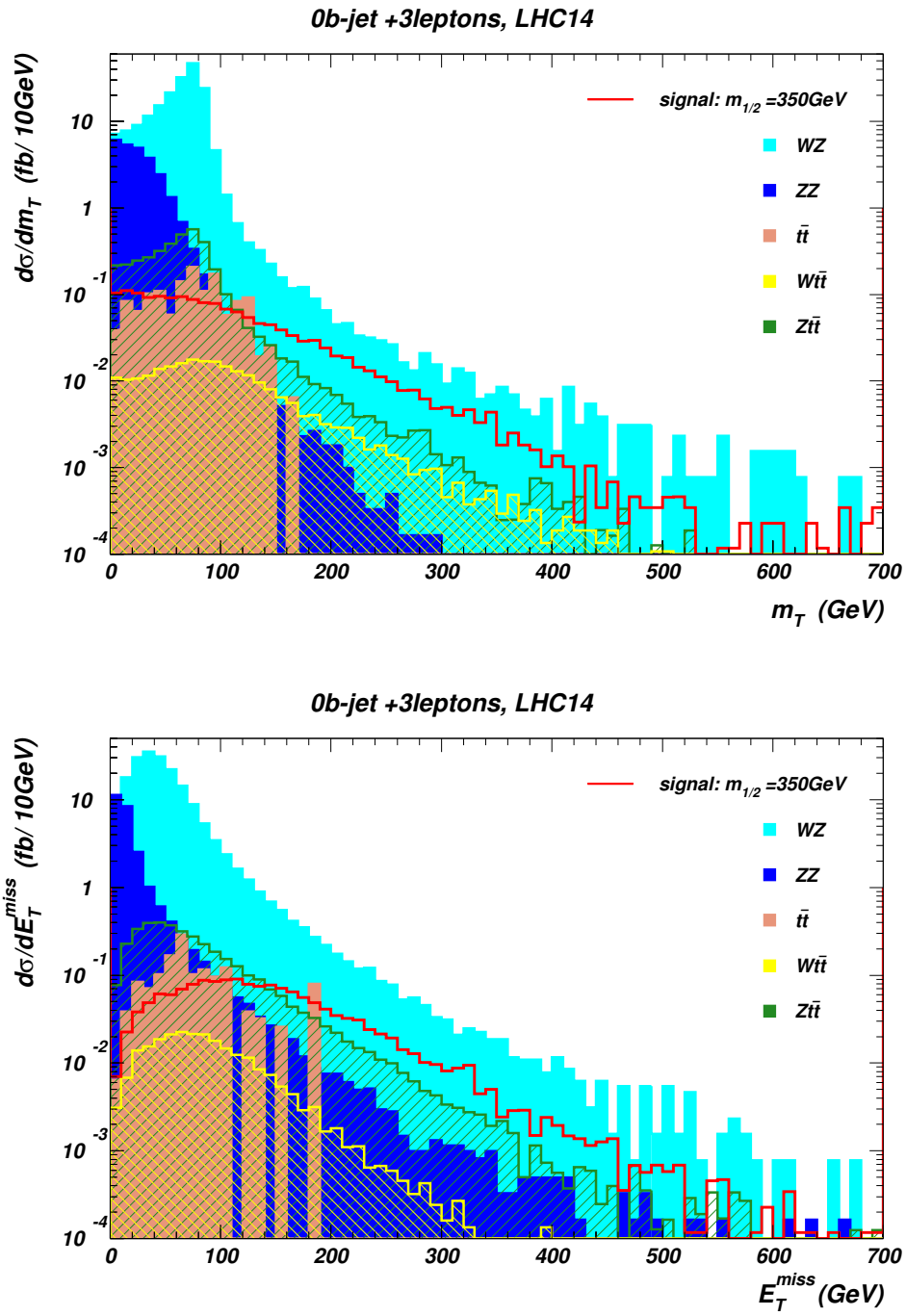


Figure 22: Transverse mass and missing energy distributions for hard trilepton events after the preliminary cuts at LHC14. The open red histograms represent the signal from winos, $\widetilde{W}_2$ and $\widetilde{Z}_4$, for the RNS point with $m_{1/2} = 350$ GeV.

	$t\bar{t}$	WZ	ZZ	$Z+t\bar{t}$	$W+t\bar{t}$	Total BG	Signal
Events Generated	12M	1.5M	1M	1.2M	10M		200K
$n(b)=0, n(l)=3$	6.96	211.94	26.07	4.26	1.84	247.29	2.88
OS/SF pair	5.25	211.51	26.02	4.21	1.37	251.97	2.57
$m(\ell^+\ell^-)$ cut	0.95	186.90	25.55	3.99	0.24	221.20	1.52
$m_T > 125$ GeV	0.03	1.64	0.05	0.20	0.07	1.99	0.43
$E_T^{\rm miss} > 150$ GeV	0.006	0.24	< 0.00085	0.0058	0.016	0.32	0.22

Table 4: Number of events generated and cross section after cuts for the dominant backgrounds in the hard trilepton channel and for the RNS signal with $m_{1/2} = 350$ GeV. All cross sections are in *fb*. The total BG values include all processes listed in the text, including the subdominant ones not shown in the Table.

The m_T cut is as in Ref. [91], but for the larger integrated luminosity and concomitantly higher wino masses that are considered here, one finds that stiffening the $E_T^{\rm miss}$ cut yields a better signal-to-background ratio. The background from various SM sources along with RNS signal for $m_{1/2} = 350$ GeV is shown after cuts in Table 4 for LHC14.

Shown in Fig. 23 is the $3\ell + E_T^{\rm miss}$ signal cross section after all cuts versus $m_{1/2}$ along the RNS model line. The turn-over at the left end of the curve is because of the efficiency loss resulting from the stiff $E_T^{\rm miss}$ cut which is optimized to yield the best reach for high wino masses. For 100 fb^{-1} of integrated luminosity, there is no reach, while the reach in $m_{1/2}$ is shown for 300 and 1000 fb^{-1}. The 300 fb^{-1} reach extends to $m_{1/2} = 500$ GeV while the 1000 fb^{-1} reach extends to $m_{1/2} = 630$ GeV. These values correspond to gluino masses of $m_{\tilde{g}} = 1.3$ TeV and 1.65 TeV, respectively. These reaches are smaller than those obtained from the $\tilde{g}\tilde{g}$ and SSdB signals. They would, nevertheless, offer corroborative evidence for any SUSY discovery at the lower range of allowed $m_{1/2}$ values.

4.8 Four leptons from heavy gaugino production

In Fig. 17 it was seen that the wino-like $\widetilde{W}_2$ and $\widetilde{Z}_4$ have significant branching fractions to W and Z bosons resulting in the dilepton and trilepton signals already

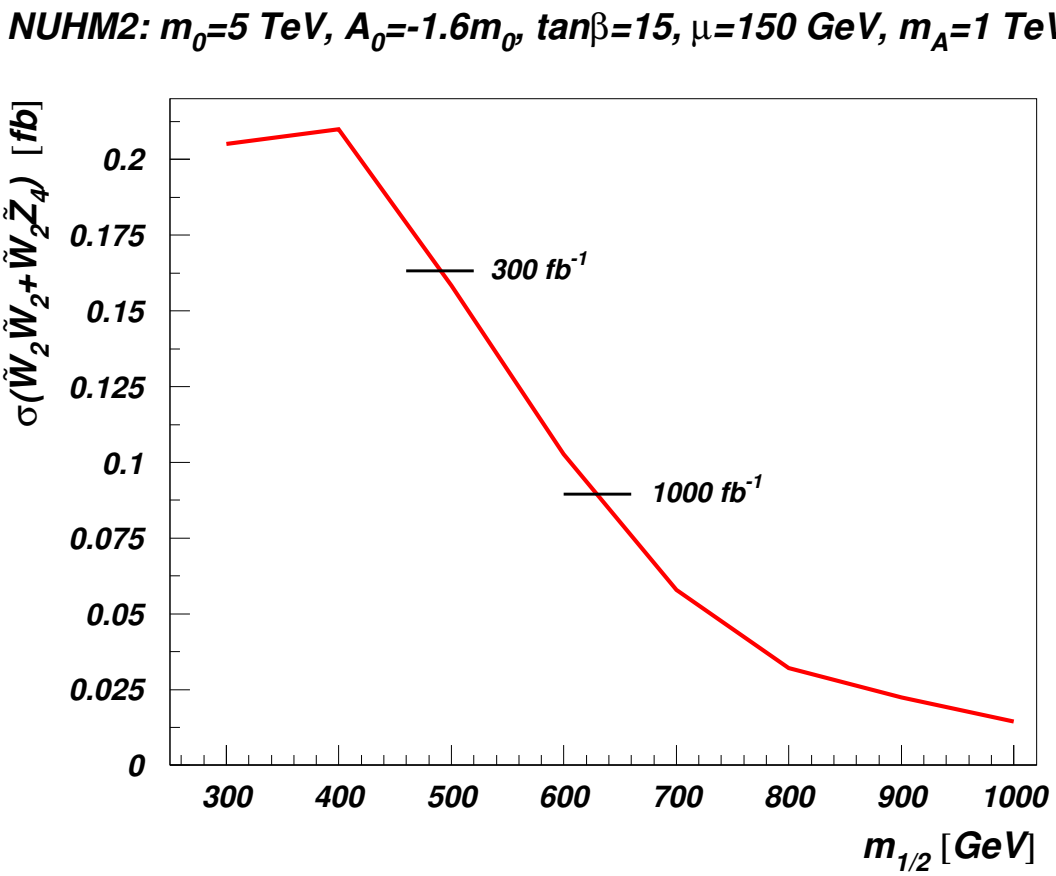


Figure 23: Tri-lepton cross sections (in *fb*) at LHC14 after cuts vs. $m_{1/2}$ along the RNS model line from wino pair production processes $pp \to \widetilde{W}_2\widetilde{Z}_4/\widetilde{W}_2\widetilde{W}_2 \to WZ + E_T^{\rm miss} \to 3\ell + E_T^{\rm miss}$ events.

discussed. A small fraction of the time, there may be two Z bosons in these events, leading to the possibility of a four-lepton signal. Additional leptons can arise from the leptonic decays of daughter $\widetilde{W}_1$ and $\widetilde{Z}_2$. Although the decay products are generally soft, the ubiquity of these light higgsino-like states within the RNS framework often results in additional detectable leptons (e and μ) in would-be trilepton events. This characteristic feature of low $|\mu|$ models such as RNS is absent in models such as mSUGRA, and leads to the possibility of four-lepton plus $E_T^{\rm miss}$ signal, even in R-parity conserving SUSY. A study of this new signal for which it is required that

- 4 isolated leptons with $p_T(\ell) > 10$ GeV within $|\eta(\ell)| < 2.5$,
- $n_b = 0$, to veto backgrounds from top decays,
- $E_T^{\rm miss} > E_T^{\rm miss}({\rm cut})$, where $E_T^{\rm miss}({\rm cut})$ is chosen to select signal events above SM backgrounds,

is the subject of this section.

Within the SM, the main sources of $4\ell + E_T^{\rm miss}$ events are ZZ, $Zt\bar{t}$, ZWW, ZZW, ZZZ and $Zh(\rightarrow WW^*)$, followed by leptonic decays of tops, and of the electroweak vector bosons. The bulk of the background from ZZ production is eliminated by requiring a large $E_T^{\rm miss}$. Nevertheless, this background remains significant since $E_T^{\rm miss}$ can arise via $Z \rightarrow \tau^+\tau^- \rightarrow \ell^+\ell'^- + E_T^{\rm miss}$.

The RNS signal, along with backgrounds from ZZ, $t\bar{t}Z$ and VVV ($V = W, Z$), is simulated using AlpGen and Pythia. The cross sections for the most important of these backgrounds are listed in the second column of Table 5, together with that for the signal for three model-line points. The last two columns list these signal and background calculations for $E_T^{\rm miss}({\rm cut}) = 100$ and 200 GeV, the choice being motivated by the $E_T^{\rm miss}$ distributions shown in Fig. 24. The numbers in bold-face show the statistical significance for an integrated luminosity of 300 fb^{-1}.

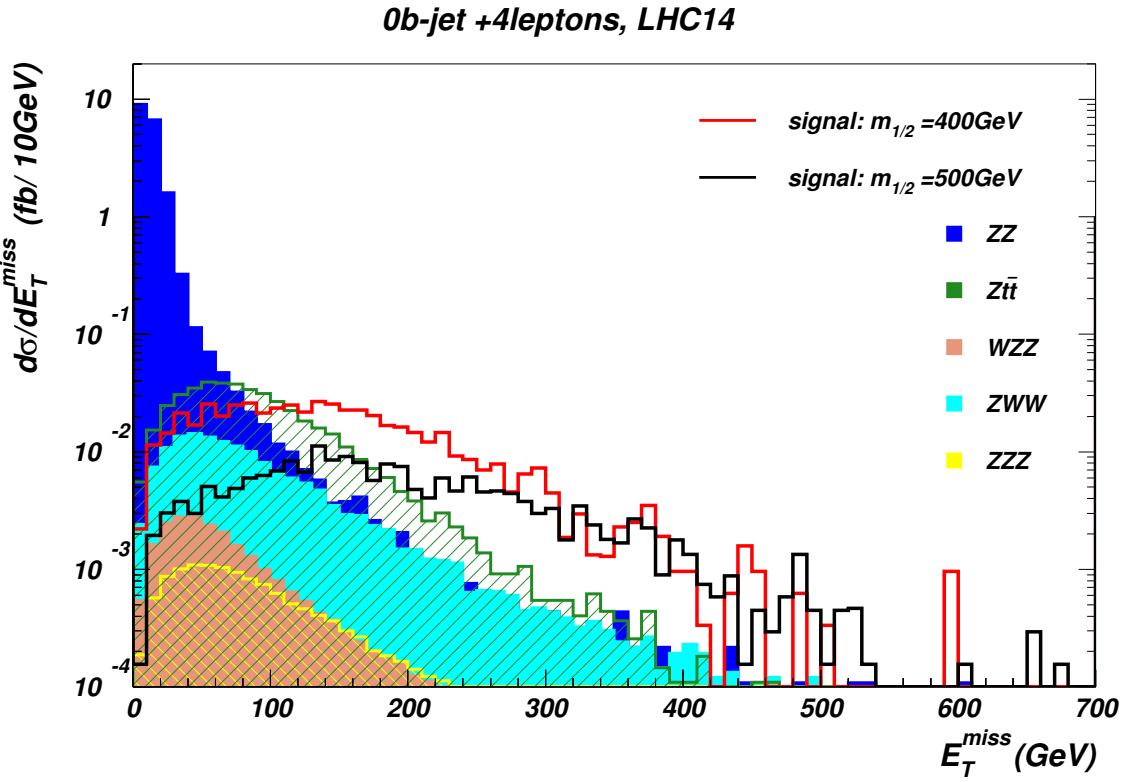


Figure 24: The $E_T^{\rm miss}$ distributions for 4ℓ events with $n_b = 0$ from various SM sources and for two signal points on the RNS model-line.

cuts	$n(b) = 0, n(l) = 4$	$E_T^{\rm miss} > 100$ GeV	$E_T^{\rm miss} > 200$ GeV
ZZ	18.02	0.0611	0.0094
$Zt\bar{t}$	0.450	0.158	0.0232
ZWW	0.155	0.0516	0.0134
Total BG	18.66	0.280	0.0483
$m_{1/2} = 400$ GeV	0.527	0.343 (**11.2**)	0.122 (**3.8**)
$m_{1/2} = 500$ GeV	0.195	0.157 (**5.1**)	0.0769 (**6.1**)
$m_{1/2} = 600$ GeV	0.084	0.0728 (**2.3**)	0.0467 (**3.7**)

Table 5: Background and signal rates in fb for 4-lepton events at LHC14 after cuts. The bold-faced numbers in parenthesis in the last two columns show the statistical significance of the signal with 300 fb^{-1} of integrated luminosity at LHC14. The signal comes from wino pair production for points on the RNS model line introduced in the text.

It is estimated that $Zh(\to W^{\pm}\ell\nu)$ yields a 4ℓ cross section ~ 1300 fb $\times 0.06 \times 0.22 \times 0.03$ (where the last factor is the branching fraction for $h \to W^{\pm}\ell^{\mp}\nu$ decay) $\simeq 0.5$ fb, before any lepton acceptance cuts which further reduce the cross section by factor about 5-10. After the hard $E_T^{\rm miss}$ requirement, one may expect expect this to make a relatively unimportant contribution to the background. Backgrounds from $ttWW$ and $4V$ processes should also be small.

Several comments are worth noting:

- there is no benefit, and in fact a loss of significance, by requiring pairs of leptons to reconstruct to M_Z. This is largely because the largest 4ℓ backgrounds also all have a Z in them, and both signal and backgrounds drop roughly equally due to this requirement.

- the softer $E_T^{\rm miss} > 100$ GeV cut works better for $m_{1/2} = 400$ GeV for which a 6σ signal is obtained even with just 100 fb^{-1} of integrated luminosity.

- the 5σ reach for 300 fb^{-1} (1000 fb^{-1}) extends to $m_{1/2} = 500$ GeV (beyond $m_{1/2} = 600$ GeV) with the harder $E_T^{\rm miss}({\rm cut}) = 200$ GeV.

In conclusion, the 4ℓ channel would serve to confirm a the SSdB signal pointing to light higgsinos out to $m_{1/2}$ values $\lesssim 500 - 650$ GeV, depending on the integrated luminosity that is ultimately available.

Current ATLAS [94] and CMS [95] 4-lepton searches are optimized for the signal from the cascade decays of gluinos (and so do not veto hadronic activity) with the high lepton multiplicity originating in R-parity violating leptonic decays of $\widetilde{Z}_1$. In contrast, the signal described here is hadronically quiet and would stand out over SM backgrounds with veto on b-jets as described in the text.

4.9 Soft trileptons from direct higgsino pair production

In this Section, an attempt to exploit the large cross sections for higgsino pair production from the RNS model at the LHC is presented: $pp \to \widetilde{W}_1\widetilde{Z}_1,\ \widetilde{W}_1^+\widetilde{W}_1^-,\ \widetilde{Z}_1\widetilde{Z}_2$ and $\widetilde{W}_1^\pm\widetilde{Z}_2$. The purely hadronic+$E_T^{\rm miss}$ final states from higgsino pair production are expected to be buried beneath prodigious QCD backgrounds since the signal yields only soft, low p_T jets and soft $E_T^{\rm miss}$ spectra. Likewise, most single and dilepton signals are expected to be buried under $W \to \ell\nu_\ell$ and WW, $t\bar{t}$ backgrounds respectively. Examined here is the clean trilepton signal from higgsino pair production by searching for the $pp \to \widetilde{W}_1\widetilde{Z}_2 \to (e\nu_e\widetilde{Z}_1) + (\mu^+\mu^-\widetilde{Z}_1)$ topology where a dilepton trigger with $p_T(e) > 10$ GeV and $p_T(\mu) > 5$ GeV is assumed. It is required that:

- 10 GeV $< p_T(e) <$ 50 GeV,
- 5 GeV $< p_T(\mu_1) <$ 50 GeV,
- 5 GeV $< p_T(\mu_2) <$ 25 GeV.

Scrutiny of a variety of distributions suggests the following cuts:

1. 10 GeV $< m(\mu^+\mu^-) <$ 75 GeV,
2. $n(jets) = 0$ (jet-veto),
3. electron transverse mass $m_T(e, E_T^{\rm miss}) <$ 60 GeV,
4. 25 GeV $< E_T^{\rm miss} <$ 100 GeV.

The signal and four background processes are shown in Table 6. Shown in Fig. 25 are distributions of electron p_T before cuts for two sample points on the RNS model line. The energy release is very small, less than $\sim$ 25 GeV, and quickly decreases with $m_{1/2}$. For $m_{1/2} = 1$ TeV most of electrons have p_T less than 10 GeV, the trigger

cuts	$t\bar{t}$	W^*Z^*	ZZ	$Wt\bar{t}$	signal
cut 1	12.4	7.6	0.15	0.1	0.42
cut 2	2.4	7.1	0.09	0.006	0.42
cut 3	1.3	4.4	0.08	0.003	0.42
cut 4	0.9	2.0	0.03	0.002	0.28

Table 6: Background and signal rates in fb for soft $3\ell + E_T^{\rm miss}$ events at LHC14 after cuts. The signal comes from higgsino pair production at $m_{1/2} = 400$ GeV point on the RNS model line. The $2 \to 4$ process labelled W^*Z^* includes $\gamma^*,\ Z^* \to \tau\bar{\tau}$.

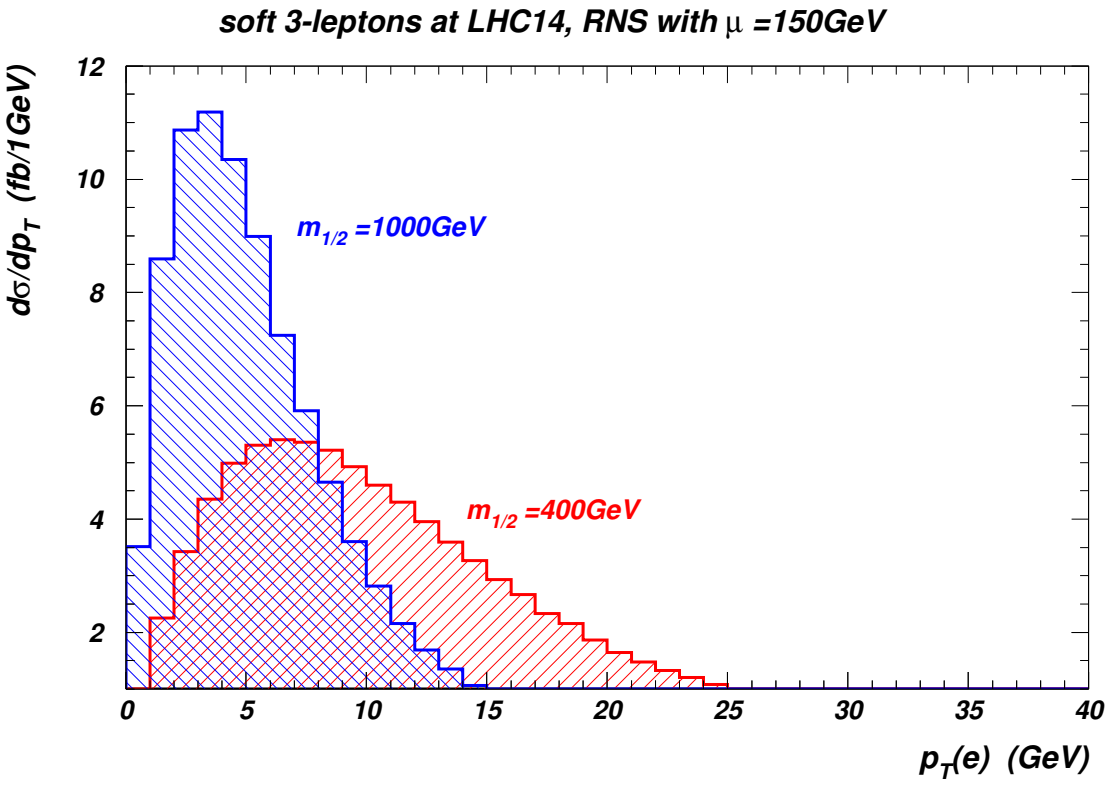


Figure 25: $p_T(e)$ distribution for soft tri-leptons from higgsino pairs before cuts for two RNS points with $m_{1/2} = 400$ GeV (red) and 1000 GeV (blue) at LHC14.

Int. lum. (fb^{-1})	$\tilde{g}\tilde{g}$	SSdB	$WZ \to 3\ell$	4ℓ
10	1.4	–	–	–
100	1.6	1.6	–	~ 1.2
300	1.7	2.1	1.4	$\gtrsim 1.4$
1000	1.9	2.4	1.6	$\gtrsim 1.6$

Table 7: Reach of LHC14 for SUSY in terms of gluino mass, $m_{\tilde{g}}$ (TeV), assuming various integrated luminosity values along the RNS model line. Presented is each search channel considered except soft 3ℓ.

threshold. After cut 4, the background exceeds signal by a factor of 10. The dimuon invariant mass distribution after cuts is shown in Fig. 26*a*) for $m_{1/2} = 400$ GeV ($\widetilde{Z}_2 - \widetilde{Z}_1$ mass gap at 38 GeV), *b*) $m_{1/2} = 550$ GeV (mass gap at 25 GeV) and *c*) $m_{1/2} = 700$ GeV (mass gap at 18 GeV). The shapes of the dilepton mass distribution for the signal+background in frame *a*) differs from that of the background alone. A shape analysis using the data at large $m_{\ell\ell}$ to normalize the background may allow one to claim a signal, given sufficient integrated luminosity, since an excess of events should be found in bins with $m(\mu^+\mu^-) < 38$ GeV as compared to higher mass bins where a theory-experiment match is expected. For a counting analysis alone, invoking a cut $m(\mu^+\mu^-) < 38$ GeV, a 5σ signal over background (without any requirement on the S/B ratio) would require about 700 fb^{-1} of integrated luminosity. In the other frames with the smaller mass gap, an excess only appears in the lowest mass bin(s) and the possibility of extracting a signal appears even more difficult.

The final reach situation for CERN LHC is summarized in Table 7, where the 5σ reach in terms of $m_{\tilde{g}}$ is given for various discovery channels and integrated luminosity values. While LHC14 can explore RNS up to $m_{\tilde{g}} \sim 2$ TeV for 300 fb^{-1}, a large swath of parameter space with $m_{\tilde{g}} \sim 2 - 5$ TeV seemingly lies beyond LHC14 reach.

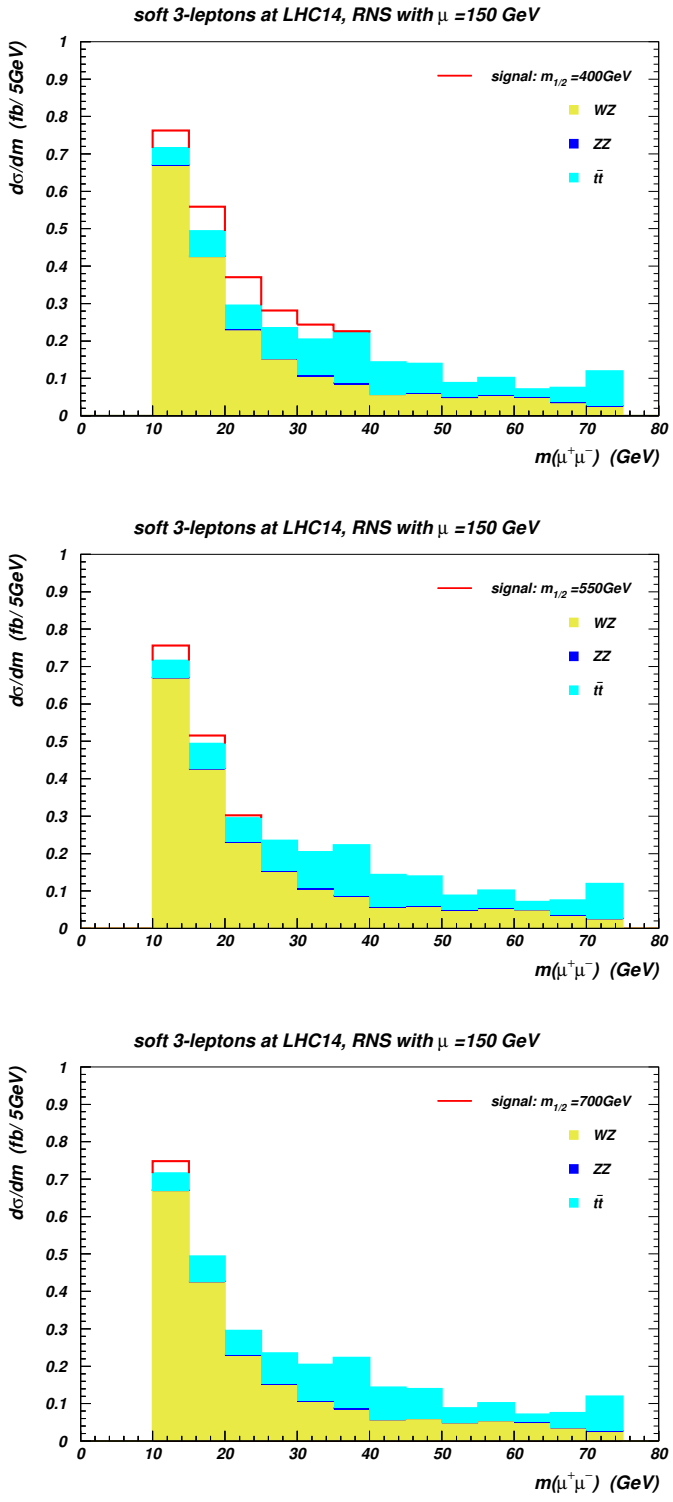


Figure 26: The dimuon invariant mass distributions after cuts for $e\mu\mu$ events. Open red histograms represent signals from higgsino pair productions for three points with $m_{1/2} = 400,\ 550$ and 700 GeV along the RNS model line.

5 Physics at a higgsino factory [96]

As seen in the last chapter, light higgsinos can be produced at large rates at LHC8 and LHC14. However, the compressed higgsino spectrum leads to only small visible energy release from $\widetilde{W}_1 \to \widetilde{Z}_1 f \bar{f}'$ and $\widetilde{Z}_2 \to \widetilde{Z}_1 f \bar{f}$ decays (where f denotes SM fermions). As demonstrated in the previous section, LHC14 should probe gluinos with mass up to $m_{\tilde{g}} \sim 2$ TeV, assuming an integrated luminosity of ~ 1000 fb^{-1}. This means that LHC14 probes about half of the gluino mass range allowed by RNS.

This chapter addresses the detectability of the light higgsinos of RNS at the International Linear Collider (ILC), a proposed e^+e^- collider [97, 98] designed to operate at $\sqrt{s} \sim 0.25 - 1$ TeV, with an added capability of electron beam polarization. While such a machine is often touted as a Higgs boson factory due to the capacity to study the reaction $e^+e^- \to Zh$, for the case of models with light higgsinos that are required for naturalness, the ILC would also become a higgsino factory and a SUSY discovery machine [59].

Early pioneering studies of sparticle production at linear colliders were performed by the Japan Linear Collider group on mixed higgsino-wino type of chargino pair production where mass gaps were around 50 GeV [99]. Additional studies incorporating cascade decays were performed in Ref. [100], and in Ref. [101, 102] chargino pair production in the hyperbolic branch/focus point region [10, 103] was examined also with ~ 40 GeV mass gaps. Very recent studies include those in Ref. [104].

Recently, studies of higgsino pair production with mass gaps of order 1 GeV have been performed [105]. In these studies, use is made of initial state photon radiation and exclusive one-or-two particle hadronic decays of the charginos which have large branching fractions because the Q-value is limited at the GeV-level. These studies were relevant for string-motivated high-scale gauge-mediation models where the very large gaugino masses lead to large values of $\Delta_{EW} \sim 275$ [106]. The current discussion examines the case of models with $\Delta_{EW} \sim 10 - 30$ where mass gaps of 10-20 GeV

are typical, and for which the techniques of Ref. [105] are not needed.

Section 5.2 presents two RNS benchmark models labeled as ILC1 and ILC2. In Sec. 5.3, sparticle production and decay for the two RNS benchmark models at a higgsino factory is discussed. In Sec. 5.4, some details of the signal and background event generation calculations are presented. Finally, Sec. 5.5 and Sec. 5.6 discuss how ILC acts as a natural SUSY discovery machine for light higgsino pair production and show how it can make precision measurements of the associated sparticle masses and mass gaps.

5.1 Simulation of Events at an e^+e^- collider

A linear collider offers several advantages over hadron colliders, such as:

- the energy is no longer limited to the colliding partons, essentially all of the electron and positron energy goes into the hard scattering subprocess.
- such a collider allows for a polarized electron beam. These beams are valuable in separating signal from background and distinguishing similar signals.
- the energy is tunable, allowing experimentalists to tune into a specific process.
- the events are far cleaner than hadron collider events.

As mentioned in the footnote of Sec. 4.1, simulation at an e^+e^- collider follows a similar process as a hadron collider. For these types of collisions there are electron PDFs which describe bremstrahlung [107] and beamstrahlung [108] effects. These PDFs are described in [102]. Bremstrahlung allows for initial state photons which have the capacity to affect the background and signals, while beamstrahlung describes the beam-beam interactions which can result in energy loss and similar effects on the background and signal.

The polarization dependence can be incorporated directly into the cross section calculations. Figure 29 illustrates these effects for several processes. The degree of

polarization can be quantified as

$$P_{\rm L}(e^-) = f_{\rm L} - f_{\rm R}, \qquad \text{with} \tag{5.1}$$

$$f_{\rm L} = \frac{n_{\rm L}}{n_{\rm L}+n_{\rm R}} = \frac{1+P_{\rm L}}{2} \tag{5.2}$$

$$f_{\rm R} = \frac{n_{\rm R}}{n_{\rm L}+n_{\rm R}} = \frac{1-P_{\rm L}}{2} \tag{5.3}$$

where $n_{\rm L,R}$ is the number of left (right) polarized electrons in the beam, and $f_{\rm L,R}$ is the corresponding fraction.

5.2 Two RNS benchmark points

Two benchmark points were selected for study of light higgsinos in RNS models. To generate spectra for models with low Δ_{EW}, the Isasugra spectrum generator [54] from Isajet 7.84 [53] was used. Point ILC1 is similar to benchmark RNS2 of Ref. [47], except a lower $\mu = 115$ GeV value has been selected to yield a spectrum of light higgsinos which would already be accessible at ILC250 (ILC with $\sqrt{s} = 250$ GeV). The mass gaps for ILC1 are $m_{\widetilde{W}_1} - m_{\widetilde{Z}_1} = 14.6$ GeV and $m_{\widetilde{Z}_2} - m_{\widetilde{Z}_1} = 21.3$ GeV. While safe from LHC8 bounds, gluino and also wino production will lead to observable signals at LHC14 [69].

Also examined is the much more challenging case of benchmark ILC2 which will likely be beyond the reach of LHC14. This point is chosen from the RNS model-line with $\mu = 150$ GeV introduced in the previous chapter, with $m_{1/2}$ adjusted to obtain as small a mass gap as possible, consistent with $\Delta_{\rm EW}^{-1}$ of no more than 3%. For this challenging case, the mass gaps are rather small, with $m_{\widetilde{W}_1} - m_{\widetilde{Z}_1} = 10.2$ GeV and $m_{\widetilde{Z}_2} - m_{\widetilde{Z}_1} = 9.7$ GeV. This point is not accessible to ILC250, and so examines the feasibility of detection at a centre-of-mass energy just below the top pair threshold.

Within the RNS framework, $m_{\widetilde{Z}_2} - m_{\widetilde{Z}_1} = 10$ GeV is close to the minimum of the mass gap if one requires that $\Delta_{\rm EW}^{-1} > 3\%$. This can be seen from Fig. 27

where the neutralino mass gap is shown in the $m_{1/2} - \mu$ plane, with the other NUHM2 parameters fixed at the same values as for the ILC2 case. From the figure it is seen that the mass gap ranges from about 10 GeV (for large $m_{1/2}$, where the Δ_{EW} contours become vertical because the top squarks become too heavy) to over 100 GeV in the region where the gaugino and higgsino states are strongly mixed.

For these large mass gaps, LHC experiments should be awash in clean multilepton signals from electroweak-ino production, including signals from $\widetilde{W}_2$ and $\widetilde{Z}_4$ events. The concern here is the difficult region with a small mass gaps $m_{\widetilde{Z}_2} - m_{\widetilde{Z}_1}$ and $m_{\widetilde{W}_1} - m_{\widetilde{Z}_1}$ where there may well be no detectable signals even at LHC14. To the extent that the difficulty of extracting ILC SUSY signals (without using kinematic properties particular to exclusive chargino decays [105]) increases with decreasing mass gap, the ILC2 point represents nearly the most challenging case that may be encountered in the examination of linear colliders as a definitive probe of naturalness.

Listed at the bottom of Table 8 are the neutralino relic density, some B-decay branching fractions and WIMP detection rates along with the value of Δ_{EW}. WIMP detection sensitivities should be multiplied by a factor $\xi \equiv \Omega_{\widetilde{Z}_1} h^2/0.12$ since the higgsino-like WIMPs could make up only a fraction of the local DM density, while *e.g.* axions might make up the remainder [109]. This will be investigated in the next chapter.

5.3 Sparticle production and decay

5.3.1 Sparticle production

Shown in Fig. 28, are sparticle and Higgs boson production rates for unpolarized beams at the ILC versus $\sqrt{s}$ for the ILC1 benchmark point. Rates were computed at leading order, with leading order spectra, using formulae from Ref. [110]. Also shown for comparison is the rate for muon pair production. Around $\sqrt{s} \sim 220 - 230$ GeV, the threshold for production of Zh, $\widetilde{W}_1^{\pm}\widetilde{W}_1^{\mp}$ and $\widetilde{Z}_1\widetilde{Z}_2$ is crossed so that

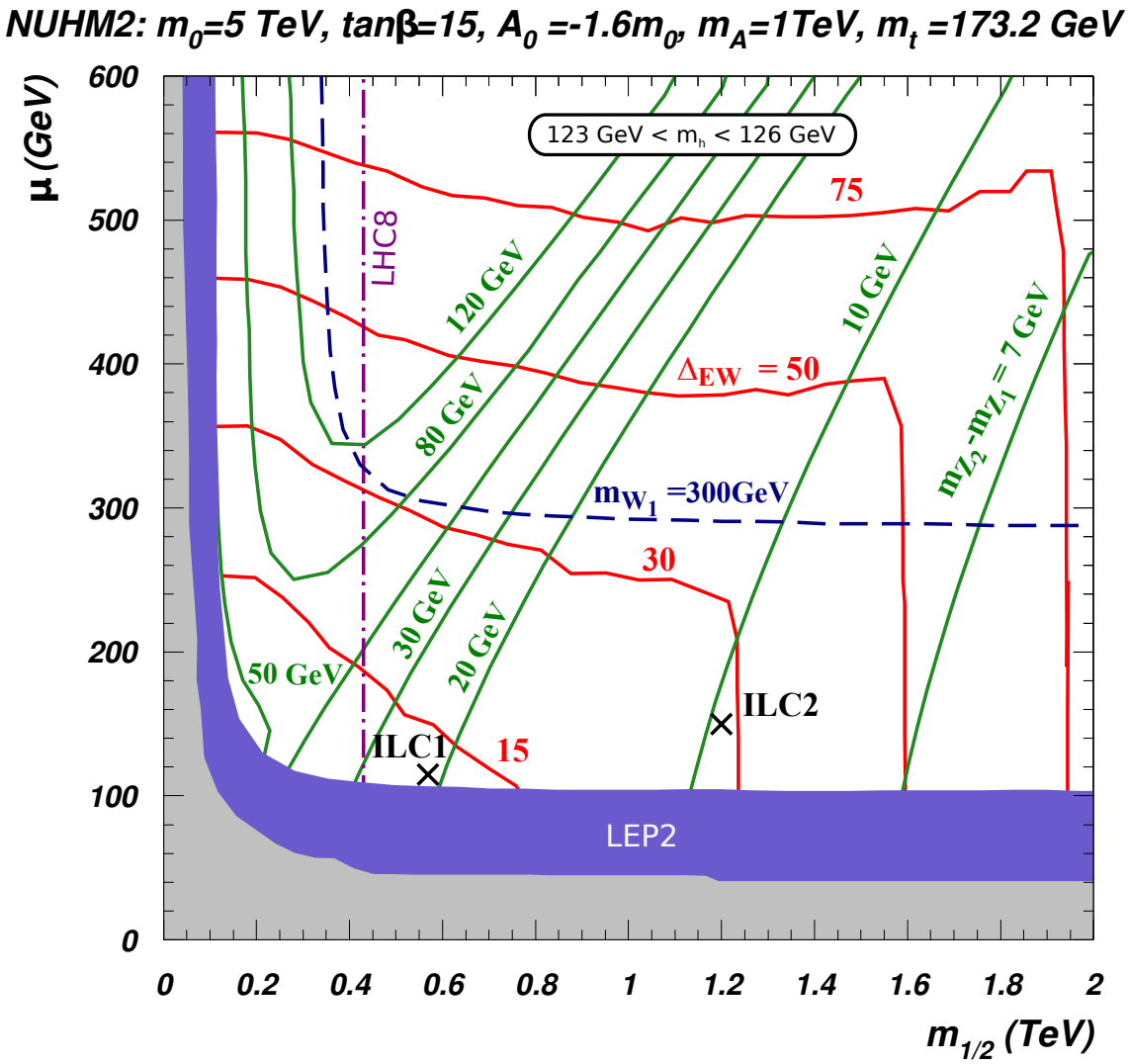


Figure 27: Contours of the mass gap (green curves) $m_{\widetilde{Z}_2} - m_{\widetilde{Z}_1}$ in the $m_{1/2} - \mu$ mass plane of the NUHM2 model for $m_0 = 5$ TeV, $A_0 = -1.6m_0$, $\tan\beta = 15$ and $m_A = 1$ TeV. The red curves show contours of Δ_{EW}. The blue (gray) shaded regions are excluded by the absence of a chargino signal at LEP2 (LEP1). The region to the left of the dot-dashed line is excluded by the LHC8 limit $m_{\tilde{g}} > 1.2$ TeV, obtained assuming squarks are very heavy. The dashed line is where $m_{\widetilde{W}_1} = 300$ GeV. The crosses denote μ and $m_{1/2}$ values for ILC1 and ILC2 benchmark points. Note that the other parameters for ILC1 differ from those in the figure, but the mass difference is insensitive to these.

parameter	ILC1	ILC2
m_0	7025.0	5000
$m_{1/2}$	568.3	1200
A_0	-11426.6	-8000
$\tan\beta$	10	15
μ	115	150
m_A	1000	1000
$m_{\tilde{g}}$	1563.5	2832.6
$m_{\tilde{u}_L}$	7021.3	5440.4
$m_{\tilde{u}_R}$	7254.2	5565.6
$m_{\tilde{e}_R}$	6758.6	4817.1
$m_{\tilde{t}_1}$	1893.3	1774.3
$m_{\tilde{t}_2}$	4919.4	3877.9
$m_{\tilde{b}_1}$	4959.2	3902.8
$m_{\tilde{b}_2}$	6893.3	5204.5
$m_{\tilde{\tau}_1}$	6656.6	4652.3
$m_{\tilde{\tau}_2}$	7103.1	5072.5
$m_{\tilde{\nu}_\tau}$	7114.0	5078.7
$m_{\widetilde{W}_2}$	513.0	1017.5
$m_{\widetilde{W}_1}$	117.3	158.3
$m_{\widetilde{Z}_4}$	524.2	1031.1
$m_{\widetilde{Z}_3}$	267.0	538.7
$m_{\widetilde{Z}_2}$	124.0	157.8
$m_{\widetilde{Z}_1}$	102.7	148.1
m_h	125.3	125.4
$\Omega^{std}_{\widetilde{Z}_1}h^2$	0.009	0.007
$BF(b\to s\gamma)\times 10^4$	3.3	3.3
$BF(B_s\to\mu^+\mu^-)\times 10^9$	3.8	3.9
$\sigma^{SI}(\widetilde{Z}_1 p)$ (pb)	1.3×10^{-8}	2.9×10^{-9}
Δ_{EW}	13.9	28.5

Table 8: NUHM2 input parameters and masses in GeV units for the two RNS benchmark points introduced in the text. Here $m_t = 173.2$ GeV.

production rates rise rapidly. Whereas one might expect ILC at these energies to be a Higgs boson factory, ILC would also be a higgsino factory, where the higgsino pair production rates exceed Zh production by factors of 5-10. While the higgsino decay debris may be too soft to be picked out above SM backgrounds at LHC, the clean environment of a linear e^+e^- collider allows for straightforward discovery, as discussed in Sec. 5.5 and 5.6. Thus, although RNS might well elude LHC searches, it cannot elude searches at ILC provided that $\sqrt{s} > 2m(higgsino)$.

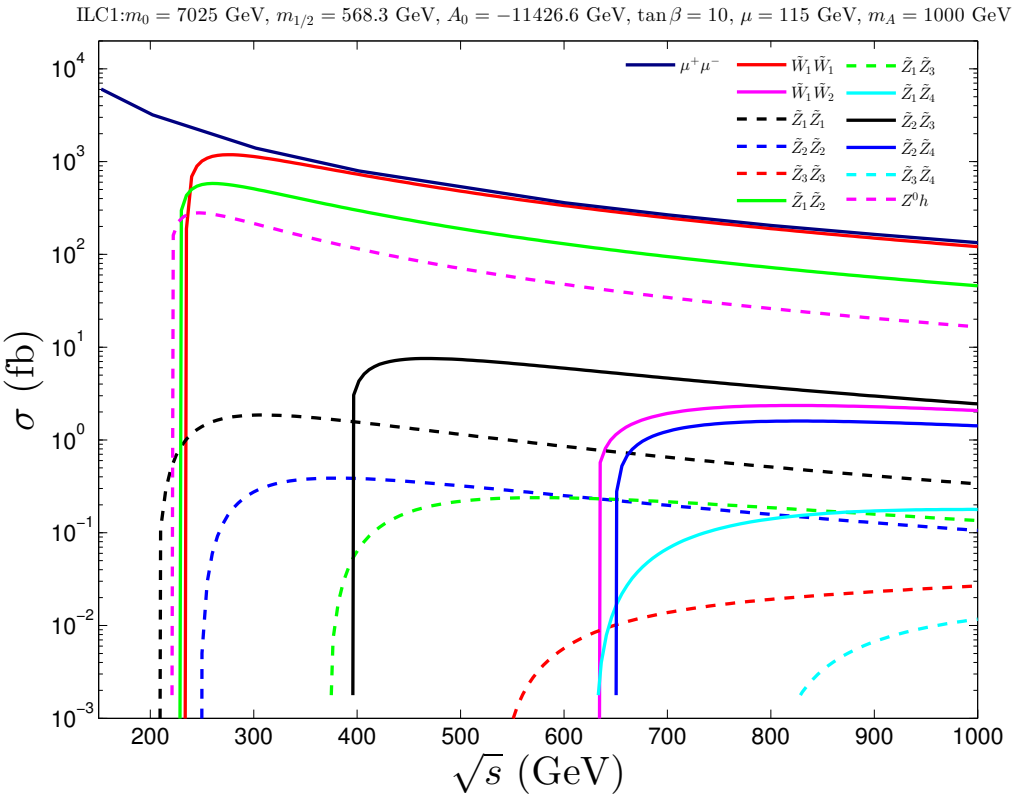


Figure 28: Sparticle production cross sections vs. $\sqrt{s}$ for unpolarized beams at an e^+e^- collider for the ILC1 benchmark point listed in Table 8.

While the reactions $e^+e^- \to \widetilde{W}_1^+\widetilde{W}_1^-$ and $e^+e^- \to \widetilde{Z}_1\widetilde{Z}_2$ will be the first sparticle production processes accessed at ILC250, the discovery prospects do not end there. As $\sqrt{s}$ is increased beyond $2m(higgsino)$, further thresholds will be passed, including those for $\widetilde{Z}_2\widetilde{Z}_3$, $\widetilde{W}_1\widetilde{W}_2$ and $\widetilde{Z}_2\widetilde{Z}_4$ production. These occur at somewhat lower but

still measureable rates. Even reactions with much lower production rates – such as $\widetilde{Z}_2\widetilde{Z}_2$, $\widetilde{Z}_1\widetilde{Z}_3$, $\widetilde{Z}_3\widetilde{Z}_3$ and $\widetilde{Z}_3\widetilde{Z}_4$ – might ultimately be detectable, depending on the machine energy and integrated luminosity that is ultimately attained.

Shown in Fig. 29, are the $\widetilde{W}_1^+\widetilde{W}_1^-$ and $\widetilde{Z}_1\widetilde{Z}_2$ production rates for the ILC1 benchmark case at $\sqrt{s} = 250$ GeV, but as a function of the electron beam polarization $P_L(e^-)$. Whereas $\widetilde{W}_1^+\widetilde{W}_1^-$ production has the largest rate for unpolarized beams ($P_L(e^-) = 0$), for the case of right polarized electron beam, $\sigma(\widetilde{W}_1^+\widetilde{W}_1^-)$ diminishes by a factor of about 4 and instead $\sigma(\widetilde{Z}_1\widetilde{Z}_2)$, which is much less sensitive to beam polarization, is dominant. The comparable rates (within an order of magnitude) for both both chargino and neutralino pair production (solid curves), together with the relatively mild polarization is characteristic of the production of higgsino-like charginos and neutralinos. For wino-like gauginos in the kinematically accessible range, chargino production would occur at a high rate, but neutralino pair production would be strongly suppressed because $SU(2)_L \times U(1)_Y$ gauge symmetry forbids couplings of the Z and γ to both binos and (neutral) winos. This can be seen in the dashed curve in Fig. 29 which shows the cross section for $\widetilde{W}_1\widetilde{W}_1$ production for the ILC1 model point except that $m_{1/2}$ and μ are now chosen so that the weak scale values of M_2 and μ are essentially exchanged. In this case, the masses of the wino-like $\widetilde{W}_1$ and $\widetilde{Z}_2$ is about the same as for the higgsinos of the ILC1 point. The neutralino-pair production cross sections for this wino-like case are below 0.1 fb and do not show up in this frame. This observation will be important in Sec. 5.5 where the analysis is described. The polarization dependence of the chargino pair production cross section provides an independent handle that may enable us to argue the higgsino-like nature of the charginos of the ILC1 point. For a right-handed electron beam the amplitude for charged wino pair production is suppressed by a factor of M_W^2/s relative to that for charged higgsino pair production, accounting for the strong drop of the dashed curve at $P_L(e^-) = -1$.

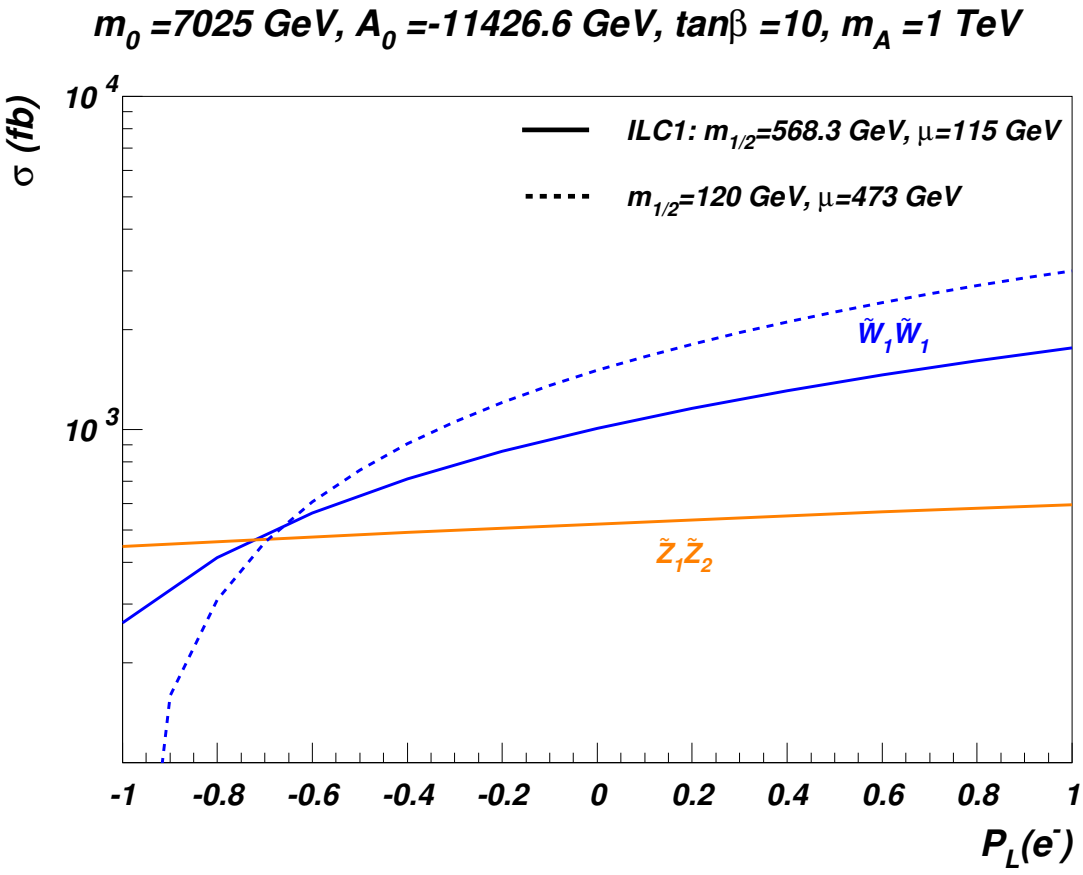


Figure 29: Sparticle production cross sections vs. $P_L(e^-)$ at an e^+e^- collider for the ILC1 benchmark point with $\sqrt{s} = 250$ GeV. The positrons are taken to be unpolarized. For comparison, shown is a point with a wino-like chargino of similar mass. For the wino-like case with $m_{1/2} = 120$ GeV, then the $\sigma(e^+e^- \to \widetilde{Z}_1\widetilde{Z}_2) \sim 0.1$ fb, while $\sigma(\widetilde{Z}_2\widetilde{Z}_2)$ is even smaller, and so is far below the cross section values shown.

5.3.2 Higgsino decays

Since the inter-higgsino mass gaps are so small, for the case of RNS one expects the following three-body decays to be dominant:

$$\widetilde{W}_1^- \rightarrow \widetilde{Z}_1 f \bar{f}' \,, \tag{5.4}$$

$$\widetilde{Z}_2 \rightarrow \widetilde{Z}_1 f \bar{f} \,, \tag{5.5}$$

where the f stand for SM fermions. Despite the larger phase space suppression for the three body decays, the branching fraction for the loop decay $\widetilde{Z}_2 \rightarrow \widetilde{Z}_1 \gamma$ is still small because of the large $Z\widetilde{Z}_1\widetilde{Z}_2$ coupling [111]. Moreover, squark and slepton masses are expected very large within the RNS framework, and the $\widetilde{W}_1$ and $\widetilde{Z}_2$ three-body decay amplitudes are dominated by W^* and Z^* exchange, respectively. The branching fractions into specific modes will thus closely follow the corresponding W and Z decay branching fractions, *i.e.* one obtains $B(\widetilde{W}_1^- \rightarrow \widetilde{Z}_1 e^- \bar{\nu}_e) \simeq 11\%$, $B(\widetilde{Z}_2 \rightarrow e^+ e^- \widetilde{Z}_1) \simeq 3\%$, *etc.*.

5.4 SUSY event generation

Within the RNS framework, higgsino pair production at the ILC will be signalled by events with low visible energy from the relatively soft daughter leptons and jets from $\widetilde{W}_1$ and $\widetilde{Z}_2$ decays, and modest $E_T^{\rm miss}$. One needs, therefore, to pay particular attention to SM sources of low visible energy events. Since the bulk of $2 \rightarrow 2$ events lead to large visible energy, the most important backgrounds come from two photon processes, $e^+e^- \rightarrow e^+e^- f\bar{f}$, where the energetic final state electron and positron are lost down the beam-pipe, and the visible energy in the detector arises only from f and $\bar{f}$.

ISAJET v7.84 was used for the SUSY event simulation as well as simulation of

$2 \to 2$ and $\gamma\gamma$-induced SM backgrounds. The $2 \to 2$ SM background sources include

$$e^+e^- \to f\bar{f},\ W^+W^- \ \text{ and } \ Z^0Z^0\ , \tag{5.6}$$

while $\gamma\gamma$ processes include,

$$\gamma\gamma \to \tau^+\tau^-,\ \ c\bar{c} \ \text{ and } \ b\bar{b}. \tag{5.7}$$

The reaction $e^+e^- \to Zh$ is included in the signal sample, but plays no role here.

The Isajet toy calorimeter was used, covering $-4 < \eta < 4$ with cell size $\Delta\eta \times \Delta\phi = 0.05 \times 0.05$. Energy resolution for electromagnetic and hadronic depositions is taken to be $\Delta E_{em}/E_{em} = 0.15/\sqrt{E_{em}} \oplus 1\%$ and $\Delta E_h/E_h = 0.5/\sqrt{E_h}/E_h \oplus 2\%$, respectively (where $\oplus$ denotes addition in quadrature). Jets are found using fixed cones of size $R = \sqrt{\Delta\eta^2 + \Delta\phi^2} = 0.6$ using the ISAJET routine GETJET (modified for clustering on energy rather than transverse energy). Clusters with $E > 5$ GeV and $|\eta(\text{jet})| < 2.5$ are labeled as jets. Muons and electrons are classified as isolated if they have $E > 5$ GeV, $|\eta(\ell)| < 2.5$, and the visible activity within a cone of $R = 0.5$ about the lepton direction is less than $min(\frac{E_\ell}{10},\ 1\ \text{GeV})$.

The production reactions are run using electron PDFs which include a convolution of bremsstrahlung [107] and beamstrahlung [108] contributions. For $\sqrt{s} = 250$ GeV, a beamstrahlung parameter $\Upsilon = 0.02$ was used and for $\sqrt{s} = 340$ GeV, $\Upsilon = 0.03$ was used. For both cases, the beam bunch length $\sigma_z = 0.3$ mm [112] was used.

For processes with low visible energy, the two-photon processes $\gamma\gamma \to f\bar{f}$ can be the most relevant. These processes also give rise to E_T^{miss} when the decay products of f include neutrinos. This analysis therefore includes only

- $\gamma\gamma \to \tau^+\tau^-,\ c\bar{c}$ and $b\bar{b}$

contributions from Isajet using a photon PDF which again includes a beam/bremsstrahlung convolution [102, 113].

5.5 Benchmark ILC1 at $\sqrt{s} = 250$ GeV

This section begins by discussing higgsino pair production for the ILC1 benchmark point with $\sqrt{s} = 250$ GeV, the nominal turn-on energy of the ILC. Once threshold for pair production is passed, then the two higgsino pair production reactions occurring at the highest rates are

- $e^+e^- \to \widetilde{W}_1^+\widetilde{W}_1^- \to (f\bar{f}'\widetilde{Z}_1) + (F\bar{F}'\widetilde{Z}_1)$ and
- $e^+e^- \to \widetilde{Z}_1\widetilde{Z}_2 \to \widetilde{Z}_1 + (f\bar{f}\widetilde{Z}_1)$

where f and F are SM fermions. For models where $|\mu| \ll M_{1,2}$, the two lightest neutralinos are well approximated by $\frac{(\tilde{h}_u \pm \tilde{h}_d)}{\sqrt{2}}$, and the coupling of Z to $\widetilde{Z}_1\widetilde{Z}_1$ and $\widetilde{Z}_2\widetilde{Z}_2$ pairs is dynamically suppressed [24]. Thus, though the phase space for $\widetilde{Z}_2\widetilde{Z}_2$ production is qualitatively similar to that for $\widetilde{Z}_1\widetilde{Z}_2$ production, $\sigma(\widetilde{Z}_2\widetilde{Z}_2)$ is much smaller in the RNS framework: see Fig. 28.

Since $m_{\widetilde{Z}_1}$ is only slightly smaller than $m_{\widetilde{W}_1,\widetilde{Z}_2}$, most of the collision energy ends up in the rest mass $2m_{\widetilde{Z}_1}$ of the LSPs, and the visible final state fermions are relatively soft. To illustrate this, shown in Fig. 30 is the visible energy distribution expected at ILC250 for benchmark ILC1. From the figure, one sees the bulk of SM background from e^+e^- annihilation processes (green curve) in (5.6) peaks around $E_{vis} \sim 250$ GeV, with some spillover to higher values due to detector energy mismeasurement. A continuous E_{vis} tail occurs at lower values due to production of WW, ZZ, $b\bar{b}$ *etc.* where substantial energy is lost due to decays to neutrinos. There are also two small bumps at $E_{vis} \sim 140$ GeV and 250 GeV arising from Zh production (blue curves). The 140 GeV bump occurs due to $e^+e^- \to Zh \to (\nu\bar{\nu})+(b\bar{b})$. The SUSY signal distribution is depicted by the bounded (red) histogram

with $E_{vis} \sim 0 - 40$ GeV is already well-separated from the $2 \to 2$ SM backgrounds. However, as anticipated, backgrounds from the $2 \to 4$ processes, $\gamma\gamma \to c\bar{c}$, $b\bar{b}$ and $\tau\bar{\tau}$, shown as the black histogram overwhelm the signal by a factor of $\sim 100 - 1000$.

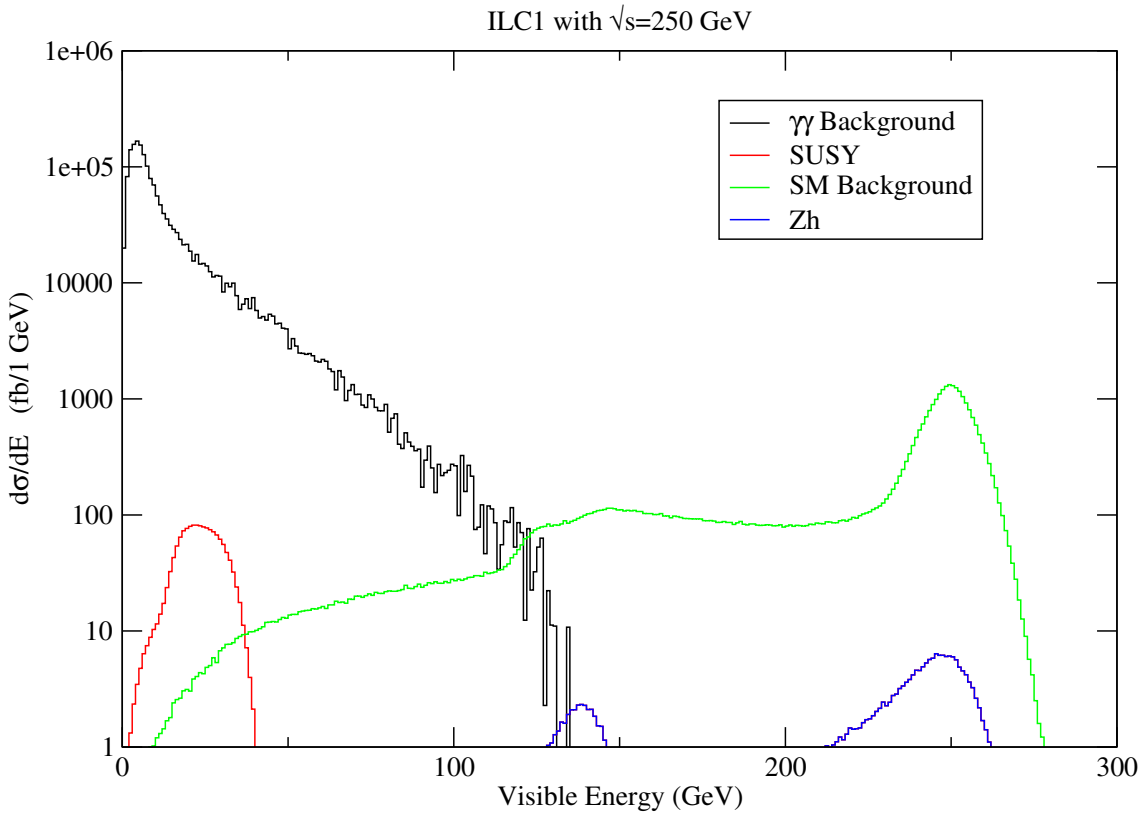


Figure 30: Distribution in visible energy measured in e^+e^- events at $\sqrt{s} = 250$ GeV for ILC1 signal and SM backgrounds from e^+e^- and $\gamma\gamma$ collisions. Beamstrahlung parameters are $\Upsilon = 0.02$ and $\sigma_z = 0.3$ mm.

To select signal events, the first requirement is:

- 20 GeV $< E_{vis} <$ 50 GeV.

The $\gamma\gamma$ background yields mainly soft visible energy events with a tail extending to higher values. To differentiate signal from this background, plotted in Fig. 31 is the missing transverse energy distribution $d\sigma/dE_T^{\rm miss}$ after the visible energy cut. The $\gamma\gamma$ background falls very rapidly since $E_T^{\rm miss}$ occurs mainly due to neutrinos

from the decays of the relatively light c, b and τ, and the signal emerges from $\gamma\gamma$ background if one requires $E_T^{\rm miss} > 10$ GeV. The bulge of events with low E_{vis} but modest $E_T^{\rm miss}$ would herald the discovery of new physics. This also explains why $\gamma\gamma \to f\bar{f}$ processes with $f = e, \mu, u, d, s$ were not included in the analysis. These yield back-to-back events in the transverse plane, with essentially no $E_T^{\rm miss}$, and are efficiently eliminated by a $E_T^{\rm miss}$ cut. Thus, for the new physics event sample, it is also required that

- $E_T^{\rm miss} > 10$ GeV.

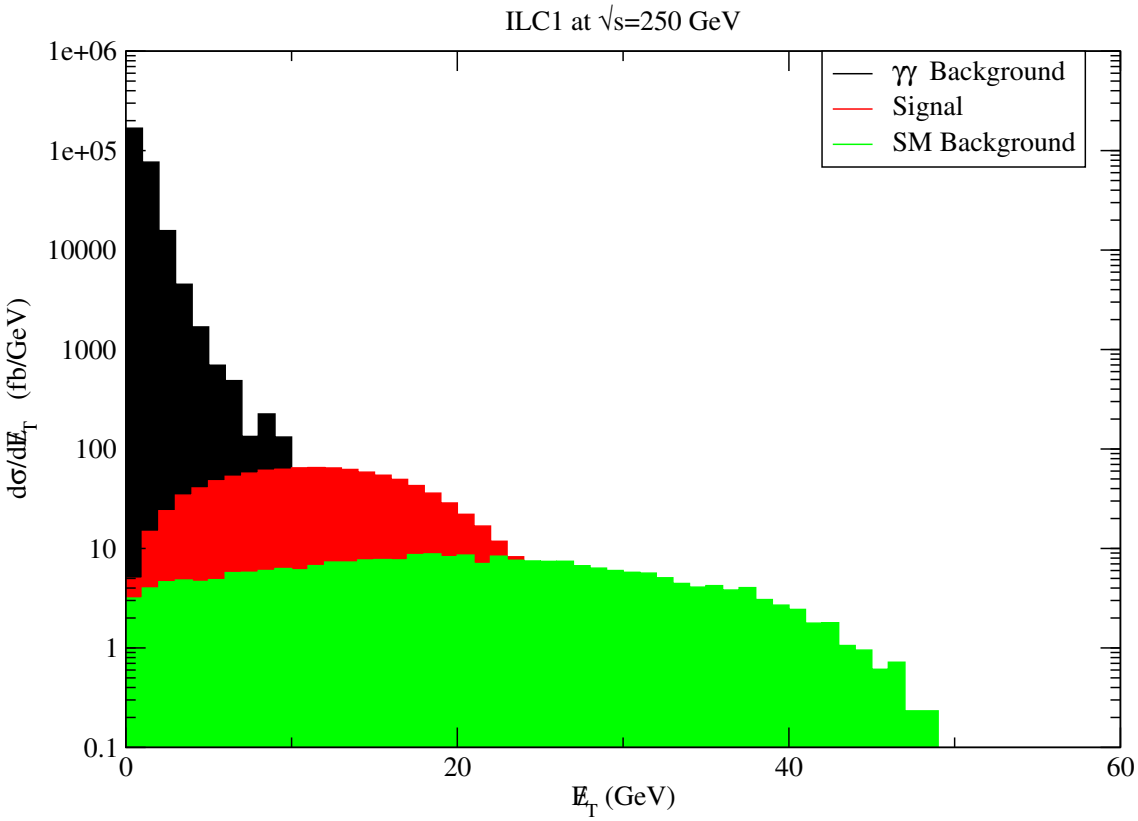


Figure 31: Distribution of missing transverse energy from e^+e^- collisions at $\sqrt{s} =$ 250 GeV for ILC1 signal along with SM background from e^+e^- and $\gamma\gamma$ collisions. It is required that 20 GeV$< E_{vis} <$ 50 GeV. Beamstrahlung parameters are $\Upsilon = 0.02$ and $\sigma_z = 0.3$ mm.

To understand the expected event topologies, the multiplicity of isolated leptons and identified jets is examined. These distributions are shown in Fig. 32. One

sees that the most lucrative signal channels from the perspective of the signal to background ratio appears to be the $n(\ell) = 0$ and $n(jet) = 1 - 3$ bins to which neutralino and chargino production can contribute. To cleanly separate chargino and neutralino contributions so that each particle can be studied in detail, it is also useful to examine other channels.

Before turning to this, note that the observation of an excess above SM in the multi-jet plus multi-lepton channels would suggest the production of charginos and neutralinos. The small energy release in these events would point to a small mass gap between the parent particles and the undetected LSP. In the simplest models with gaugino mass unification, this would indicate the production of higgsino-like states, with $|\mu| \ll m_{1/2}$ where $\widetilde{W}_1$, $\widetilde{Z}_2$ and $\widetilde{Z}_1$ are roughly degenerate, and the bino and winos are substantially heavier. However, it is also possible that such events may arise from wino pair production in models with heavy higgsinos, and a bino only slightly lighter than the wino-states. It should, however, be possible to distinguish between these possibilities since, as mentioned in the discussion of Fig. 29, with unpolarized beams neutralino production is smaller than 0.1 fb (*i.e.* three orders of magnitide below expectations for higgsino-like neutralinos) in the latter case. Moreover, the chargino signal from the production of wino-like charginos will reduce much more sharply for right-handed electron beams than for higgsino-like charginos. It should thus be possible to unambiguously conclude that the signal is from higgsino-like, and not gaugino-like super-partners.

With this in mind, the goal is to find strategies that will help obtain essentially pure samples of chargino and of neutralino events for the ILC1 point under examination.

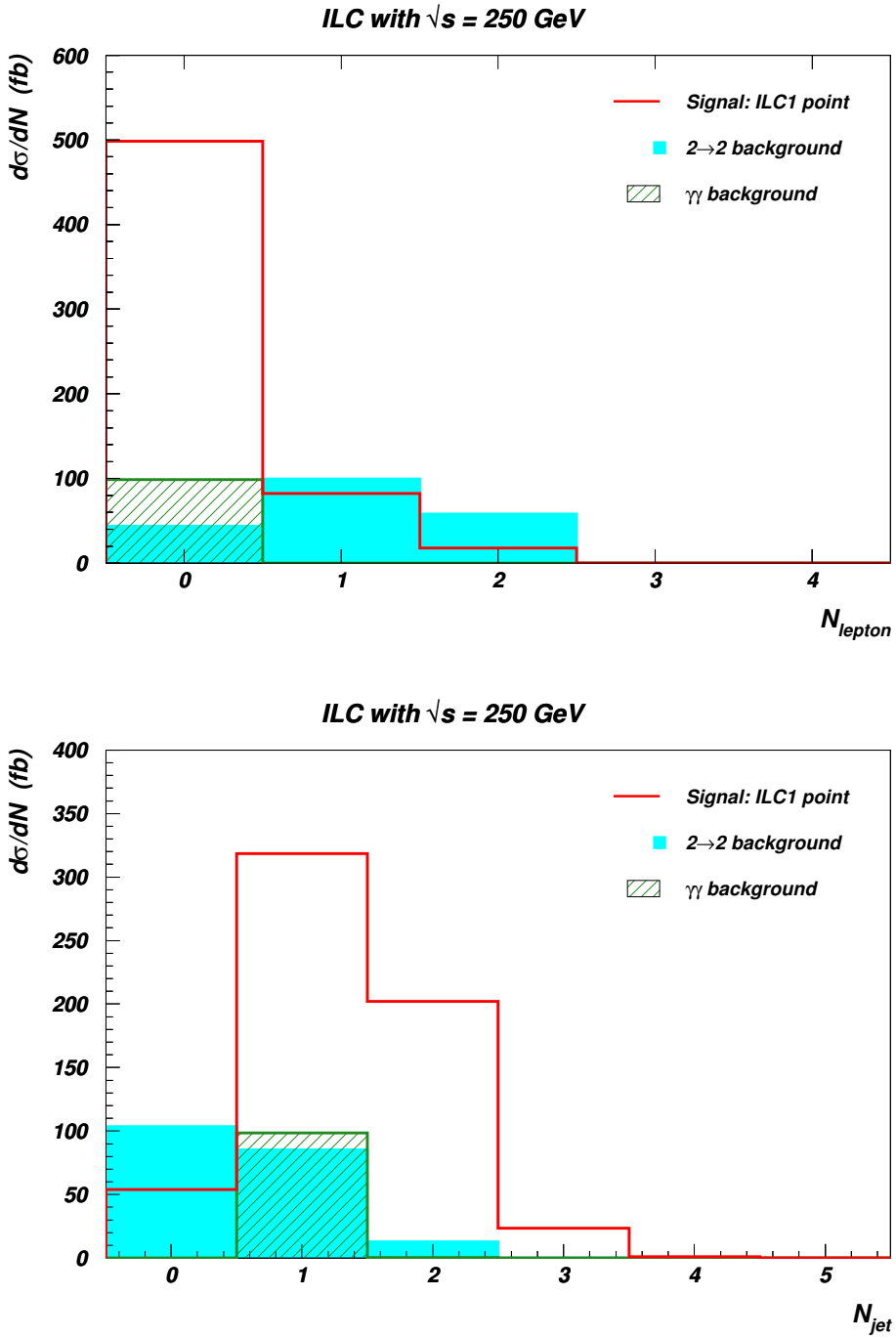


Figure 32: Distribution of *a*) isolated lepton multiplicity and *b*) jet multiplicity from e^+e^- collisions at $\sqrt{s} = 250$ GeV for higgsino signals from the ILC1 case study along with corresponding SM backgrounds from e^+e^- and $\gamma\gamma$ collisions. It is required that 20 GeV$< E_{vis} <$ 50 GeV and $E_T^{\rm miss} >$ 10 GeV. Beamstrahlung parameters are $\Upsilon = 0.02$ and $\sigma_z = 0.3$ mm.

5.5.1 Chargino pair production for ILC1

To select out a nearly pure sample of chargino pair events where the jets all arise from the same chargino, first selected are events with the E_{vis} and $E_T^{\rm miss}$ cuts introduced above, but also require

- $n(\ell) = 1$

and

- $n(jet) = 2$.

After these requirements, the signal cross section is 6.43 fb. Just one background event passes cuts, leading to $\sigma_{BG} \sim 0.018$ fb, *i.e.* there is a nearly pure sample of chargino pair events, where one chargino decays leptonically and the other decays hadronically.

A scatter plot of these selected events in the $E(jj)$ vs. $m(jj)$ plane is shown in Fig. 33. The $m(jj)$ distribution is expected to be bounded from above by $m_{\widetilde{W}_1} - m_{\widetilde{Z}_1} = 14.6$ GeV up to energy mis-measurement corrections; this cut-off is seen in Fig. 33, from which it is apparent the $m_{\widetilde{W}_1} - m_{\widetilde{Z}_1}$ mass gap is ~ 15 GeV.

The sparticle masses $m_{\widetilde{W}_1}$ and $m_{\widetilde{Z}_1}$ can be obtained from fits of the $E(jj)$ data distribution [99, 100, 101] to various expected theory distributions which vary depending on $m_{\widetilde{W}_1}$ and $m_{\widetilde{Z}_1}$. The lower endpoint of $E(jj)$ is determined largely by the $E(j) > 5$ GeV jet requirement but the upper endpoint is quite sensitive to $m_{\widetilde{W}_1}$ and $m_{\widetilde{Z}_1}$ values.

To assess the precision which can be attained, a synthetic "data" set is generated, assuming 100 fb^{-1} of integrated luminosity, along with expected statistical error bars. Also generated is a theory sample of distributions run over a large grid of μ and $m_{1/2}$ points (which yields a corresponding grid of $m_{\widetilde{W}_1}$ and $m_{\widetilde{Z}_1}$ points) where each theory sample is run with 10 times the statistics of data. This analysis ignores any sensitivity to other parameters, and implicitly assumes that one can distinguish

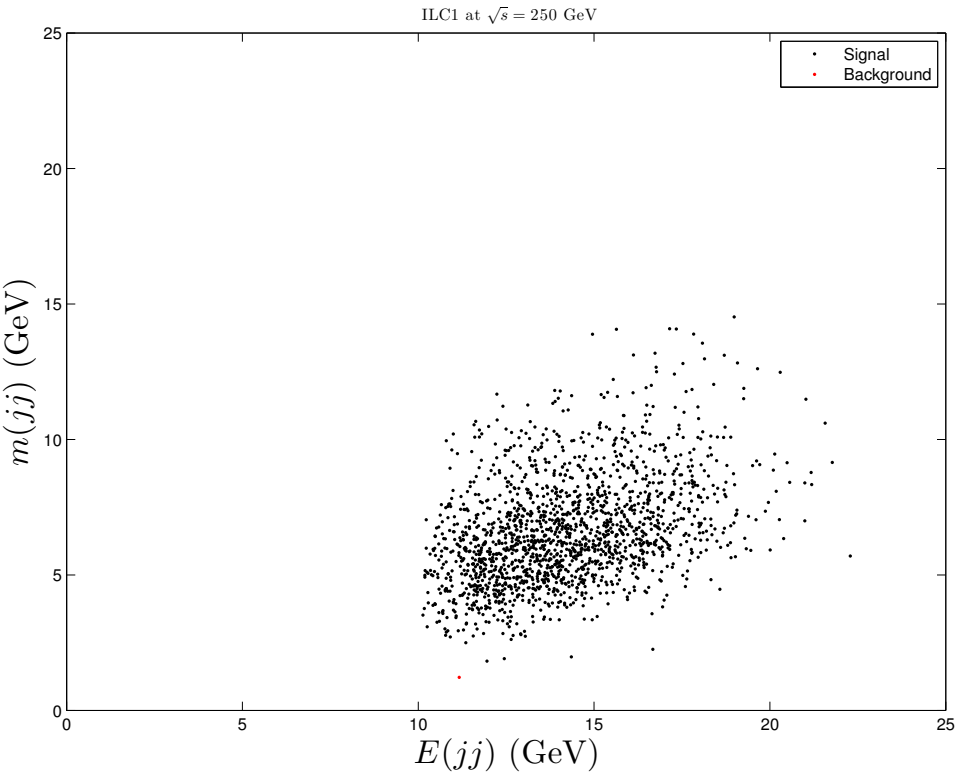


Figure 33: Scatter plot in the E_{jj} vs. $m(jj)$ plane for $1\ell + 2 - jets$ events from the ILC1 point in e^+e^- collisions at $\sqrt{s} = 250$ GeV. It is required that 20 GeV$<$ $E_{vis} < 50$ GeV and $MET > 10$ GeV. Beamstrahlung parameters $\Upsilon = 0.02$ and $\sigma_z = 0.3$ mm.

between higgsino- and wino-like chargino events (which should be possible as noted just before the start of Sec. 5.5.1). The $E(jj)$ "data" distribution (with 1 GeV bins) is then compared to these theory templates and one may obtain the values of χ^2 between the "data" and the theory. The normalization of theory curves is fixed to match "data" so that only the shape of the distribution is fitted. To obtain the χ^2, the appropriately weighted statistical errors for the theory and data sets are added in quadrature.

This procedure enables one to obtain a grid of $\Delta\chi^2 = \chi^2 - \chi^2_{min}$ values in the $m_{\widetilde{W}_1} - m_{\widetilde{Z}_1}$ plane. The reader should keep in mind that the theory calculation is also subject to statistical fluctuations that will be reflected in the distribution of $\Delta\chi^2$ values. To enable the reader to personally assess the reliability of the computation, shown in Fig. 34*a* are these $\Delta\chi^2$ values binned by $\Delta\chi^2 < 2.3$ (1σ CL), $\Delta\chi^2 < 4.6$ (90% CL) and $\Delta\chi^2 > 4.6$. Also shown are the corresponding 1σ and 90% CL error ellipses that were obtained as conservative fits to the $\Delta\chi^2$ data. From these error ellipses, the 2-3% mass measurements

- $m_{\widetilde{W}_1} = 117.8 \pm 2.8$ GeV (1σ),

and also,

- $m_{\widetilde{Z}_1} = 103.1 \pm 2.2$ GeV (1σ),

should be possible for the ILC1 point. The synthetic "data", together with statistical error bars corresponding to an integrated luminosity of 100 fb^{-1}, are shown in Fig. 34*b*) along with the best fit distribution shown as the solid curve.

Note that if instead the time is taken to perform various total cross section measurements around the higgsino pair threshold – which will require a much higher integrated luminosity investment at several $\sqrt{s}$ values [114] – even better precision on the masses may be expected.

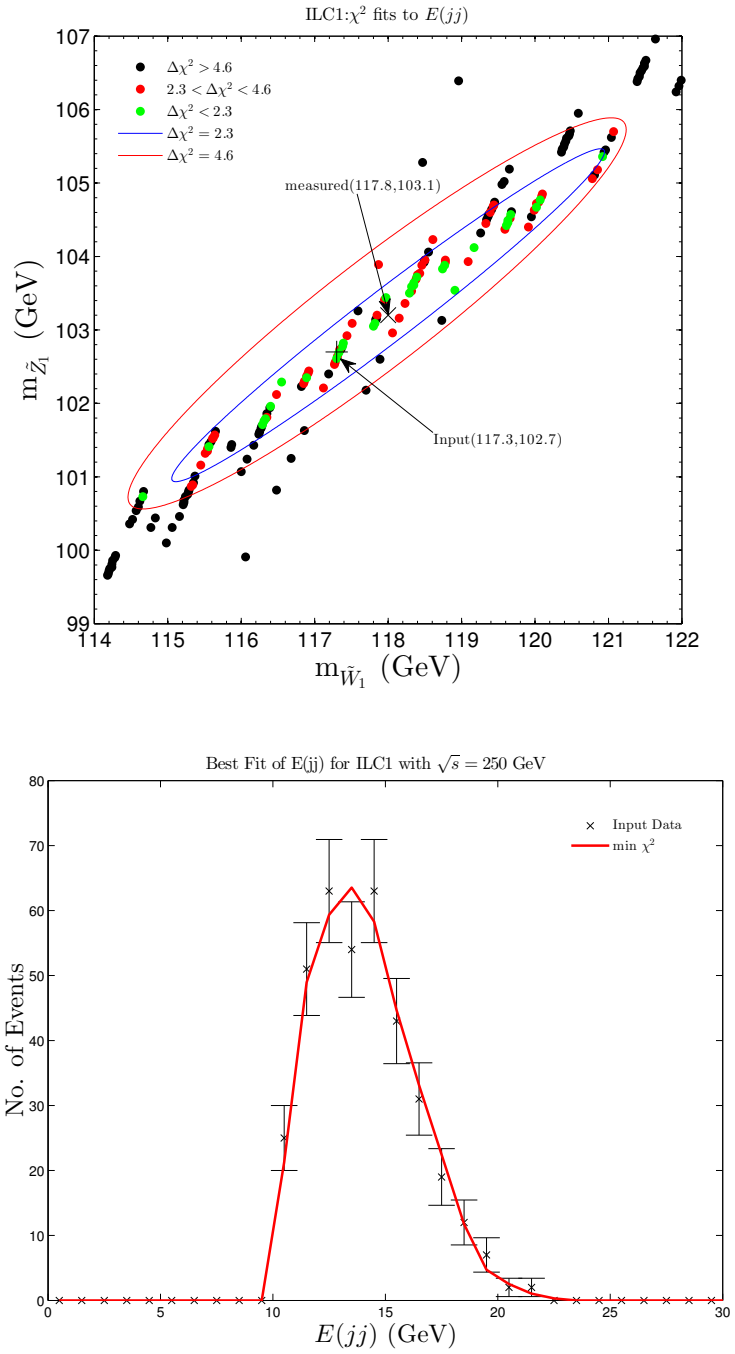


Figure 34: Shown *a*), are values of $\Delta\chi^2$ found from matching 100 fb^{-1} of ILC1 "data" to various "theory" distributions generated from a scan over μ *vs.* $m_{1/2}$ space. Each "theory" point is run with ten times the events contained in the "data" distribution. Also shown are fitted error ellipses corresponding to 1σ and 90% CL measurements. In *b*), is the distribution in $E(jj)$ from 100 fb^{-1} of "data" along with best fit distribution.

5.5.2 Neutralino pair production for ILC1

For the case of $\widetilde{Z}_1\widetilde{Z}_2$ pair production, events where $\widetilde{Z}_2 \to q\bar{q}\widetilde{Z}_1$ that yield an $n(\ell) = 0,\ n(j) = 2$ sample as well as events where $\widetilde{Z}_2 \to \ell^+\ell^-\widetilde{Z}_1$, for which $n(\ell) = 2$ and $n(j) = 0$ were examined. While one might expect the dijet sample to yield more events due to the large $\widetilde{Z}_2 \to \widetilde{Z}_1 q\bar{q}$ branching fraction, in fact one finds after cuts that the $\ell^+\ell^-$ sample is larger. This is because frequently the two possible quark jets merge to yield only a single resolvable jet given the jet finding algorithm, or else one of the possible jets becomes too soft or too forward to be identified.

For the opposite-sign/same flavor (OS/SF) dilepton signal that is focused on, a polarized electron beam with $P_L(e^-) = -0.9$ is used since this helps to reduce potential backgrounds from WW production, and also limits contamination from chargino production to around 10%. The signal is required to have:

- exactly 2 OS/SF isolated leptons with no jets,
- $E_{vis} < 35$ GeV,
- transverse plane angle between the two leptons $\Delta\phi(\ell^+\ell^-) < \pi/2$.

After these cuts, the $\gamma\gamma$ background is eliminated but some SM background – mainly WW production – remains. The $E(\ell^+\ell^-)$ distribution after these cuts is shown in Fig. 35. This leaves a OS/SF dilepton signal of 19.55 fb while SM background is 0.44 fb. The signal has a negligible contribution from chargino production.

With the clean sample of OS/SF dilepton signal events from essentially $\widetilde{Z}_1\widetilde{Z}_2$ production, next examined is the $m(\ell^+\ell^-)$ distribution for the ILC1 case. One expects that this distribution is kinematically bounded from above by the $m_{\widetilde{Z}_2} - m_{\widetilde{Z}_1}$ mass difference and relatively insensitive to the absolute masses of the particles. The theory templates generated with 10 times the statistics, as described in Sec. 5.5.1 were used to obtain a map of χ^2 vs. $m_{\widetilde{Z}_2} - m_{\widetilde{Z}_1}$, shown by the jagged (black) line in Fig. 36*a*. As before, the fit is to the shape, allowing the normalization to float.

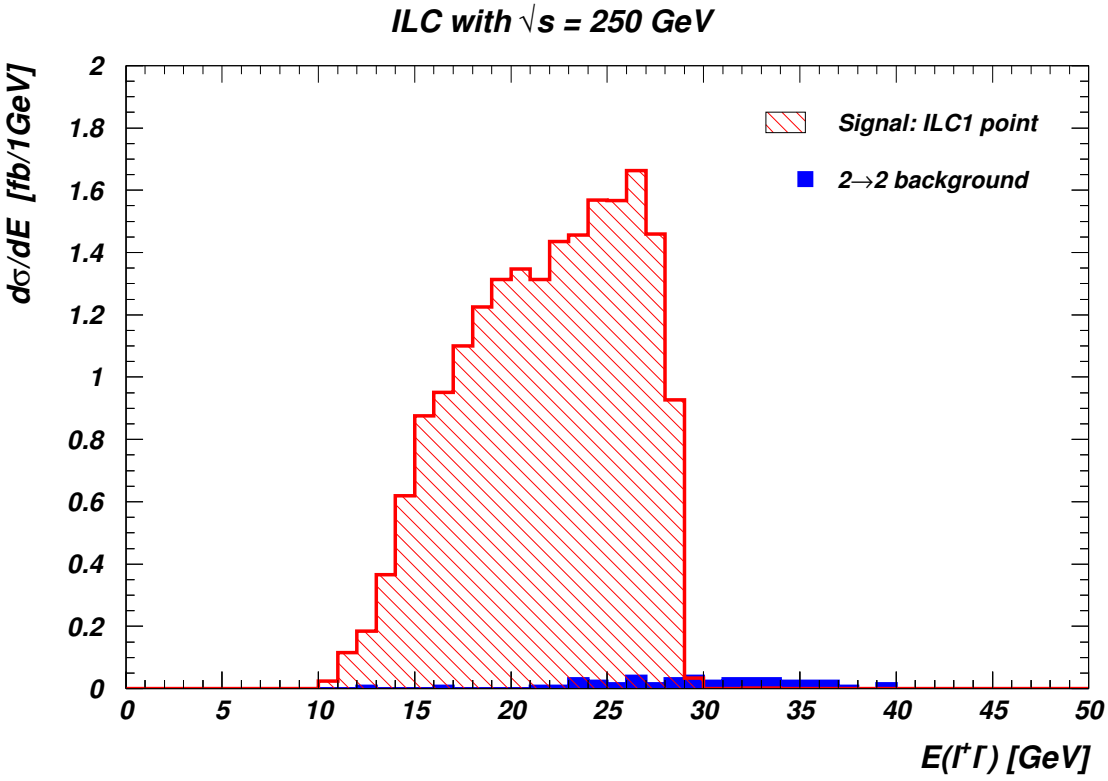


Figure 35: Distribution in $E(\ell^+\ell^-)$ from 100 fb^{-1} of "data" of OS/SF dilepton events with $P_L(e^-) = -0.9$ from the signal for the ILC1 case, and from SM background (which only comes from $2 \to 2$ processes), after the E_{vis} and $\Delta\phi(\ell\ell)$ cuts discussed in the text.

While statistical fluctuations do contribute to the jaggedness, it was checked that the points with the largest χ^2 values come from theory templates where the mass scale of the neutralinos is very different. Also shown in the figure is a parabolic fit to the values of χ^2. From this, one sees that the mass gap should be measureable at the percent level:

- $m_{\widetilde{Z}_2} - m_{\widetilde{Z}_1} = 21.0 \pm 0.2$ GeV (1σ).

The best fit line and the dilepton mass "data" used to obtain the fit are shown in the lower frame in the figure. The shape of this mass distribution is indicative of an opposite sign of the $\widetilde{Z}_1$ and $\widetilde{Z}_2$ mass eigenvalues [71], completely compatible with expectation [15] from the decay of a higgsino-like $\widetilde{Z}_2$ to a higgsino-like $\widetilde{Z}_1$.

Once the mass gap is known, it is possible to extract the neutralino mass value via a fit to the $E(\ell^+\ell^-)$ distribution because the energy of the daughter leptons (but not their invariant mass) depends on the boost of the parent $\widetilde{Z}_2$. The same procedure described above was used to fit the 100 fb^{-1} OS/SF dilepton $E(\ell^+\ell^-)$ using theory templates with different values of $m_{\widetilde{Z}_2}$, but with $m_{\widetilde{Z}_2} - m_{\widetilde{Z}_1}$ fixed at 21 GeV. The corresponding values of χ^2 along with the parabolic fit is shown in Fig. 37*a*. It is found that $m_{\widetilde{Z}_2}$ is measured as

- $m_{\widetilde{Z}_2} = 123.7 \pm 0.2$ GeV (1σ),

a 0.2% measurement. Combining the $m_{\widetilde{Z}_2} - m_{\widetilde{Z}_1}$ and $m_{\widetilde{Z}_2}$ measurements also gives $m_{\widetilde{Z}_1}$:

- $m_{\widetilde{Z}_1} = 102.7 \pm 0.3$ GeV (ILC1-dileptons).

This value serves as a consistency check against the measurement of $m_{\widetilde{Z}_1}$ from chargino pair production, and most importantly, lends support to the SUSY interpretation of these events. The distribution of $E(\ell^+\ell^-)$ data are shown in Fig. 37*b*) along with the corresponding best fit depicted by the solid curve.

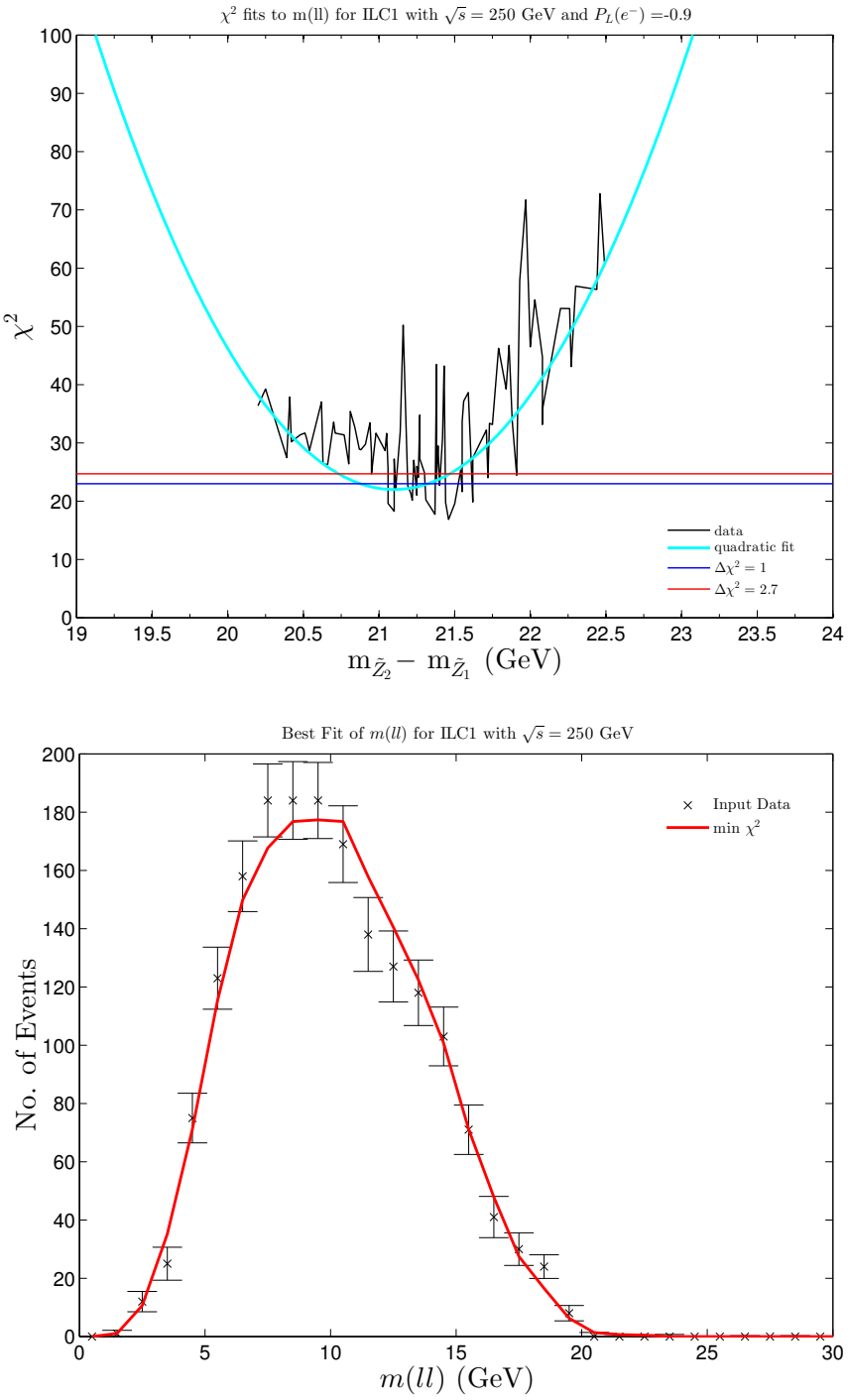


Figure 36: Shown in *a*) are values of χ^2 vs. $m(\ell^+\ell^-)$ from 100 fb^{-1} of OS/SF dilepton ILC1 "data" from $\widetilde{Z}_1\widetilde{Z}_2$ production fit to the shapes from various "theory" templates, as described in the text. In *b*), are the ILC1 "data" for the $m(\ell^+\ell^-)$ distribution from $\widetilde{Z}_1\widetilde{Z}_2$ events along with statistical error for 100 fb^{-1}. The solid curve shows the best fit to these "data".

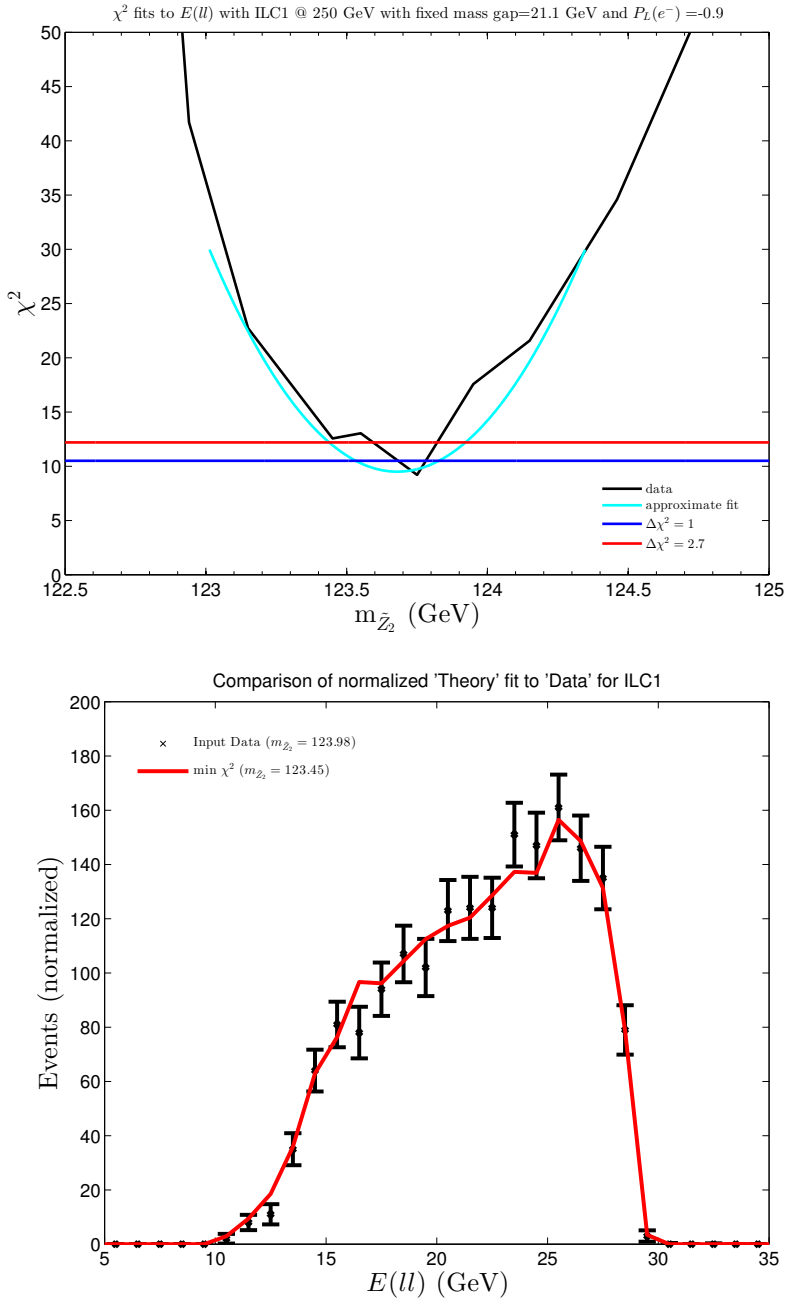


Figure 37: Shown in *a*), are fitted values of χ^2 found from matching 100 fb^{-1} of OS/SF dilepton "data" from $\widetilde{Z}_1\widetilde{Z}_2$ production to various "theory" distributions generated from varying $m_{\widetilde{Z}_2}$ while keeping $m_{\widetilde{Z}_2} - m_{\widetilde{Z}_1}$ fixed at 21 GeV. In *b*) is the distribution in $E(\ell^+\ell^-)$ from a 100 fb^{-1} of OS/SF dilepton ILC1 "data" from $\widetilde{Z}_1\widetilde{Z}_2$ production along with best fit.

5.6 Benchmark ILC2 at $\sqrt{s} = 340$ GeV

Benchmark point ILC2 is more challenging for ILC studies because the mass gap between $\widetilde{W}_1/\widetilde{Z}_2$ and the $\widetilde{Z}_1$ is just about 10 GeV, resulting typically in softer energy release from three-body $\widetilde{W}_1$ and $\widetilde{Z}_2$ decays. This mass gap is close to the minimum for RNS models where $\Delta_{\rm EW}^{-1} > 3\%$. Since charginos and neutralinos are heavier, its exploration requires a higher $\sqrt{s}$ to reach higgsino pair production threshold. In this case, studies are performed at $\sqrt{s} = 340$ GeV, enough for $\widetilde{W}_1^+\widetilde{W}_1^-$ and $\widetilde{Z}_1\widetilde{Z}_2$ production, but just below $t\bar{t}$ threshold. For these higher $\sqrt{s}$ values, the expected beamstrahlung parameter Υ is expected to increase to 0.03, while σ_z remains at 0.3 mm [112].

The E_{vis} distribution from signal and background is shown in Fig. 38. Here, the ILC2 signal is restricted to the region with $E_{vis} \lesssim 30$ GeV, while the background from $\gamma\gamma$ collisions is more severe than for the $\sqrt{s} = 250$ GeV case. Therefore, a cut of

- $E_{vis} < 30$ GeV.

is imposed.

Following the earlier analysis, the $E_T^{\rm miss}$ is examined in Fig. 39. Unlike the case of ILC1, the signal never emerges from the $\gamma\gamma$ background. Clearly additional cuts are necessary for observability of the signal.

5.6.1 Chargino pair production for ILC2

To extract a chargino pair production signal from the SM background for benchmark ILC2, it is required that:

- $E_{vis} < 30$ GeV,
- $E_T^{\rm miss} > 10$ GeV,

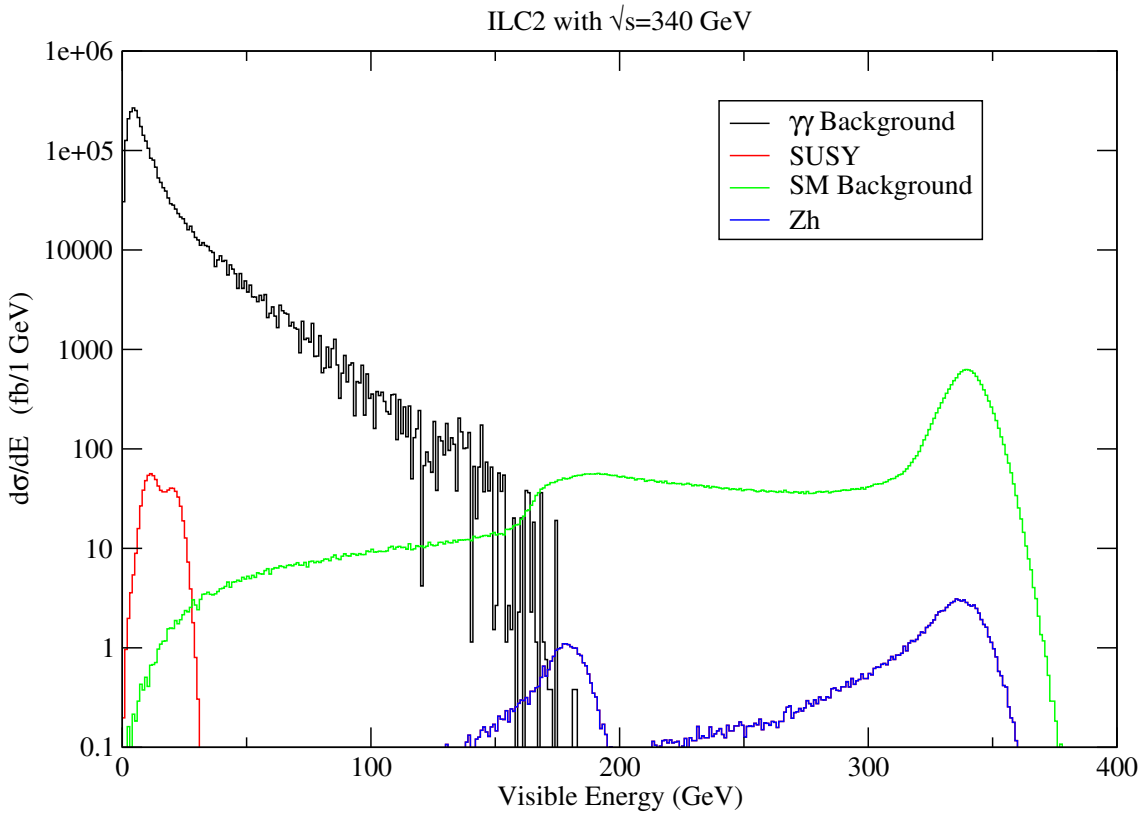


Figure 38: Distribution in E_{vis} from benchmark ILC2 signal and SM backgrounds at ILC with $\sqrt{s} = 340$ GeV and $\Upsilon = 0.03$.

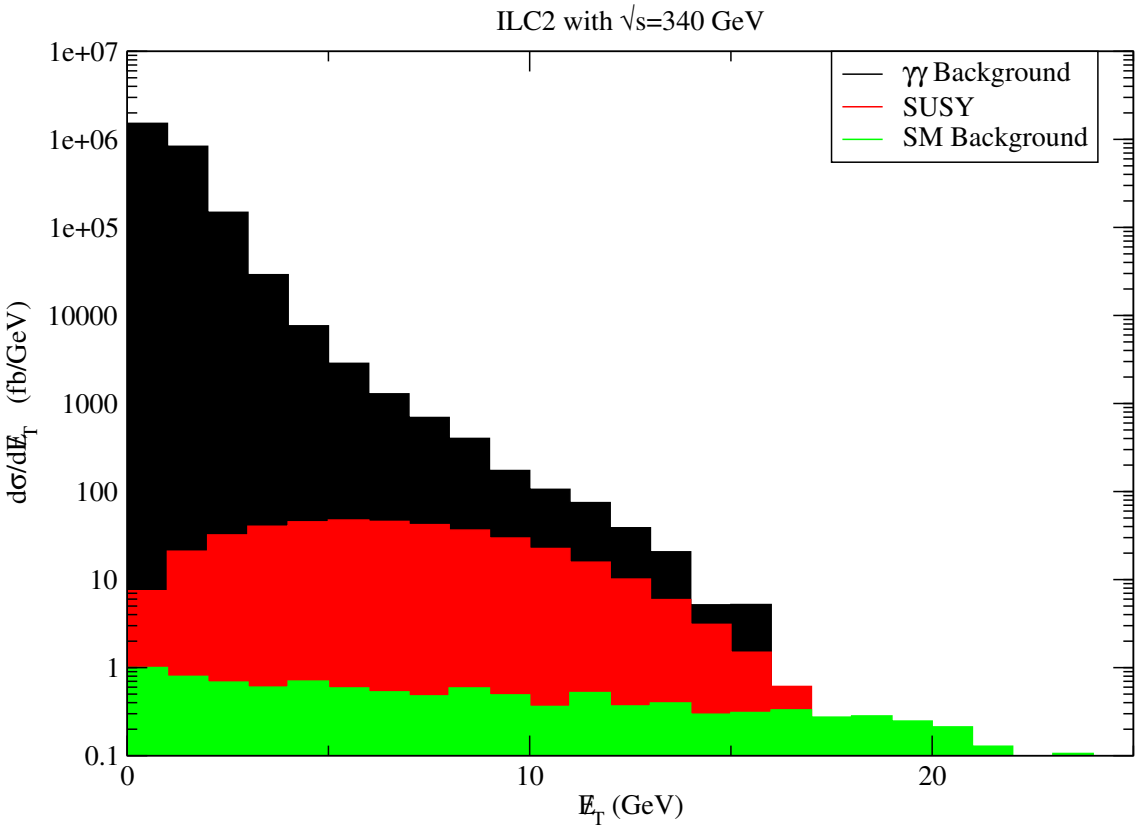


Figure 39: Distribution in missing transverse energy from e^+e^- collisions at $\sqrt{s} = 340$ GeV for signal from the ILC2 benchmark case, along with SM backgrounds from e^+e^- and $\gamma\gamma$ collisions. $E_{vis} < 30$ GeV is required. Beamstrahlung parameters are $\Upsilon = 0.03$ and $\sigma_z = 0.3$ mm.

- exactly one isolated lepton with $E > 5$ GeV and one jet with $E(j) > 5$ GeV.

For the case of ILC2, the hadronic energy release from $\widetilde{W}_1 \to q\bar{q}'\widetilde{Z}_1$ is so small that almost never are two resolvable jets produced, making chargino mass extraction difficult via continuum production (although perhaps still possible via threshold scans with sufficient integrated luminosity). Hence, instead the $n(\ell) = 1,\ n(jet) = 1$ signal is focused on. The transverse plane lepton-jet opening angle which is shown in Fig. 40. Most of the SM background comes from $\gamma\gamma \to \tau^+\tau^-$ followed by one leptonic and one hadronic tau decay. This may be mostly eliminated by requiring

- $\Delta\phi(\ell, jet) < 120°$.

After this cut, a signal of 7.1 fb is left while SM background is at the 2.8 fb level, and all of the $\gamma\gamma$ background, which arises from tau pair production, is eliminated. This should not be surprising because most taus that decay into 5 GeV jets/leptons will be significantly boosted, and hence tend to have their decay products nearly back-to-back in the transverse plane. The discovery of new physics might be possible with a data set of just a few fb^{-1} at ILC340 even in this difficult case.

5.6.2 Neutralino pair production for ILC2

As mentioned earlier, if any signal in the $1\ell 1j$ channel just discussed is to be attributed to higgsino-like charginos of SUSY, one may also expect a signal from $\widetilde{Z}_1\widetilde{Z}_2$ production as this reaction must have a comparable production cross section. Therefore, $\widetilde{Z}_1\widetilde{Z}_2$ production is examined for the ILC2 point with $\sqrt{s} = 340$ GeV, where $\widetilde{Z}_2 \to \ell^+\ell^-\widetilde{Z}_1$. This acoplanar dilepton signal may also allow for neutralino mass reconstruction via continuum production. It is required of the signal to have

- $E_{vis} < 30$ GeV,

- a pair of OS/SF leptons, with $n(j) = 0$,

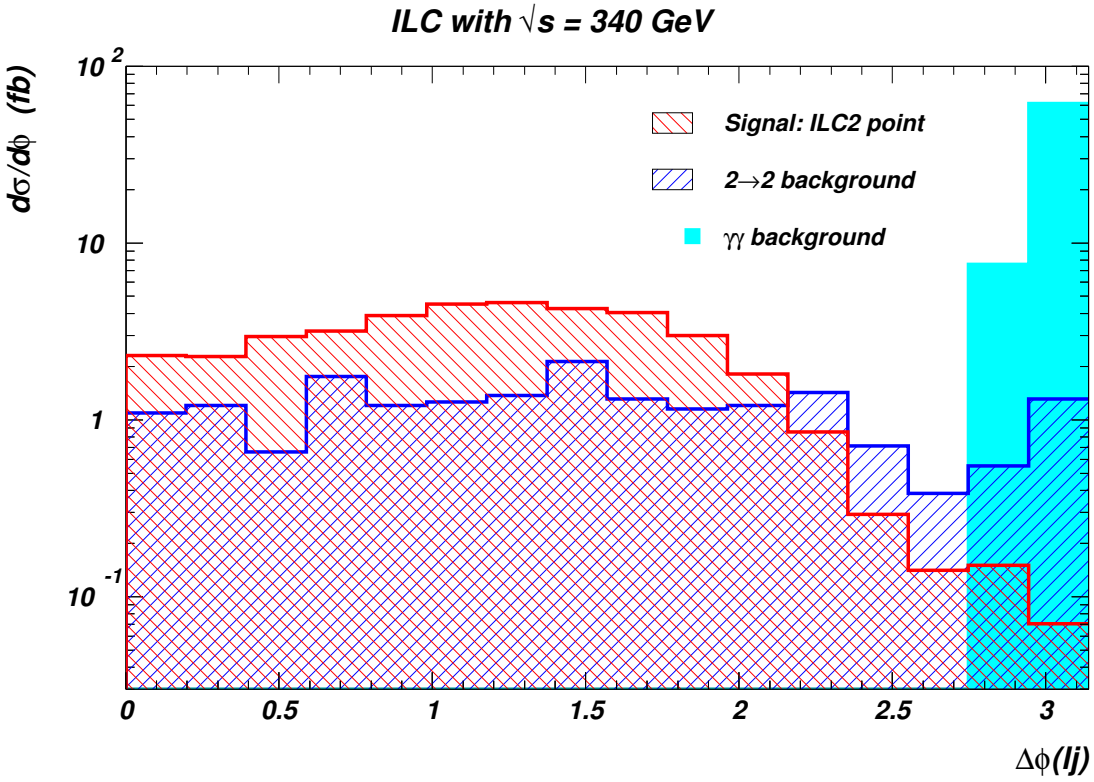


Figure 40: Distribution in transverse plane opening angle between the isolated lepton and jet for the ILC2 signal point at $\sqrt{s} = 340$ GeV, and for SM backgrounds. Here, $E_{vis} < 30$ GeV and $E_T^{\rm miss} > 10$ GeV. Beamstrahlung parameters are $\Upsilon = 0.03$ and $\sigma_z = 0.3$ mm.

- $E_T^{\rm miss} > 5$ GeV.

For this channel, mainly right polarized electron beams with $P_L(e^-) = -0.9$ are used to reduce backgrounds from W^+W^- and contamination from $\widetilde{W}_1^+\widetilde{W}_1^-$ production. The transverse OS/SF dilepton opening angle is plotted in Fig. 41. To eliminate the $\gamma\gamma$ background which is once again nearly back-to-back in the transverse plane, and to improve the signal-to-background ratio, it is required that:

- $\Delta\phi(\ell^+\ell^-) < 90^\circ$.

At this point, the signal has a cross section of 2.6 fb while SM background is at the 0.15 fb level with no $\gamma\gamma$ background. Once again, discovery of new physics is possible with just a few fb^{-1} of integrated luminosity. For benchmark ILC2, the same procedure is used as for the ILC1 case study to extract the neutralino masses. First the normalized theory templates (generated with 1000 fb^{-1} each) with varying $m_{\widetilde{Z}_2} - m_{\widetilde{Z}_1}$ mass gaps are fit to a 100 fb^{-1} "data" distribution. The various χ^2 values along with a parabolic fit are shown in Fig. 42*a*. As before, it was checked that the very large χ^2 values for a mass gap near the bottom of the parabola arise from extreme values of $m_{\widetilde{Z}_2}$ in the templates. For the ILC2 case, the $m_{\widetilde{Z}_2} - m_{\widetilde{Z}_1}$ mass gap is measured to be

- $m_{\widetilde{Z}_2} - m_{\widetilde{Z}_1} = 9.7 \pm 0.2$ GeV (1σ)

a 2% measurement. The data along with best theory fit are shown in Fig. 42*b*.

Keeping the mass gap fixed near 9.7 GeV, theory templates are generated for the $E(\ell^+\ell^-)$ distributions from $\widetilde{Z}_1\widetilde{Z}_2$ production with 10 times the statistics of "data" but with varying $m_{\widetilde{Z}_2}$ values and fit the shapes of these to the corresponding "data" distribution as before. Shown in Fig. 43, are the χ^2 values along with the parabolic fit. From this, a measurement of

- $m_{\widetilde{Z}_2} = 158.5 \pm 0.4$ GeV (1σ).

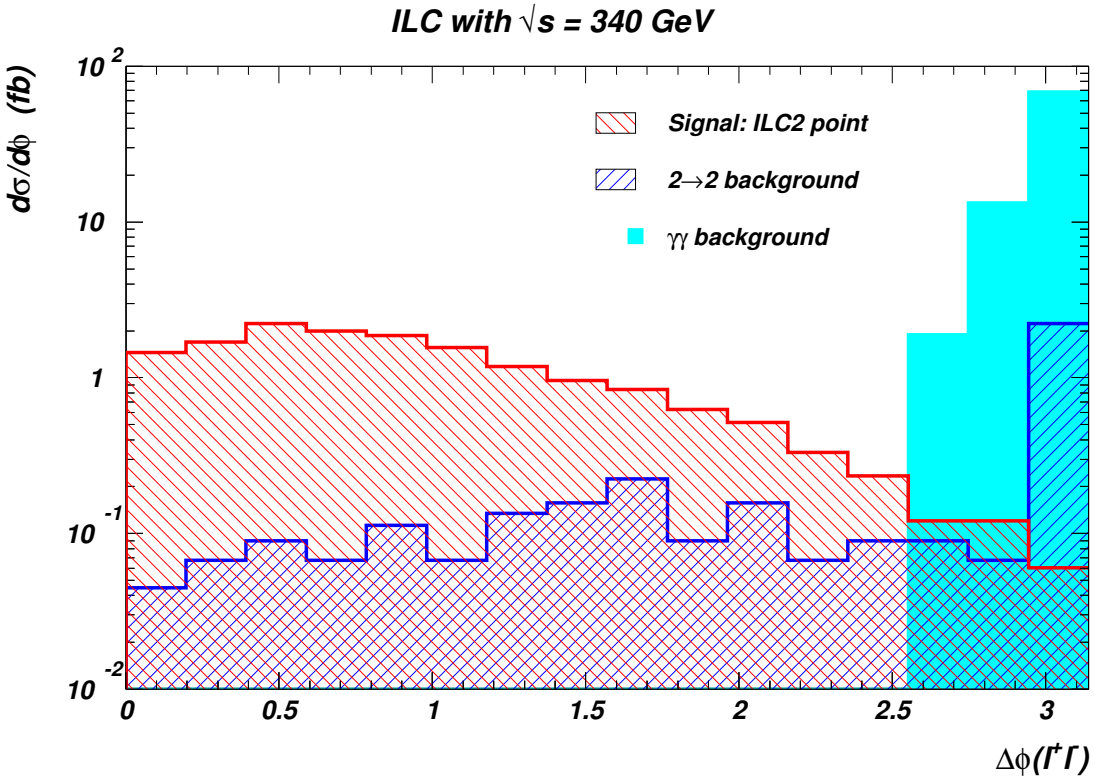


Figure 41: Distribution in transverse opening angle between isolated OS/SF leptons for ILC2 signal at $\sqrt{s} = 340$ GeV and for SM backgrounds. It is required that $E_{vis} < 30$ GeV and $E_T^{\rm miss} > 5$ GeV. Beamstrahlung parameters are $\Upsilon = 0.03$ and $\sigma_z = 0.3$ mm.

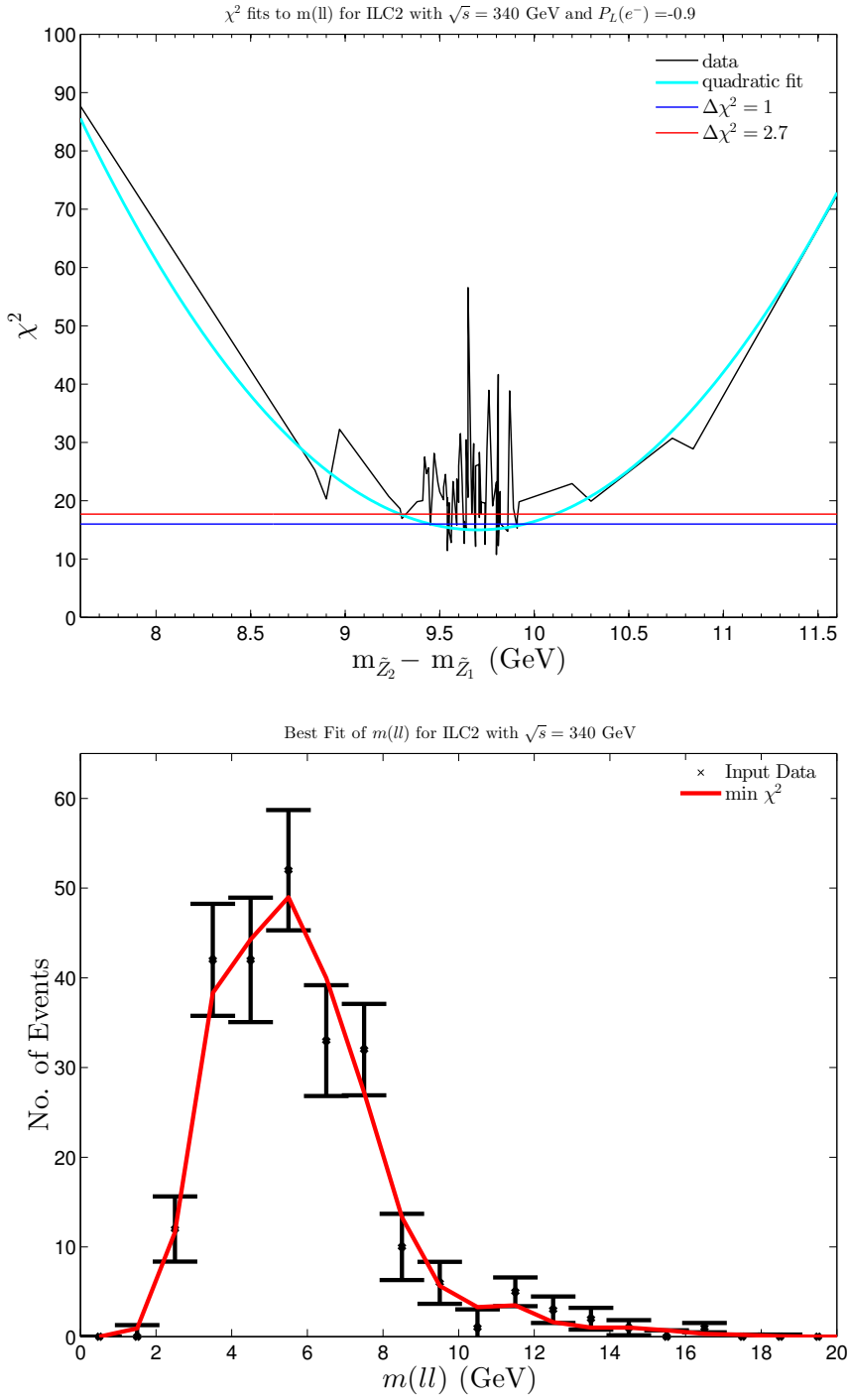


Figure 42: Shown in *a* are χ^2 values vs. $m(\ell^+\ell^-)$ from 100 fb^{-1} of OS/SF dilepton ILC2 "data" from $\widetilde{Z}_1\widetilde{Z}_2$ production fit to theory along with a best-fit parabola. In *b*) is the distribution in $m(\ell^+\ell^-)$ from a 100 fb^{-1} of OS/SF dilepton ILC2 "data" from $\widetilde{Z}_1\widetilde{Z}_2$ production along with best fit.

is found. The $E(\ell^+\ell^-)$ distribution for "data" along with best fit theory are shown in Fig. 43*b*. By combining the $m_{\tilde{Z}_2}$ and mass gap measurements, one finds

- $m_{\tilde{Z}_1} = 148.8 \pm 0.5$ GeV (ILC2-dileptons).

Although this analysis was performed using the RNS model as a guide, the results should be applicable to all models with light higgsinos. It is encouraging that even the difficult point with the smallest mass gap for 150 GeV higgsinos allows not only detection, but also precision mass measurements, even at a centre-of-mass energy just modestly above the production threshold. This leads one to infer that an electron-positron collider will serve as a definitive probe of the idea of naturalness in all SUSY models where the μ-term is the dominant contribution to higgsino masses. In particular, from the dashed contour in Fig. 27, one may conclude that ILC600 will either discover or decisively exclude models where fine-tuning is worse than 3%. Precision measurements that can be made at ILC will definitively show that higgsino pair production is indeed occuring, and will allow measurement with high precision at least the higgsino mass scale and associated mass gaps.

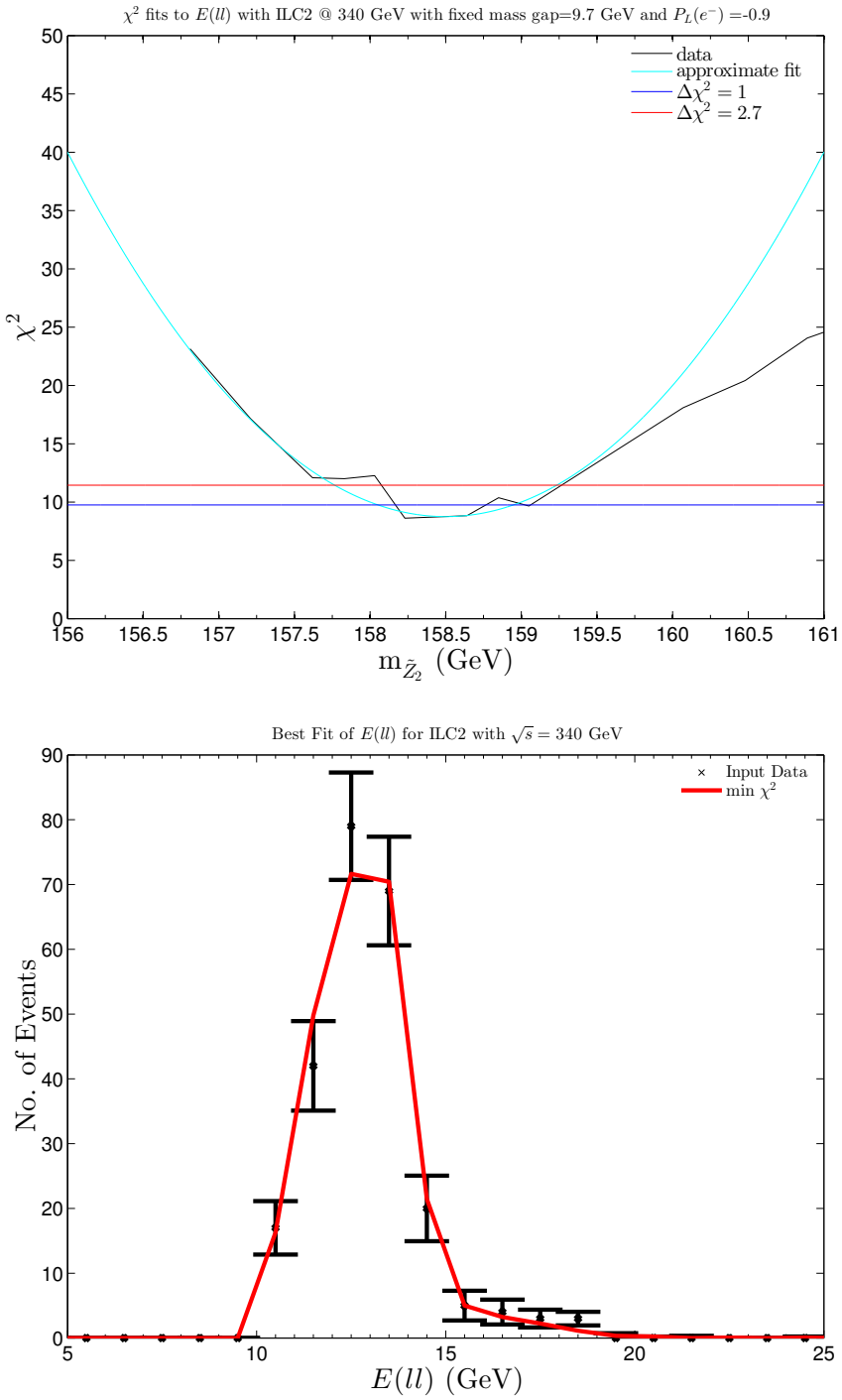


Figure 43: Shown in *a*) are values of χ^2 found from matching 100 fb^{-1} of OS/SF dilepton ILC2 "data" from $\widetilde{Z}_1\widetilde{Z}_2$ production to various "theory" distributions generated from varying $m_{\widetilde{Z}_2}$ while keeping $m_{\widetilde{Z}_2} - m_{\widetilde{Z}_1}$ fixed at 9.7 GeV. In *b*) is the distribution in $E(\ell^+\ell^-)$ from a 100 fb^{-1} of OS/SF dilepton ILC2 "data" from $\widetilde{Z}_1\widetilde{Z}_2$ production along with best fit.

6 Radiative Natural Supersymmetry and Dark Matter [39]

Dark matter (DM) has been postulated to account for several unexplained phenomena, such as anisotropies in cosmic microwave background (CMB) and discrepencies between luminosity and gravitational effects in mass measurements of stellar objects. Possibly the strongest evidence for DM came with the study of rotation curves of spiral galaxies. Assuming Newtonian dynamics and spherical symmetry, the rotational velocity $v(r)$ at a distance r can be related to the mass of the galaxy $M(r)$ by

$$v(r) = \sqrt{\frac{GM(r)}{r}} \tag{6.1}$$

where G is Newton's gravitation constant. Therefore, outside of a large enough radius, $M(r)$ is expected to be constant and $v(r)$ should fall off as $r^{-1/2}$. However, this is not the case in measurement, where $v(r)$ flattens out and remains constant. This measurement suggests that a halo of DM surrounds each galaxy. Many different types of DM have been theorized, such as black holes, hot (relativistic) dark matter, and various forms of cold dark matter (CDM). However, of these candidates CDM is required by experimental evidence.

One possibility for a CDM candidate is the weakly-interacting massive particle, or WIMP. In addition to collider searches, as addressed previously, SUSY might be found much earlier by discovery of higgsino-like WIMPs. As seen above, the LSP in RNS is the lightest higgsino-like neutralino $\widetilde{Z}_1$. The conservation of R-parity implies $\widetilde{Z}_1$ is stable; in addition, it does not interact via the electromagnetic or strong forces. Therefore $\widetilde{Z}_1$ is an excellent WIMP candidate.

Big bang nucleosynthesis (BBN) and data from WMAP [115] and other experiments suggest that the baryonic matter density of the universe is $\Omega_b h^2 \simeq 0.0224$, whereas the total matter density estimate is $\Omega_m h^2 \simeq 0.135$. Here, Ω is the ratio of the density to the critical density of the universe $\Omega = \rho/\rho_c$, h is a dimensionless

scaling constant that parameterizes the Hubble constant $H_0 \equiv 100h$ km s^{-1} Mpc^{-1}, and the critical density $\rho_c = \frac{3H_0^2}{8\pi}$ is the density for which the the spatial geometry is flat. These values imply that the cold dark matter density is $\Omega_{CDM}h^2 \simeq 0.11$. For the lightest neutralino to be a viable CDM particle, one would expect the *relic density* of neutralinos leftover from the big bang to make up a portion of $\Omega_{CDM}h^2$, possibly supplemented by other CDM particles, such as axions. The predicted relic density of neutralinos $\Omega_{\widetilde{Z}_1}h^2$ can be found by using the Boltzmann equation in the Freidmann-Robertson-Walker metric,

$$\frac{dn}{dt} = -3Hn - \langle\sigma_{ann}v\rangle\,(n^2 - n_{eq}^2), \tag{6.2}$$

Here, n is the number density of neutralinos, t is time, n_{eq} is the thermal equilibrium number density of neutralinos, and $\langle\sigma_{ann}v\rangle$ is the thermally averaged neutralino annihilation cross section times the relative velocity.

In the early universe, the WIMPs are in thermal equilibrium and follow a Maxwell-Boltzmann distribution with the number density decreasing exponentially with the temperature. However, as the universe cools and expands the number density of WIMPs

$$n_{eq} = g(\frac{mT}{2\pi}^{3/2})e^{-(m-\mu)/T} \tag{6.3}$$

decreases until the *freeze-out temperature* T_{fr} is reached, at which time the density of WIMPs only reduces due to the expansion. Here, g is the number of degrees of freedom and μ is the chemical potential. Therefore, the number of neutralinos would be larger than expected from thermal equlibrium and becomes effectively constant per co-moving volume.

At the freeze-out temperature, the Hubble term and the scattering term in

Eq. 6.2 become comparable, *i.e.*

$$\langle \sigma_{ann} v \rangle \, n \simeq H(T_{Fr}), \tag{6.4}$$

which defines the freeze-out temperature. Using the Friedmann relation for a radiation dominated universe (it is assumed here that freeze-out occurs in a radiation dominated phase),

$$H^2 = \frac{8\pi G \rho_r}{3} = \frac{\rho_r}{3M_P^2}, \tag{6.5}$$

where

$$\rho_r = \frac{\pi^2}{30} g_*(T) T^4 \tag{6.6}$$

is the radiation density, $H(T)$ is the Hubble parameter, M_P is the reduced Planck mass, and g_* is the number of relativistic degrees of freedom at a temperature T. One may now define the yield variable as

$$Y \equiv \frac{n}{s} = \frac{H}{\langle \sigma_{ann} v \rangle \, s}, \tag{6.7}$$

with the entropy density s given by

$$s = \frac{2\pi^2}{45} g_*(T) T^3. \tag{6.8}$$

Combining Eq.'s 6.6 and 6.8 into Eq. 6.7 gives the yield as

$$Y_{Fr} = \frac{(90/\pi^2 g_*(T_{Fr})(T_{Fr}))^{1/2}}{4 \langle \sigma_{ann} v \rangle \, M_P T_{Fr}} \tag{6.9}$$

It is assumed that the yield is conserved from $T = T_{Fr}$ to $T = T_0$ where T_0 is the present day temperature of radiation. Now the neutralino relic density (also known as the 'standard thermal neutralino abundance' can be written in terms of the yield,

accounting for the entropy density for *today* as

$$\Omega_{\tilde{Z}_1}^{std}h^2 = \frac{2\pi^2 g_*(T_0)T_0^3}{45\rho_c/h^2} m_{\tilde{Z}_1} Y_{Fr} \tag{6.10}$$

In Eq. 6.10, ρ_c and h^2 appear from the definition of Ωh^2 and $m_{\tilde{Z}_1}$ is from writing the energy density of the neutralinos as $\rho_{\tilde{Z}_1} = m_{\tilde{Z}_1} Y_{Fr} s$.

While this calculation made several simplifications, it is a good estimate and gives the general behavior of the relic density. The relic density and annihilation cross section calculations are often calculated in real-time numerically using computer packages, such as in the IsaReD [116] relic density subroutine.

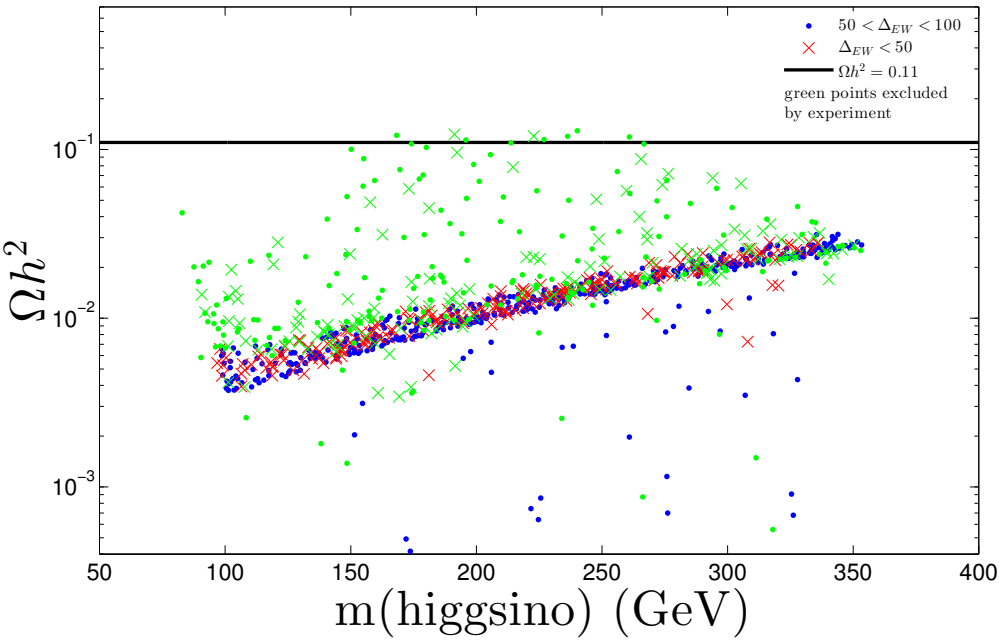


Figure 44: Plot of standard thermal neutralino abundance $\Omega_{\tilde{Z}_1}^{std}h^2$ versus higgsino mass from a scan over NUHM2 parameter space with $\Delta_{\rm EW} < 50$ (red crosses) and $\Delta_{\rm EW} < 100$ (blue dots). Green points are excluded by current direct and indirect search experiments.

Using the same NUHM2 parameter space as Section 3, RNS models are generated and the IsaReD [116] relic density subroutine is used to calculate the 'standard

thermal neutralino abundance' $\Omega^{std}_{\widetilde{Z}_1}h^2$ which is the relic density expected from the model point. Only models with $\Omega^{std}_{\widetilde{Z}_1}h^2 < 0.12$ and $m_{\widetilde{W}_1} > 103.5$ GeV were accepted. The relic abundance is shown in Fig. 44, where the red crosses have $\Delta_{\rm EW} < 50$ and blue dots have $\Delta_{\rm EW} < 100$. Green points are excluded by current direct and indirect search limits. In the figure, one sees a high density band of parameter space points from $\Omega^{std}_{\widetilde{Z}_1}h^2 \sim 0.004$ for $\widetilde{Z}_1 \sim 100$ GeV to $\Omega^{std}_{\widetilde{Z}_1}h^2 \sim 0.02$ for $\widetilde{Z}_1 \sim 300$ GeV. Thus, there is typically an *underabundance* of higgsino dark matter compared to measurement from WMAP9 by a factor ranging from 3-25. There is some spread in these values above and below the main band from cases where μ is quite large and $m_{1/2}$ is small so that one has instead a mixed higgsino-bino LSP state. The bulk of points above the band are already excluded as will be seen. The neutralino abundance is expected to be low, as the annhililation rate for higgsino-like WIMPs tends to be large since $\Omega h^2 \propto \langle \sigma v \rangle^{-1}$. This implies that a mainly higgsino-like neutralino by itself is not an ideal CDM candidate. The main annihilation channels are $\widetilde{Z}_1\widetilde{Z}_1 \to W^+W^-(\sim 60\%)$, and $ZZ(\sim 26\%)$ with the remainder coming from annihilation in Zh and $\widetilde{Z}_1\widetilde{W}_1$ co-annihilation. These annihilation channels are as expected from mainly higgsino-like WIMP states [117].

To address the underabundance of WIMPs, it is possible to consider the Peccei-Quinn-Weinberg-Wilczek solution to the strong CP problem [29, 30, 31, 32] which introduces a PQ symmetry and the resultant axions from PQ symmetry breaking. The SUSY partners of the axions are the R-parity-even spin-0 *saxions* s and R-parity-odd spin-$\frac{1}{2}$ *axinos* $\tilde{a}$ [118]. In models of gravity mediation, as is the case in RNS, the saxion and axino are expected to have masses of $m_s \sim m_{\tilde{a}} \sim m_{3/2} \sim 5-20$ TeV [119]. The axion itself will be much lighter ($\sim \mu$eV), but depends on the scale of PQ symmetry breaking. In this case, the dark matter would consist of both axions and higgsinos acting as co-dark matter particles.

The relic abundance of mixed axion-neutralino CDM has been addressed in Refs

[120, 121]. In [121], it was found that SUSY models with a standard overabundance of dark matter are still excluded in the PQMSSM by a combination of dark matter overabundance constraints, big bang nucleosynthesis (BBN) constraints and dark radiation constraints. However, SUSY models with a standard underabundance of neutralinos are still allowed over large ranges of PQMSSM parameters. In RNS models, for any particular parameter set, one expects the relic higgsino abundance to lie somewhere between the standard value $\Omega^{std}_{\widetilde{Z}_1}h^2$ (which would correspond to axion domination) up to the measured value 0.11, in which case CDM would be higgsino-dominated. The question then arises: what are the prospects for direct/indirect detection of relic higgsinos in WIMP detection experiments?

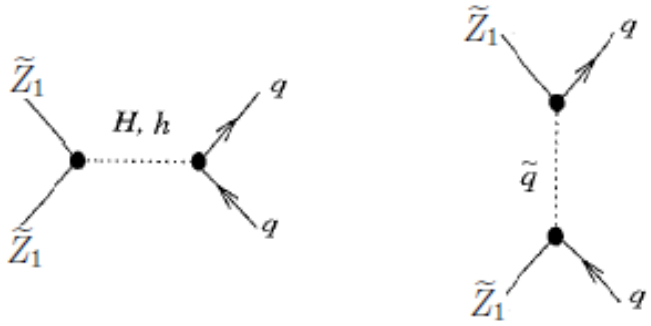


Figure 45: Two of the Feynman diagrams that contribute to the nucleus-neutralino interactions. On the left is Higgs exchange, the light Higgs exchange will dominate, since the heavy Higgs will not contribute in the decoupling limit. On the right is squark exchange.

6.1 Direct Detection of higgsino-like WIMPs

There are currently several experiments hoping to detect dark matter directly through scattering from nuclei. This is attempted far underground to reduce induced radioactivity background from high energy cosmic rays. The idea is that as the Earth moves through the galaxy, DM particles will pass through a media (such as liquid Xenon or Germanium crystals) and interact with nuclei, releasing energy which can be detected. A typical neutralino-nucleus elastic scattering event will involve energies of

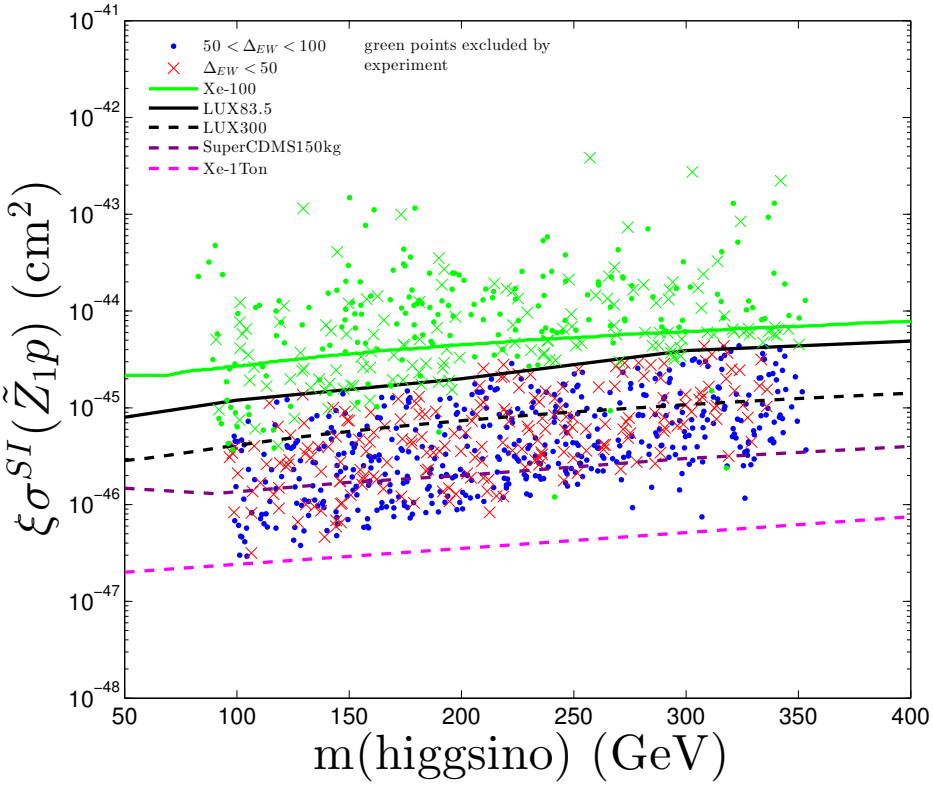


Figure 46: Plot of rescaled WIMP spin-independent detection rate $\xi\sigma^{SI}(\widetilde{Z}_1 p)$ versus m(higgsino) from a scan over NUHM2 parameter space with $\Delta_{\rm EW} < 50$ (red crosses) and $\Delta_{\rm EW} < 100$ (blue dots). Green points are excluded by current direct and indirect search experiments. Also shown is the reach of Xe-100 experiement, the LUX experiment after 83.5 days of running, and the projected reaches of LUX300, SuperCDMS 150 kg and Xe-1 ton.

just 10's of keV. Because of the low energies involved, these are approximated as effective operators of four particle interactions.

There are two types of interactions, spin-*independent* and spin-*dependent*. Which one dominates will depend on the type of nucleus of the interaction media. The spin-independent interaction will typically be larger, because the interaction will sum for all available nucleons and the neutralino will scatter via the entire mass of the particle. The diagrams in Fig. 45 contribute to spin-independent scattering. In spin-dependent scattering, the neutralino will scatter only via the spin of the nucleus, such as an interaction with a hydrogen atom in the Sun's core. The spin-dependent scattering can occur through Z-exchange and squark exchange, however, the squark decouples and Z-exchange will dominate.

As an example, the direct detection interaction diagrams between the neutralinos and quarks via Higgs and squark exchange are illustrated in Fig. 45 (not shown, but allowed, is the neutralino-gluon interaction). On the left is the Higgs exchange. Both the light and heavy Higgs scalars are shown, however, due to their large masses, the heavy Higgs and squarks will decouple and not contribute.

Shown in Fig. 46 are the spin-independent higgsino-proton scattering rates calculated by IsaReS [122]. These rates are adjusted by a rescaling factor $\xi =$ to account for the fact that the local WIMP density may be far below the usual assumed value $\rho_{local} \simeq 0.3$ GeV/cm^3, as suggested by Bottino *et al.* [123] (the remainder would be composed of axions). As discussed above, the WIMP in the present case scatters from quarks and gluons mainly via h exchange. The $\widetilde{Z}_1 - \widetilde{Z}_1 - h$ coupling involves a product of both higgsino and gaugino components. In the case of RNS models, the $\widetilde{Z}_1$ contains enough gaugino component that the coupling is never small: in the notation of [24]

$$\mathcal{L} - X_{11}^h \bar{\widetilde{Z}}_1 \widetilde{Z}_1 h \tag{6.11}$$

where

$$X_{11}^h = -\frac{1}{2}\left(v_2^{(1)}\sin\alpha - v_1^{(1)}\cos\alpha\right)\left(gv_3^{(1)} - g'v_4^{(1)}\right), \tag{6.12}$$

and where $v_1^{(1)}$ and $v_2^{(1)}$ are the higgsino components, $v_3^{(1)}$ and $v_4^{(1)}$ are the gaugino components of the lightest neutralino, α is the Higgs mixing angle, and g and g' are the $SU(2)_L$ and $U(1)_Y$ gauge couplings. As can be seen in the figure, the Xe-100 [124] and LUX [125] experiments are already probing the parameter space. The Xe-1-ton [126] (which is currently being deployed) or other comparable noble liquid detectors can make a complete exploration of RNS parameter space.

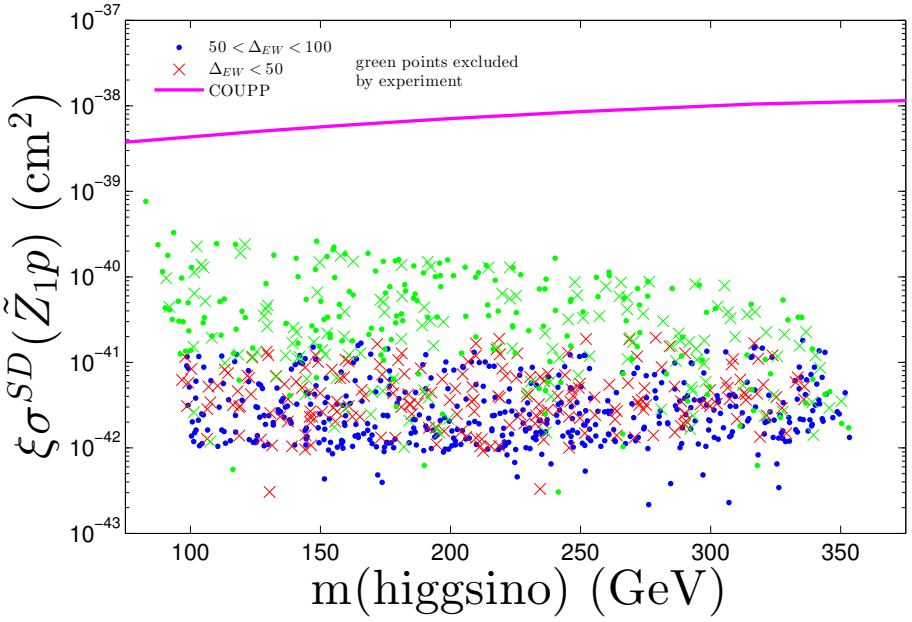


Figure 47: Plot of rescaled spin-dependent higgsino-like WIMP detection rate $\xi\sigma^{SD}(\widetilde{Z}_1 p)$ versus m(higgsino) from a scan over NUHM2 parameter space with $\Delta_{\rm EW} < 50$ (red crosses) and $\Delta_{\rm EW} < 100$ (blue dots). Green points are excluded by current direct/indirect WIMP search experiments. Also shown is the current reach of the COUPP detector.

Figure 47 shows the rescaled spin-dependent higgsino-proton scattering cross section $\xi\sigma^{SD}(\widetilde{Z}_1 p)$. Also shown are recent limits from the COUPP [127] detector. COUPP is a 'bubble detector' that uses purified water along with the chemical CF3I, kept at a temperature near boiling point. When a particle passes through the liquid,

bubbles will form along the ionized recoil trail, which can be observed. Current limits are still about an order of magnitude away from reaching the predicted rates from RNS models.

6.2 Indirect Detection of higgsino-like WIMPs

Indirect detection focuses on discovering dark matter through either decays or annihilation and searching for the decay/annihilation product. This differs from direct detection, where the detection media interacts directly with the dark matter as described in the previous section. One such detector is the IceCube detector at the South Pole Neutrino Observatory [128]. In Fig. 48 the value of the non-rescaled spin-dependent scattering cross section is shown, along with the reach of the IceCube experiment.

As the Sun moves through the galaxy and the DM halo that permeates it, WIMPs can be swept up and scatter within the Sun's core. If enough energy is lost in the scattering, the WIMP can then become captured within the Sun and accumulate at high density in the solar core. Within the core, WIMPs can annihilate with each other into SM particles. Most are absorbed by the solar material, but high energy GeV scale neutrinos can escape. IceCube tries to detect these by their conversion to muons in the ice. The detection rates therefore do not include the rescaling factor ξ because the IceCube detection rates depend on whether the Sun has equilibrated its core abundance between capture rate and annihilation rate [117] and not the local WIMP density. Typically for the Sun, equilibration is reached for almost all of SUSY parameter space [129]. The IceCube limits have entered the RNS parameter space and exclude the larges values of $\sigma^{SD}(\widetilde{Z}_1 p)$.

Shown in Fig. 49 is the thermally averaged neutralino annihilation cross section times relative velocity in the limit as $v \to 0 : \xi^2 \langle \sigma v \rangle_{v \to 0^+}$. Here the rescaling factor ξ is squared since limits depend on the square of the local WIMP abundance [130].

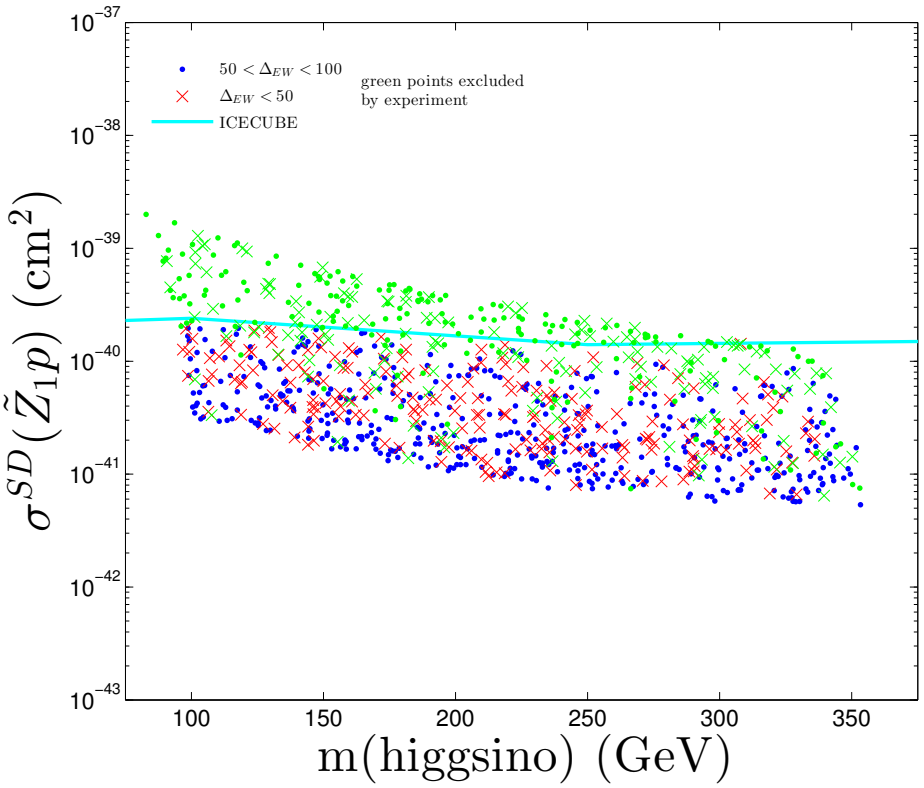


Figure 48: Plot of (non-rescaled) spin-dependent higgsino-like WIMP detection rate $\sigma^{SD}(\widetilde{Z}_1 p)$ versus m(higgsino) from a scan over NUHM2 parameter space with $\Delta_{\rm EW} < 50$ (red crosses) and $\Delta_{\rm EW} < 100$ (blue dots). Green points are excluded by current direct/indirect WIMP search experiments. Also shown is the current reach from IceCube.

Space-based satellite experiments search for anomalously high rates for antimatter or photon production, e.g. the Fermi-LAT satellite or AMS-02 aboard the space station. WIMPs in space may annihilate one against another into matter-antimatter pairs into SM particles which then decay to photons. On the plot, the limit derived from the Fermi LAT gamma ray obervatory [131] for WIMP annihilations into WW is shown. These limits have not yet reached the RNS parameter space due in part to the squared rescaling factor. Anomalies in the positron and γ spectra have been reported, although the former may be attributed to pulsars [132], while the latter 130 GeV gamma line may be instrumental. In Ref. [133], constraints on the pMSSM model have been derived from lack of anti-proton signal in PAMELA data [134]. The anti-proton and gamma-ray constraints from [133] occur at $\langle\sigma v\rangle$ values $\sim 10^{-25}\mathrm{cm}^3/\mathrm{s}$. In the current case where the galactic annihilation rates are suppressed by the ξ^2 factor, the rates lie a couple orders of magnitude below these limits.

In addition to the discovery of higgsino-like WIMPs, discovery of axions is expected in co-dark matter scenarios. The Axion Dark Matter Experiement (ADMX) [135] searches for axions by exploiting their coupling with photons. Axions would necessarily exist in the dark matter halo that permeates our galaxy (which would also include the WIMP neutralinos). ADMX uses a microwave cavity with strong magnetic field which, if the axions exist at the resonant frequency of the cavity, will decay into microwave photons via the $a-\gamma-\gamma$ coupling. So far, no positive results have been reported.

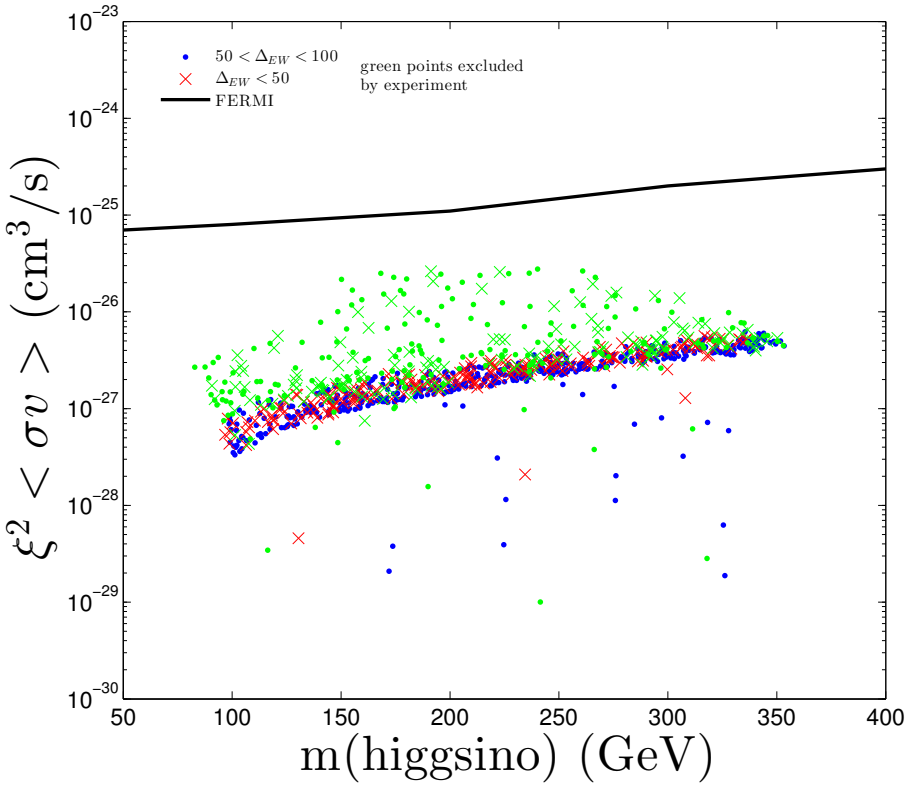


Figure 49: Plot of rescaled $\xi^2 \langle \sigma v \rangle_{v \to 0}$ versus m(higgsino) from a scan over NUHM2 parameter space. Green points are excluded by the current direct and indirect WIMP search experiments.

7 Summary

Recent results from LHC7 and LHC8, setting the limits $m_{\tilde{g}} \stackrel{>}{\sim} 1.8$ TeV (for $m_{\tilde{g}} \simeq m_{\tilde{q}}$) and $m_{\tilde{g}} \stackrel{>}{\sim} 1.3$ TeV (for $m_{\tilde{g}} \ll m_{\tilde{q}}$), have resulted in heightened concern for reconciling electroweak naturalness with lack of SUSY signals and the rather large value of $m_h = 125$ GeV. It has been argued that this reconciliation can occur within the context of radiatively-driven natural supersymmetry (or RNS) where $m_{H_u}^2$ is driven to a small negative value and $\mu \sim m_Z$.

RNS is a SUSY model based on the MSSM, which may be valid all the way up to the GUT scale. Thus, it maintains the desirable features of gauge coupling unification and radiative electroweak symmetry breaking while avoiding the introduction of extra possibly destabilizing gauge singlets or other forms of exotic matter. The main features of the RNS model include 1) a low value of superpotential higgsino mass $|\mu| \sim 100 - 300$ GeV, and 2) a weak scale value of $-m_{H_u}^2 \sim m_Z^2$: both these qualities are required to fulfill electroweak naturalness at the tree level. The term $m_{H_u}^2$ is driven to low values radiatively by the same mechanism leading to REWSB and depends on a large top quark Yukawa coupling.

The EWFT is evaluated at the 1-loop level. In this case, top squark masses enter the computation of $\Delta_{\rm EW}$ and are also driven radiatively to few-TeV values. By allowing for large top-squark mixing ($|A_0| \sim (1-2)m_0$), top-squark contributions to EWFT are suppressed at the same time as the light Higgs boson mass is uplifted: thus, the model reconciles electroweak fine-tuning with $m_h \simeq 125$ GeV all in the context of the MSSM.

RNS may be realized in the two-parameter non-universal Higgs models NUHM2, but not the more common mSUGRA/CMSSM model. In this case, low EWFT with $\Delta_{\rm EW} \stackrel{<}{\sim} 10$, which corresponds to 10 % EWFT, can be attained for model parameters which lead to a distinctive mass spectrum:

- light higgsino-like $\widetilde{W}_1^{\pm}$ and $\widetilde{Z}_{1,2}$ with mass $\sim 100 - 300$ GeV,
- gluinos with mass $m_{\tilde{g}} \sim 1 - 4$ TeV,
- heavier top squarks than generic NS models: $m_{\tilde{t}_1} \sim 1 - 2$ TeV and $m_{\tilde{t}_2} \sim 2 - 5$ TeV,
- first/second generation squarks and sleptons with mass $m_{\tilde{q},\tilde{\ell}} \sim 2 - 10$ TeV. The $m_{\tilde{\ell}}$ range can be pushed up to 20-30 TeV if non-universality of generations with $m_0(1,2) > m_0(3)$ is allowed.

The RNS model with the above spectra also fulfills limits from rare B-decay measurements, which can (along with the value of m_h) be an Achilles heel for generic NS models with much lighter third generation squarks.

The RNS model can be tested at LHC for a range of parameter space. An RNS model line was constructed which allows variable $m_{1/2}$. It was found that $\tilde{g}\tilde{g}$ production followed by cascade decays leads to the expected leptons+jets+$E_T^{\rm miss}$ events. These should allow values of $m_{\tilde{g}}$ up to ~ 1.7 TeV to be discovered by LHC14 with about 300 fb^{-1} of integrated luminosity.

A qualitatively new signal, endemic to SUSY models with light higgsinos, arises mainly from wino pair production $pp \to \widetilde{W}_2\widetilde{Z}_4 \to (W^{\pm}\widetilde{Z}_{1,2}) + (W^{\pm}\widetilde{W}_1^{\mp})$ which leads to same sign-diboson production accompanied by minimal jet activity. After cuts, the largest background comes from $t\bar{t}W$ production. This channel seems to offer the best reach for RNS for higher integrated luminosity values > 100 fb^{-1}. The SSdB signal from wino pair production may be confirmed if the decays of $\widetilde{W}_2$ and $\widetilde{Z}_4$ yield a final state with $WZ \to 3\ell + E_T^{\rm miss}$ at high integrated luminosity. Wino pair production also leads to observable $4\ell + E_T^{\rm miss}$ signals for $m_{1/2} \lesssim 500$ GeV (up to ~ 650 GeV at the high-luminosity LHC). Signals in the soft 3ℓ channel arising from direct higgsino pair production $pp \to \widetilde{W}_1^{\pm}\widetilde{Z}_2$ were also explored. This channel should be visible over the lower $m_{1/2}$ range, which provide a large enough

$m_{\tilde{Z}_2} - m_{\tilde{Z}_1}$ mass gap such that one may avoid the $2 \to 4$ process $W^*Z^*/W^*\gamma^*$ which contains an obstructing virtual photon contribution at the lower portion of the $m(\ell^+\ell^-)$ distribution. Detection will likely be possible via the analysis of the shape of the dimuon invariant mass distribution for $e^{\pm}\mu^+\mu^-$ events where there should be a distortion due to an excess for $m(\mu^+\mu^-) < m_{\tilde{Z}_2} - m_{\tilde{Z}_1}$.

To probe the possibilites at a linear collider, two benchmark scenarios were investigated: ILC1 with lighter higgsinos ~ 120 GeV and mass gap $\sim 15 - 22$ GeV relative to the LSP, and ILC2 with heavier higgsinos ~ 150 GeV but with a mass gap of just 10 GeV, close to the minimum possible in models with no worse than 3% fine-tuning.

For both these cases, the chargino pair and neutralino pair signals should be seen above usual SM $2 \to 2$ background and $\gamma\gamma$ induced events via a combination of specially devised E_{vis}, $E_T^{\rm miss}$, angle and topology cuts with an integrated luminosity of just a few fb^{-1}. The signal will be characterized by low E_{vis} ($\lesssim 30-50$ GeV) plus $E_T^{\rm miss}$ events indicating the production of heavy parents that decay into an invisible partner with a mass just 10-20 GeV lighter. Observation of a signal in both $jet(s)+\ell$ and OS/SF dilepton channels at the expected rates will point to the production of higgsinos that are the hallmark of natural SUSY models. For ILC1, the $\ell + jets$ signal allows for a continuum measurement of $m_{\widetilde{W}_1}$ and $m_{\tilde{Z}_1}$ to $\sim 2\%$ accuracy assuming a canonical value of 100 fb^{-1} of integrated luminosity. The neutralino pair production reaction can be seen above the background in the OS/SF, same-side dilepton signal which allows for the mass gap $m_{\tilde{Z}_2} - m_{\tilde{Z}_1}$ to be measured via the $m(\ell^+\ell^-)$ distribution to $\sim 1\%$ accuracy while $m_{\tilde{Z}_2}$ can be measured to sub-GeV precision.

The more challenging ILC2 point allows for chargino pairs to be seen above background, but the smaller $m_{\widetilde{W}_1} - m_{\tilde{Z}_1}$ mass gap makes dijet resolution very difficult so that a continuum mass measurement via $E(jj)$ is not possible with the simplified

methods used here. The OS/SF same-side dilepton measurement still remains viable in the case of ILC2 where the mass gap $m_{\widetilde{Z}_2} - m_{\widetilde{Z}_1}$ can be measured to $\sim 2\%$ accuracy and $m_{\widetilde{Z}_2}$ can be again measured to sub-GeV precision.

In RNS, one also expects the presence of higgsino-like WIMPs which have large rates for direct and indirect WIMP detection. With the ILC over a decade away, and signals possibly hidden at the LHC, these higgsino-like WIMPs may provide the first evidence of RNS. Since higgsinos are thermally underproduced, one expects them to constitute only a portion of the measured dark matter abundance, with perhaps axions comprising the remainder. Detectability via WIMP searches will depend on the higgsino fraction of the dark matter. Noble liquid detectors such as the 1-ton scale Xenon detector have the opportunity to probe the entirety of RNS parameter space. Detection of the co-dark matter axions offer complementary evidence to WIMP searches.

In conclusion, the possibilities for detection of RNS at colliders and dark matter detectors, along with its desirable theoretical features, merits a high level of scrutiny. The many elegant features presented above impel one to regard RNS as the new paradigm SUSY model.

8 References

[1] G. Aad *et al.* [ATLAS Collaboration], *Phys. Rev.* **D 87** (2013) 012008. [hep-ex];

[2] S. Chatrchyan *et al.* [CMS Collaboration], ions at $\sqrt{s} = 7$ TeV," *J. High Energy Phys.* **1210** (2012) 018.

[3] A. Chamseddine, R. Arnowitt and P. Nath, *Phys. Rev. Lett.* **49** (1982) 970; R. Barbieri, S. Ferrara and C. Savoy, *Phys. Lett.* **B 119** (1982) 343; N. Ohta, *Prog. Theor. Phys.* **70** (1983) 542; L. Hall, J. Lykken and S. Weinberg, *Phys. Rev.* **D 27** (1983) 2359.

[4] Some early global analyses of mSUGRA phenomenology may be found in, V. D. Barger, M. S. Berger and P. Ohmann, *Phys. Rev.* **D 47** (1993) 1093; G. Kane, C. Kolda, L. Roszkowski and J. Wells, *Phys. Rev.* **D 49** (1994) 6173; H. Baer, C-h. Chen, F. Paige, R. Munroe and X. Tata, *Phys. Rev.* **D 51** (1995) 1046.

[5] J. R. Ellis, K. Enqvist, D. V. Nanopoulos and F. Zwirner, Mod. Phys. Lett. A **1** (1986) 57.

[6] R. Barbieri and G. Giudice, *Nucl. Phys.* **B 306** (1988) 63.

[7] G. W. Anderson and D. J. Castano, Phys. Lett. B **347** (1995) 300.

[8] S. Dimopoulos and G. F. Giudice, Phys. Lett. B **357** (1995) 573.

[9] G. W. Anderson and D. J. Castano, Phys. Rev. D **52** (1995) 1693.

[10] K. Chan, P. Nath and U. Chattopaadhyay, *Phys. Rev.* **D 58** (1998) 096004

[11] P. H. Chankowski, J. R. Ellis and S. Pokorski, Phys. Lett. B **423** (1998) 327; P. H. Chankowski, J. R. Ellis, M. Olechowski and S. Pokorski, Nucl. Phys. B **544** (1999) 39.

[12] G. L. Kane and S. F. King, Phys. Lett. B **451** (1999) 113; M. Bastero-Gil, G. L. Kane and S. F. King, Phys. Lett. B **474** (2000) 103.

[13] S. Cassel, D. M. Ghilencea and G. G. Ross, Nucl. Phys. B **825** (2010) 203 and Nucl. Phys. B **835** (2010) 110; S. Cassel, D. M. Ghilencea, S. Kraml, A. Lessa and G. G. Ross, JHEP **1105** (2011) 120.

[14] I. Gogoladze, F. Nasir and Q. Shafi, arXiv:1212.2593 [hep-ph]; H. Baer, V. Barger and M. Padeffke-Kirkland, *Phys. Rev.* **D 88** (2013) 055026.

[15] R. Kitano and Y. Nomura, *Phys. Lett.* **B 631** (2005) 58 and *Phys. Rev.* **D 73** (2006) 095004.

[16] N. Arkani-Hamed, talk at WG2 meeting, Oct. 31, 2012, CERN, Geneva.

[17] M. Papucci, J. T. Ruderman and A. Weiler, *J. High Energy Phys.* **1209** (2012) 035; C. Brust, A. Katz, S. Lawrence and R. Sundrum, *J. High Energy Phys.* **1203** (2012) 103; R. Essig, E. Izaguirre, J. Kaplan and J. G. Wacker, *J. High Energy Phys.* **1201** (2012) 074;

[18] C. Wymant, *Phys. Rev.* **D 86** (2012) 115023; E. Arganda, J. L. Diaz-Cruz and A. Szynkman, European Physical Journal C **73** (2013) 2384.

[19] H. Baer, V. Barger, P. Huang and X. Tata, *J. High Energy Phys.* **1205** (2012) 109.

[20] P. Higgs, *Phys. Rev. Lett.* **13** (1964) 508.

[21] F. Englert, R. Brout, *Phys. Rev. Lett.* **13** (1964) 321.

[22] G. Aad *et al.* [ATLAS Collaboration], *Phys. Lett.* **B 716** (2012) 1.

[23] S. Chatrchyan *et al.* [CMS Collaboration], *Phys. Lett.* **B 716** (2012) 30.

[24] *Weak Scale Supersymmetry*, H. Baer and X. Tata (Cambridge, 2006)

[25] Joint LEP 2 Supersymmetry Working Group, *Combined LEP Chargino Results up to 208 GeV*, `http://lepsusy.web.cern.ch/lepsusy/www/inos_moriond01/charginos_pub.html`.

[26] L. E. Ibañez and G. G. Ross, Phys. Lett. **B110**, 215 (1982); K. Inoue *et al.* Prog. Theor. Phys. **68**, 927 (1982) and **71**, 413 (1984); L. Ibañez, Phys. Lett. **B118**, 73 (1982); J. Ellis, J. Hagelin, D. Nanopoulos and M. Tamvakis, Phys. Lett. **B125**, 275 (1983); L. Alvarez-Gaumé. J. Polchinski and M. Wise, Nucl. Phys. **B221**, 495 (1983).

[27] H. Baer, A. Mustafayev, S. Profumo, A. Belyaev, and X. Tata *Phys. Rev.* **D 71** (2005) 095008.

[28] J. Ellis, K. Olive and Y. Santoso, *Phys. Lett.* **B 539** (2002) 107; J. Ellis, T. Falk, K. Olive and Y. Santoso, *Nucl. Phys.* **B 652** (2003) 259; H. Baer, A. Mustafayev, S. Profumo, A. Belyaev and X. Tata, *J. High Energy Phys.* **0507** (2005) 065.

[29] R. Peccei, H. Quinn, *Phys. Rev. Lett.* **38** (1977) 1440

[30] R. Peccei, H. Quinn, *Phys. Rev.* **D 16** (1977) 1791

[31] S. Weinberg, *Phys. Rev. Lett.* **40** (1978) 223

[32] F. Wilczek, *Phys. Rev. Lett.* **40** (1978) 279

[33] H. Baer, V. Barger and D. Mickelson, *Phys. Rev.* **D 88** (2013) 095013.

[34] H. Baer, V. Barger, D. Mickelson, and M. Padeffke-Kirkland, *Phys. Rev.* **D 89** (2014) 115019.

[35] S. Dimopoulos and H. Georgi, *Nucl. Phys.* **B 193** (1981) 150; E. Witten, *Nucl. Phys.* **B 1982** (513) ; R. Kaul *Phys. Lett.* **B 109** (1982) 19.

[36] E. Gildner and S. Weinberg, *Phys. Rev.* **D 13** (1976) 333; E. Gildner, *Phys. Rev.* **D 14** (1976) 117;see also L. Susskind, *Phys. Rev.* **D 20** (1979) 2619.

[37] H. Baer, V. Barger, P. Huang, D. Mickelson, A. Mustafayev, W. Sreethawong and X. Tata, *Phys. Rev. Lett.* **110** (2013) 151801.

[38] A. G. Delannoy, B. Dutta, A. Gurrola, W. Johns, T. Kamon, E. Luiggi, A. Melo and P. Sheldon *et al.*, arXiv:1304.7779 [hep-ph].

[39] H. Baer, V. Barger and D. Mickelson, *Phys. Lett.* **B 726** (2013) 330.

[40] H. Baer, V. Barger, P. Huang, D. Mickelson, A. Mustafayev and X. Tata, *Phys. Rev.* **D 87** (2013) 115028.

[41] H. Baer, V. Barger, P. Huang, D. Mickelson, A. Mustafayev and X. Tata, *Phys. Rev.* **D 87** (2013) 035017.

[42] V. Barger, M. S. Berger, and P. Ohmann, *Phys. Rev.* **D 49** (1994) 4908, [hep-ph/9311269].

[43] L. E. Ibanez, C. Lopez and C. Munoz, Nucl. Phys. B **256** (1985) 218; A. Lleyda and C. Munoz, Phys. Lett. B **317** (1993) 82.

[44] H. Abe, T. Kobayashi and Y. Omura, Phys. Rev. D **76** (2007) 015002.

[45] S. P. Martin, Phys. Rev. D **75** (2007) 115005 .

[46] For a recent review, see *e.g.* J. L. Feng, arXiv:1302.6587 [hep-ph].

[47] H. Baer, V. Barger, P. Huang, A. Mustafayev and X. Tata, Phys. Rev. Lett. **109** (2012) 161802.

[48] M. Dine, A. Kagan and S. Samuel, *Phys. Lett.* **B 243** (1990) 250; A. Cohen, D. B. Kaplan and A. Nelson, *Phys. Lett.* **B 388** (1996) 588; T. Moroi and M. Nagai, *Phys. Lett.* **B 723** (2013) 107.

[49] N. Arkani-Hamed and H. Murayama, *Phys. Rev.* **D 56** (1997) 6733.

[50] R. Arnowitt and P. Nath, *Phys. Rev.* **D 46** (1992) 3981.

[51] A. V. Gladyshev, D. I. Kazakov, W. de Boer, G. Burkart and R. Ehret, *Nucl. Phys.* **B 498** (1997) 3.

[52] R. Aaij *et al.* [LHCb Collaboration], Phys. Rev. Lett. **110** (2013) 021801

[53] ISAJET, by H. Baer, F. Paige, S. Protopopescu and X. Tata, [hep-ph/0312045].

[54] H. Baer, C. H. Chen, R. Munroe, F. Paige and X. Tata, *Phys. Rev.* **D 51** (1995) 1046; H. Baer, J. Ferrandis, S. Kraml and W. Porod, *Phys. Rev.* **D 73** (2006) 015010.

[55] K. Agashe and M. Graesser, *Phys. Rev.* **D 59** (1998) 015007.

[56] H. Baer, C. Balazs, P. Mercadante, X. Tata and Y. Wang, *Phys. Rev.* **D 63** (2001) 015011.

[57] H. Baer, V. Barger, A. Lessa and X. Tata, *J. High Energy Phys.* **1006** (2010) 102, *Phys. Rev.* **D 85** (2012) 051701 and *Phys. Rev.* **D 86** (2012) 117701.

[58] H. Baer, A. Belyaev, T. Krupovnickas and X. Tata, *J. High Energy Phys.* **0402** (2004) 007; H. Baer, T. Krupovnickas and X. Tata, *J. High Energy Phys.* **0406** (2004) 061.

[59] H. Baer, V. Barger and P. Huang, *J. High Energy Phys.* **1111** (2011) 031.

[60] F. Gabbiani, E. Gabrielli, A. Masiero and L. Silvestrini, general SUSY extensions *Nucl. Phys.* **B 477** (1996) 321.

[61] J. Hagelin, S. Kelley and T. Tanaka, *Nucl. Phys.* **B 415** (1994) 293; H. Baer, A. Belyaev, T. Krupovnickas and A. Mustafayev, *J. High Energy Phys.* **0406** (2004) 044.

[62] D. Asner *et al.* [Heavy Flavor Averaging Group], [arXiv: 1010.1589] [hep-ex].

[63] M. Misiak *et al.*, *Phys. Rev. Lett.* **98** (2007) 022002.

[64] H. Baer and M. Brhlik, *Phys. Rev.* **D 55** (1997) 3201.

[65] G. Buchalla, A. J. Buras and M. Lautenbacher, Rev. Mod. Phys. **68** (1996) 1125.

[66] S. Rai Choudhury and N. Gaur, *Phys. Lett.* **B 451** (1998) 86; K. S. Babu and C. F. Kolda, *Phys. Rev.* **D 84** (2000) 28; our calculation uses the formulae in J. Mizukoshi, X. Tata and Y. Wang, *Phys. Rev.* **D 66** (2002) 115003.

[67] H. Baer, S. Kraml and S. Kulkarni, *J. High Energy Phys.* **1212** (2012) 066, [arXiv: 1208.3039] [hep-ph].

[68] G. W. Bennett *et al.* (Muon $g-2$ Collaboration), *Phys. Rev.* **D 80** (2009) 052008.

[69] H. Baer, V. Barger, P. Huang, D. Mickelson, A. Mustafayev, W. Sreethawong and X. Tata, *J. High Energy Phys.* **1312** (2013) 013.

[70] H. Baer, V. Barger, G. Shaughnessy, H. Summy and L. -t. Wang, *Phys. Rev.* **D 75** (2007) 095010.

[71] R. Kadala, [arXiv: 1205.1267].

[72] W. Beenakker, R. Hopker and M. Spira, [hep-ph/9611232].

[73] H. Baer, X. Tata and J. Woodside, *Phys. Rev.* **D 42** (1990) 1568.

[74] H. Baer, C. -h. Chen, M. Drees, F. Paige and X. Tata, *Phys. Rev.* **D 58** (1998) 075008.

[75] T. Han, S. Padhi and S. Su, [arXiv: 1309.5966] [hep-ph].

[76] H. Baer, J. Ellis, G. Gelmini, D. Nanopoulos and X. Tata, *Phys. Lett.* **B 161** (1985) 175; G. Gamberini, *Z. Physik* **C 30** (1986) 605; H. Baer, V. Barger, D. Karatas and X. Tata, *Phys. Rev.* **D 36** (1987) 96.

[77] I. Hinchliffe, F. E. Paige, M. D. Shapiro, J. Soderqvist and W. Yao, *Phys. Rev.* **D 55** (1997) 5520.

[78] See J. Gaunt, C-H. Kom, A. Kulesza and W. J. Stirling, *Eur. Phys. J.* **C 69** (2010) 53, for a recent assessment of dileptons from SS W production and other SM sources at the LHC.

[79] M. L. Mangano, M. Moretti, F. Piccinini, R. Pittau and A. D. Polosa, *J. High Energy Phys.* **0307** (2003) 001.

[80] J. Alwall, M. Herquet, F. Maltoni, O. Mattelaer and T. Stelzer, *J. High Energy Phys.* **1106** (2011) 128 [[arXiv: 1106.0522] [hep-ph]].

[81] T. Sjostrand, S. Mrenna and P. Z. Skands, *J. High Energy Phys.* **0605** (2006) 026.

[82] J. Alwall, A. Ballestrero, P. Bartalini, S. Belov, E. Boos, A. Buckley, J. M. Butterworth and L. Dudko *et al.*, Comput. Phys. Commun. **176** (2007) 300.

[83] J. M. Campbell and R. K. Ellis, Nucl. Phys. Proc. Suppl. **205-206**, 10 (2010) [[arXiv: 1007.3492] [hep-ph]].

[84] M. V. Garzelli, A. Kardos, C. G. Papadopoulos and Z. Trocsanyi, *J. High Energy Phys.* **1211** (2012) 056.

[85] H. Baer, V. Barger, A. Lessa and X. Tata, *Phys. Rev.* **D 86** (2012) 117701.

[86] H. Baer, V. Barger, A. Lessa and X. Tata, *J. High Energy Phys.* **0909** (2009) 063.

[87] S. Chatrchyan *et al.* [CMS Collaboration], *Phys. Rev. Lett.* **109** (2012) 071803 and [arXiv: 1212.6194] [hep-ex]. See CMS-PAS-SUS-13-013 for an updated (preliminary) analysis.

[88] [ATLAS Collaboration], ATLAS-CONF-2013-007

[89] CMS Collaboration, CMS Physics Analysis Summary, CMS-PAS-SUSY-13-006 (2013).

[90] D. Dicus, S. Nandi and X. Tata, *Phys. Lett.* **B 129** (1983) 451; A. Chamseddine, P. Nath and R. Arnowitt, *Phys. Lett.* **B 129** (1983) 445; H. Baer and X. Tata,*Phys. Lett.* **B 155** (1985) 278; H. Baer, K. Hagiwara and X. Tata, *Phys. Rev. Lett.* **57** (1986) 294 and *Phys. Rev.* **D 35** (1987) 1598; R. Arnowitt and P. Nath, *Mod. Phys. Lett.* **A 2** (1987) 331; R. Barbieri, F. Caravaglios, M. Frigeni and M. Mangano, *Nucl. Phys.* **B 367** (1991) 28; H. Baer and X. Tata, *Phys. Rev.* **D 47** (1993) 2739; J. Lopez, D. Nanopoulos, X. Wang and A. Zichichi, *Phys. Rev.* **D 48** (1993) 2062 and *Phys. Rev.* **D 52** (1995) 142; H. Baer, C. Kao and X. Tata, *Phys. Rev.* **D 48** (1993) 5175; S. Mrenna, G. Kane, G. Kribs and J. Wells, *Phys. Rev.* **D 53** (1996) 1168; H. Baer, C. H. Chen, F. Paige and X. Tata, *Phys. Rev.* **D 54** (1996) 5866; K. Matchev and D. Pierce, *Phys. Rev.* **D 60** (1999) 075004; H. Baer, M. Drees, F. Paige, P. Quintana and X. Tata, *Phys. Rev.* **D 61** (2000) 095007; V. Barger, C. Kao and T. Li, *Phys. Lett.* **B 433** (1998) 328; V. Barger and C. Kao, *Phys. Rev.* **D 60** (1999) 115015; K. Matchev and D. Pierce, *Phys. Lett.* **B 467** (1999) 225; H. Baer, T. Krupovnickas and X. Tata, *J. High Energy Phys.* **0307** (2003) 020.

[91] H. Baer, V. Barger, S. Kraml, A. Lessa, W. Sreethawong and X. Tata, *J. High Energy Phys.* **1203** (2012) 092 [[arXiv: 1201.5382] [hep-ph]].

[92] Talks presented by C. Potter (for ATLAS Collaboration) and B. Hooberman (for CMS collaboration) at SUSY 2013, *21st International Conference on Supersymmetry and Unification of Fundamental Interactions,* Trieste, Italy, Aug. 2013.

[93] M. L. Mangano, M. Moretti, F. Piccinini and M. Treccani, *J. High Energy Phys.* **0701** (2007) 013 [[hep-ph/0611129]].

[94] [ATLAS Collaboration], ATLAS-CONF-2013-036.

[95] The CMS Collaboration, CMS-PAS-SUS-13-010

[96] H. Baer, V. Barger, D. Mickelson, A. Mustafayev, X. Tata, *J. High Energy Phys.* **1406** (2014) 172.

[97] H. Baer, T. Barklow, K. Fujii, Y. Gao, A. Hoang, S. Kanemura, J. List and H. E. Logan *et al.*, arXiv:1306.6352 [hep-ph].

[98] H. Baer, M. Berggren, J. List, M. M. Nojiri, M. Perelstein, A. Pierce, W. Porod and T. Tanabe, arXiv:1307.5248 [hep-ph].

[99] T. Tsukamoto, K. Fujii, H. Murayama, M. Yamaguchi and Y. Okada, Phys. Rev. D **51** (1995) 3153.

[100] H. Baer, R. Munroe and X. Tata, *Phys. Rev.* **D 54** (1996) 6735 [Erratum-ibid. D **56** (1997) 4424].

[101] H. Baer, A. Belyaev, T. Krupovnickas and X. Tata, *J. High Energy Phys.* **0402** (2004) 007.

[102] H. Baer, T. Krupovnickas and X. Tata, *J. High Energy Phys.* **0406** (2004) 061.

[103] J. L. Feng, K. T. Matchev and T. Moroi, Phys. Rev. D **61** (2000) 075005; J. L. Feng and K. T. Matchev, Phys. Rev. D **63** (2001) 095003; J. L. Feng, K. T. Matchev and D. Sanford, Phys. Rev. D **85** (2012) 075007.

[104] T. Han, S. Padhi and S. Su, *Phys. Rev.* **D 88** (2013) 115010; M. Berggren, T. Han, J. List, S. Padhi, S. Su and T. Tanabe, [arXiv: 1309.7342] [hep-ph].

[105] M. Berggren, F. Brmmer, J. List, G. Moortgat-Pick, T. Robens, K. Rolbiecki and H. Sert, *Eur. Phys. J.* **C 73** (2013) 2660.

[106] H. Baer and J. List, *Phys. Rev.* **D 88** (2013) 055004.

[107] E. A. Kuraev and V.S Fadin, *Sov. J. Nucl. Phys.* **41** (1985) 466.

[108] P. Chen, *Phys. Rev.* **D 46** (1992) 1186; M. Peskin, SLAC-TN-04-032.

[109] K. J. Bae, H. Baer and E. J. Chun, Phys. Rev. D **89** (2014) 031701 and JCAP **1312** (2013) 028.

[110] H. Baer, A. Bartl, D. Karatas, W. Majerotto and X. Tata, *Int. J. Mod. Phys.* **A 4** (1989) 4111.

[111] H. Komatsu and H. Kubo, *Phys. Lett.* **B 157** (1985) 90 and *Nucl. Phys.* **B 263** (1986) 265; H. Haber and D. Wyler, *Nucl. Phys.* **B 323** (1989) 267; H. Baer and T. Krupovnickas, *J. High Energy Phys.* **0209** (2002) 038.

[112] C. Adolphsen, M. Barone, B. Barish, K. Buesser, P. Burrows, J. Carwardine, J. Clark and Hln. M. Durand *et al.*, [arXiv: 1306.6328] [physics.acc-ph].

[113] M. Drees and R. M. Godbole, *Phys. Rev.* **D 50** (1994) 3124.

[114] G. A. Blair, eConf C **010630** (2001) E3019; for corresponding studies at a muon collider see V. D. Barger, M. S. Berger and T. Han, *Phys. Rev.* **D 59** (1999) 71701.

[115] G. Hinshaw, D. Larson, E. Komatsu, D.N. Spergel, C.L. Bennett, J. Dunkley, M.R. Nolta, M. Halpern, *et. al.*, arXiv:1212.5226.

[116] See IsaReD, H. Baer, C. Balazs, A. Belyaev, *J. High Energy Phys.* **0203** (2002) 042.

[117] G. Jungman, M. Kamionkowski, K. Greist, *Phys. Rep.* **267** (1996) 195.

[118] H.P. Nilles, S. Raby, *Nucl. Phys.* **B 198** (1982) 102; J.E. Kim, *Phys. Lett.* **B 136** (1984) 378; J.E. Kim, H.P. Nilles, *Phys. Lett.* **B 138** (1984) 150; For a review, see e.g. F.D. Steffen, *Eur. Phys. J.* **C 59** (2009) 557.

[119] P. Moxhay, K. Yamamoto, *Phys. Lett.* **B 151** (1985) 363; E. Chun, A. Lukas, *Phys. Lett.* **B 357** (1995) 43; J.E. Kim, M.-S. Seo, *Nucl. Phys.* **B 864** (2012) 296; C. Cheung, G. Elor, L.J. Hall, *Phys. Rev.* **D 85** (2012) 015008.

[120] K-Y. Choi, J. E. Kim, H. M. Lee and O. Seto, *Phys. Rev.* **D 77** (2008) 123501; H. Baer, A. Lessa, S. Rajagopalan and W. Sreethawong, JCAP**1106** (2011) 031; H. Baer, A. Lessa and W. Sreethawong, JCAP**1201** (2012) 036; K. J. Bae, H. Baer and E. J. Chun, [arXiv: 1309.0519] [hep-ph] and [arXiv: 1309.5365] [hep-ph].

[121] K. J. Bae, H. Baer and A. Lessa, JCAP **1304** (2013) 041;

[122] H. Baer, C. Balazs, A. Belyaev, J. O'Farrill, *J. Cosmol. Astropart. Phys.* **0309** (2003) 007.

[123] A. Bottino, F. Donato, N. Fornengo, S. Scopel, *Phys. Rev.* **D 63** (2001) 125003.

[124] E. Aprile *et al.* [Xenon100 Collaboration], *Phys. Rev. Lett.* **109** (2012) 181301.

[125] D. S. Akerib *et al.* [LUX Collaboration], Nuclear Inst. Methods in Physics Research A704 (2013) 111-126.

[126] E. Aprile *et al.* [Xenon100 Collaboration], arXiv:1206.6288.

[127] E. Behnke, *et al.*, COUPP Collaboration, *Phys. Rev.* **D 86** (2012) 052001.

[128] R. Abbasi, *et al.*, IceCube Collaboration, *Phys. Rev.* **D 85** (2012) 042002.

[129] V. Niro, A. Bottino, N. Fornengo, S. Scopel, *Phys. Rev.* **D 80** (2009) 095019.

[130] A. Bottino, F. Donato, N. Fornengo, P. Salati, *Phys. Rev.* **D 72** (2005) 083518.

[131] M. Ackermann, *et al.*, Fermi Collaboration, *Phys. Rev. Lett.* **107** (2011) 241302.

[132] V. Barger, Y. Gao, W.Y. Keung, D. Marfatia, G. Shaughnessy, *Phys. Lett.* **B 678** (2009) 283; S. Profumo, *Cent. Eur. J. Phys.* **10** (2011) 1.

[133] G. Belanger, C. Boehm, M. Cirelli, J. Da Silva, A. Pukhov, *J. Cosmol. Astropart. Phys.* **1211** (2012) 028.

[134] O. Adriani, *et al.*, PAMELA Collaboration, *Phys. Rev. Lett.* **105** (2010) 121101.

[135] S.J. Asztalos, *et al.*, *Nucl. Instr. and Meth. in Phys. Res.* **A 656** (2011) 39.